Journal of Materials Chemistry A

REVIEW

View Article Online
View Journal | View Issue

Cite this: J. Mater. Chem. A, 2024, 12, 7351

Scope, evaluation and current perspectives of MXene synthesis strategies for state of the art applications†‡

Muhammad Zeeshan Abid, [a] Khezina Rafiq, *[a] Anam Aslam, [a] Rongchao Jin [b] and Ejaz Hussain *[ab]

Received 26th October 2023
Accepted 16th January 2024

DOI: 10.1039/d3ta06548k

rsc.li/materials-a

MXenes have garnered considerable attention as 2D functional materials. Their application in advanced applications is linked to synthetic approaches, terminal groups (=O, –OH, and –F *etc.*) and multiple characteristics. Functionality and control over MXene terminations are important factors. MXenes exhibit a regular planar structure, conductivity, tuneable fabrication and structural modifications, as well as superior optical, thermal, and chemical properties. These exceptional characteristics grant MXenes and their derivatives distinction among 2D materials. MXenes have practical applications in energy conversion/storage, catalysis, sensing, water purification, drug delivery, and cancer treatments. Recent advances, with a primary focus on MXenes synthesis and terminations linked to their method of preparation, are the focus of this review. We offer potential solutions to the challenges faced by researchers during MXene synthesis. We describe the advantages, drawbacks, and mechanism associated with MXene fabrications and developments. Despite significant progress on MXene-oriented research, several challenges must be addressed before practical applications.

1. Introduction

Over the past 20 years, two-dimensional (2D) materials have garnered great interest due to their extraordinary characteristics. This interest has sparked new developments in 2D materials and led to diverse applications. Materials such as MXenes, graphene, g-C_3N_4, metal chalcogenides and boron nitrides have attained special interest due to their appealing characteristics for practical applications.[1,2] Among 2D materials, MXenes have attained special recognition not only to

[a]*Institute of Chemistry, Inorganic Materials Laboratory 52S, The Islamia University of Bahawalpur, 63100, Pakistan. E-mail: ejaz.hussain@iub.edu.pk; khezina.rafiq@iub.edu.pk*

[b]*Department of Chemistry, Carnegie Mellon University, Pittsburgh, Pennsylvania-15213, USA*

† This work has been dedicated to our son Muhammad Arhaan Ejaz on the ocassion of his 3rd birthday.

‡ Electronic supplementary information (ESI) available. See DOI: https://doi.org/10.1039/d3ta06548k

Muhammad Zeeshan Abid

Muhammad Zeeshan Abid is a doctoral student at the Institute of Chemistry, Islamia University of Bahawalpur. He is working under the supervision of Dr Ejaz Hussain. His research interests include the synthesis of MXene-derived compounds for various applications.

Khezina Rafiq

Dr Khezina Rafiq is Assistant Professor at the Institute of Chemistry, Islamia University of Bahawalpur. She has been awarded Global Korea Scholarship for PhD in Chemistry from Hallym University, South Korea. She has a patent invention and has published several research articles in well-known scientific journals. Her research interests include the synthesis of novel compounds for portable kidney devices, electrochemical sensing, as well as energy and environmental applications.

academic researchers but also for the industrial researchers. MXenes (pronounced "maxenes") comprise transition-metal carbides and nitrides.[3] MXenes were reported for the first time in 2011. After this discovery, synthetic protocols and applications of MXenes have been consistently improved. MXenes have been derived from etching of the MAX phase by the removal of inherited A-layers. The typical formula for the MAX phase is $M_{n+1}AX_n$, where M represents early transition metals from groups III to VI (i.e., Sc, Ti, Zr, V, Nb, Ta, Cr, Mo, W). These elements can form MAX phases because they possess specific electronic configurations and a layered hexagonal close-packed (hcp) structure (in space group $P6_3/mmc$) that allows their exfoliation[4]. In contrast, late transition metals (i.e., Ag, Cu, Ni, Pd, Pt, Au and Zn) do not form hcp-layered structures due to their higher valence electrons (shielding). The involvement of d-electrons is important for development of the MAX phase.[5] These factors significantly hinder the bonding needed to achieve the compatibility for layered structures that are essential for MAX-phase stability[6]. Late transition metals exhibit relatively incompatible bonding and cannot facilitate formation of stable M layers.[7] Moreover, the tendency of late transition metals to form non-layered structures (strong covalent bonds) often leads to stable phases that commonly remain distinct from MAX phases.[8] "A" stands for 13 or 14 element of the group. X stands for C, N and O (for oxynitrides and oxycarbides).[9] In most reports, the general formula of MXenes is represented as $M_{n+1}X_nT_x$, where T_x stands for terminal groups (*i.e.*, =O, –OH, –F, –Cl, or =S). MXene terminations are the chemical functional groups over the surfaces of a MXene.[10] Fig. 1a represents the chemical compositions of MAX and MXenes.[11]

MXenes have been employed in various advanced applications: energy storage,[12–17] electronics,[18–21] environmental,[22–26] sensors,[27–33] catalysis[34–38] and biomedicine.[39,40] The advanced features and flexibility of MXene structures are the main causes of their diverse applications. The chemical and physical properties of MXenes can be modified by controlling the MXene terminations to targeted applications. MXene terminations have been altered to generate layers for "sensing" different gases or chemicals. This sensing mechanism relies upon changes in MXene electrical conductivity or capacitance due to the presence of adsorbate molecules.[41] In addition, MXene terminations can affect surface properties, such as wettability, that enhance the sensing performances. MXene-based sensors have been effectively utilized for gas-, humidity-, and chemical-sensing applications. Further research is ongoing to develop more advanced MXene-based sensors with improved sensitivity and selectivity.[42]

The world has been facing an energy crisis but MXene-based materials have the potential to build a new hope to reduce this issue.[43] There is great demand to replace conventional energy sources by developing alternative, sustainable and clean energy sources.[44] The energy crisis can be overcome by solar-energy harvesting.[45] For this purpose, researchers are interested in hydrogen generation *via* water splitting on MXenes and their substitutes.[46] In this context, the characteristics of super charge-conducting materials like MXenes are crucial because these materials have potential to transfer photo-induced charges (e^-/h^+) to active centres. Moreover, the effectiveness of a sustainable catalytic system depends on the ability to reduce back reactions.[47,48] Semiconductors exhibit low visible absorption. However, upon combination with a MXene, charge-carrier

Anam Aslam

Anam Aslam is an MS student in Chemistry under the supervision of Dr Khezina Rafiq at Institute of Chemistry, Islamia University of Bahawalpur. Her research focuses on the development of advanced inorganic materials for photocatalytic applications.

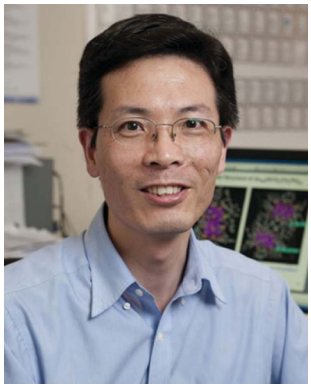

Rongchao Jin

Dr Rongchao Jin is Professor of Chemistry at Carnegie Mellon University. He received his BS in Chemical Physics from USTC in 1995, an MS in Physical Chemistry/Catalysis from the Dalian Institute of Chemical Physics in 1998, and his PhD in Chemistry from Northwestern University in 2003. After post-doctoral research at the University of Chicago, he joined the chemistry faculty of CMU in 2006. His research interests include atomically precise nanoparticles, and nanoclusters for optics and catalysis applications.

Ejaz Hussain

Dr Ejaz Hussain is an Assistant Professor in the Institute of Chemistry, Islamia University of Bahawalpur. He received his PhD from Quaid-i-Azam University. He was awarded a scholarship for advanced research at the Department of Chemistry, Carnegie Mellon University (with Professor Rongchao Jin). He was accredited with the "Best Researcher Award 2015–2016". He is a mentor and key scientist in Inorganic Materials Laboratory 52S, and has expertise on water-splitting, renewable energy, and environmental science.

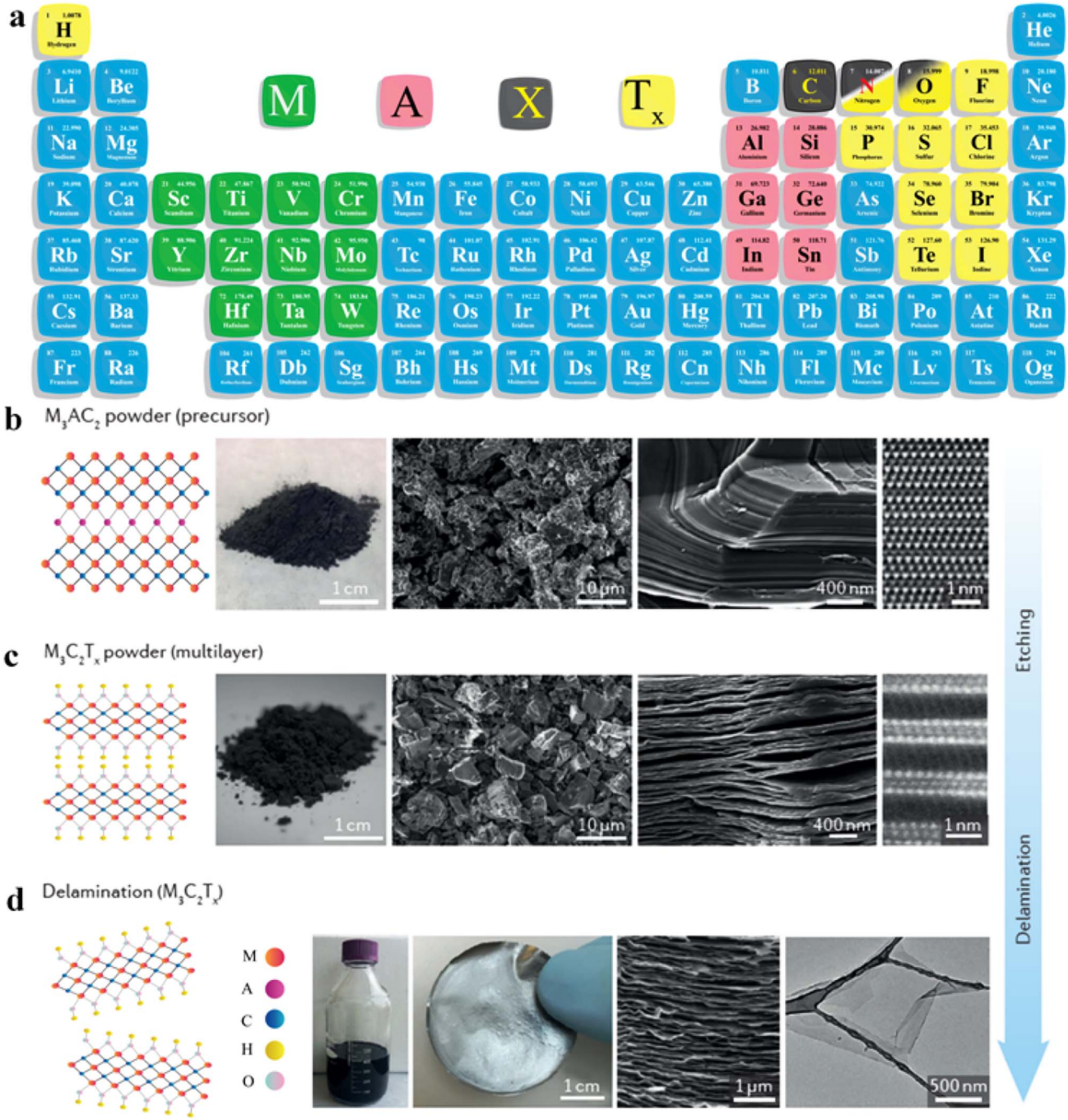

Fig. 1 (a) Important elemental constituents of MAX and MXenes. The black highlight in O represents oxycarbides and oxynitrides, reproduced from ref. 11 with permission from Royal Society of Chemistry, copyright 2022. (b and c) Atomic structure, SEM and HR-STEM results of precursors of MAX (Ti_3AlC_2) and a multi-layered MXene ($M_2C_2T_x$). (d) SEM image of a $Mo_2TiC_2T_x$ film of $Ti_3C_2T_x$ in water along with a digital view and TEM image of $Ti_3C_2T_x$ flakes, reproduced from ref. 60 with permission from *Nature Reviews Materials*, copyright 2017.

transportation is significantly enhanced.[49] The efficiency of catalysts can be improved by loading MXene based co-catalysts or any noble metal. Improvement of MXene-based co-catalysts is needed to boost efficiency and scale-up photocatalytic applications.[50]

The functional groups (–OH, =O and –F) present on the surface of MXenes as terminations are dependent upon the type of etchant used in the synthesis.[51] Direct hydrofluoric acid (HF) etching of MXenes enables changes in the proportion of –OH, =O, and –F groups on the surface of MXenes.[52] In this context, titanium carbide (Ti_3C_2) has drawn much interest to researchers for energy conversion and energy-storage systems.[53] This article provides insights on the synthetic methods for –Cl, –Br, and –I terminated MXenes by utilization of molten salts (such as

$ZnCl_2$) to erode the aluminium or "A" layer,[54] which can be further modified with other terminations, like –S, –Te and –NH.[55,56] A commonly utilized MXene ($Ti_3C_2T_x$) is usually terminated by =O and –OH through electrochemical corrosion.[57] MXenes can be produced by the intercalation and delamination of MAX phases for algae extraction.[58] Similarly, MXenes can be developed by a microenvironment method by employing organic solvents. The most effective solvents that have been identified facilitate the dispersion of substantial $Ti_3C_2T_x$ nanosheets.[59]

This article illustrates the improvements in various syntheses and designs for MXenes and their terminations. We focus on the novel designs and approaches, structural modification, and state of the art applications of MXenes. Fig. 1b demonstrates the atomic structures along with a digital image of MAX (*i.e.*, M_3AC_2), whereas Ti_3AlC_2 is exhibited *via* SEM and HR-STEM images. Consequently, HR-STEM results of Mo_2TiAlC_2 provide structural details. Fig. 1c presents various features of MXenes: atomic structures, digital images, and multilayer morphologies. The HR-STEM image (Fig. 1c) shows removal of the aluminium (A) layer to develop $Mo_2TiC_2T_x$. Similarly, Fig. 1d illustrates the atomic structures and TEM result of $Ti_3C_2T_x$ flakes along with cross-sectional SEM results. Additionally, a digital photograph depicts 400 mL of delaminated $Ti_3C_2T_x$ in water and $Mo_2TiC_2T_x$ produced *via* vacuum-assisted filtration.[60]

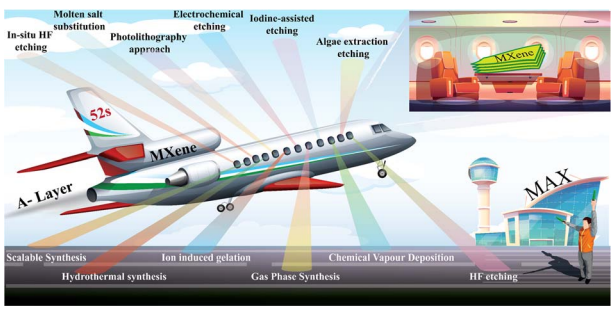

Fig. 2 Synthetic methods for MXenes.

Recent developments in MXenes have also been summarized and evaluated, focusing on their terminations and applications. These factors significantly influence the chemical properties exhibited by MXenes. Furthermore, challenges (along with their potential solutions) associated with MXene design for specific applications have been demonstrated and justified.

2. Different methods for MXene designs

The synthesis of MXenes can be achieved through various etching methods. These include *in situ* etching with hydrofluoric acid (*i.e.* HCl/LiF), direct HF etching, electrochemical etching, molten salt substitution, algae extraction, photolithography, hydrothermal methods, scalable synthesis, as well as iodine-assisted and ion-induced gelation.[55,61–70] Each method has particular advantages along with disadvantages. The chemical structures and electronic properties of MXenes are dependent upon multiple aspects. These aspects may include: (i) purity of the MAX-Phase; (ii) choice of etching agent; (iii) concentration; (iv) stoichiometry of precursors; (v) method employed for preparation; (vi) reaction duration.[71,72] Details of different methods used for MXene synthesis are depicted in Fig. 2.

2.1. *In situ* HF etching

This method was proposed by Ghidiu *et al.*[56] It involves the use of different etchants (*i.e.*, LiF/HCl, LiF/NaF, forming *in situ* HF)[73,74] employed to eliminate the aluminium layers from a MAX-Phase. This etching process ends with the development of a layered MXene with terminations such as =O, –OH and –F (Fig. 3a).[75] This method is also known as the "clay method" because the MXene obtained looks like clay paste.[56] Ammonium fluoride can also be used as an etching agent to reduce the number of intercalation steps.[76]

2.1.1 Mechanism. The *in situ* generation of HF from HCl and LiF facilitates etching of the A layer to form a MXene. The byproducts (*i.e.*, LiCl, AlF_3) further react with MXenes, to

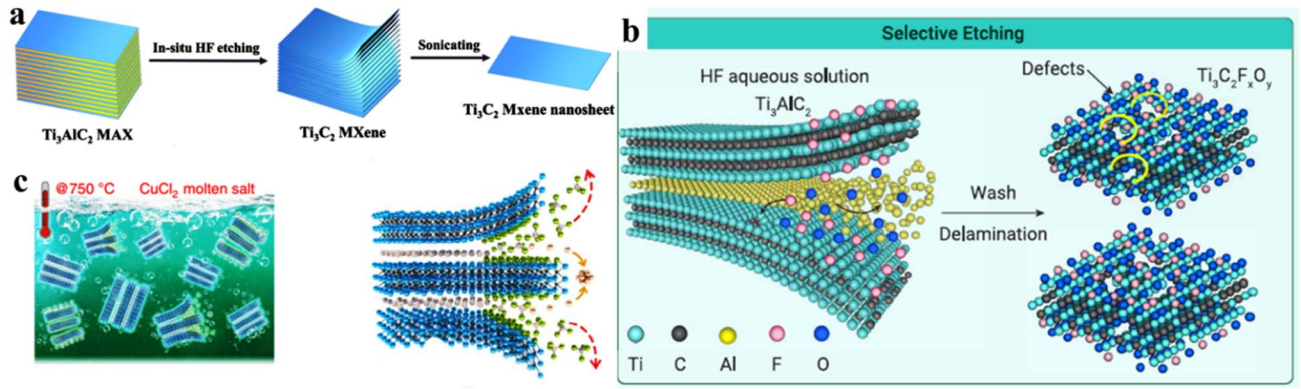

Fig. 3 Synthetic schemes of MXene. (a) Ti_3C_2 MXene nanosheets by *in situ* HF etching, reproduced from ref. 75 with permission from Springer Nature, copyright, 2021. (b) Ti_3C_2 MXene nanosheets by HF etching, reproduced from ref. 82 with permission from ScienceDirect, copyright, 2023. (c) Development of a MXene by molten salt, reproduced from ref. 89 with permission from *Nature*, copyright, 2020.

generate –F, –Cl, –OH and =O terminations. The etching process is depicted through eqn (1)–(5):

$$Ti_3AlC_2 + 3HCl + 3LiF = Ti_3C_2 + 3LiCl + AlF_3 + 1.5H_2 \quad (1)$$

$$Ti_3C_2 + 2HF = Ti_3C_2(F)_2 + H_2 \quad (2)$$

$$Ti_3C_2 + 2HCl = Ti_3C_2(Cl)_2 + H_2 \quad (3)$$

$$Ti_3C_2 + 2H_2O = Ti_3C_2(OH)_2 + H_2 \quad (4)$$

$$Ti_3C_2 + 2H_2O = Ti_3C_2(O)_2 + 2H_2 \quad (5)$$

2.1.2 Advantages. *In situ* HF etching enhances the quality of the MXene. Researchers can produce MXene films of any dimension that promise more conductive properties. Additionally, this method can be used to develop MXene ink to *in situ* deposits on targeted substrates. Also, there is no need for sonication for delamination.[73] The yield of a MXene obtained from *in situ* etching method is 100%.[56] Similarly, this method consumes low energy during its operation. In this method, metal cations can be embedded between MXene sheets to enhance the layered spacing to enable easier separations. The distinct advantage of this method is direct delamination of MXene sheets through intercalating fluoride ions, which provides reaction stability, higher surface area and more redox-active sites.[49]

2.1.3 Drawbacks. The main drawback linked with this approach is that, due to intercalation of water molecules, the drying process can take longer time as compared with other methods.[77] Furthermore, interlayer spacing can be reduced and broken during the drying process. It has been reported that, by increasing –F contents, interlayer spacing in MXene sheets can be diminished.[49]

2.1.4 Precautions and suggestions. It has been suggested that *in situ* HF etching needs more careful handling and stoichiometry of precursors during etching and developments. Intercalation of water contents can be reduced/eradicated by using appropriate solvents.[77–79]

2.2. Direct HF etching

Direct HF etching is a fundamental and widely employed method for producing MXenes and derivatives. In 2011, Naguib *et al.* used this method to etch MAX phases.[80] After HF etching, dense MAX phases were converted into loosely stacked multi-layered MXenes, which contains –OH, –F and =O terminations on their surfaces (Fig. 3b).[81,82] Although these terminations affected the mechanical strength and other properties, they could be controlled by the compatibility of the MXene with the polymer matrix.[83] This method rendered them hydrophilic and highly dispersible in the presence of various polar solvents.[60]

2.2.1 Mechanism. HF assists the etching of MAX to form MXenes. The byproduct (AlF_3) and H_2O react with further MXenes to generate –F, –OH and =O terminations. The etching process is depicted through eqn (6)–(9):

$$2Ti_3AlC_2 + 6HF = 3H_2 + 2Ti_3C_2 + 2AlF_3 \quad (6)$$

$$Ti_3C_2 + 2HF = Ti_3C_2(F)_2 + H_2 \quad (7)$$

$$Ti_3C_2 + 2H_2O = Ti_3C_2(OH)_2 + 2H_2 \quad (8)$$

$$Ti_3C_2 + 2H_2O = Ti_3C_2(O)_2 + 2H_2 \quad (9)$$

2.2.2 Advantages. It is considered a special method if a MXene can be prepared at low or even at room temperature. This is widely recommended for its ease and simplicity of use. Using this method, the –OH group (*i.e.*, termination) can convert $Ti_3C_2OH_x$ *in situ* to TiO_2, which can extend the utility of MXenes for photocatalytic applications.[49] It has been noted that fully fluorine-terminated MXenes have high resistance against oxidation, which enhances their stability. Albeit, fully iodine-terminated MXenes are considered not stable to resist oxidation.[49,84] In addition, HF aqueous etching offers numerous benefits, such as complete elimination of the aluminium layer from the MAX phase, and better morphology and yield.[60] Due to these advantages, researchers mostly use this approach to design MXenes and its other derivatives.[85]

2.2.3 Drawbacks. HF is highly corrosive and toxic, so its direct use is restricted. MXenes produced *via* this method have high fluorine contents. The presence of fluorine is problematic specifically for photocatalytic reactions.[49] Another major disadvantage of F-terminating groups is non-valid electrode/electrolyte interface reactions. Moreover, the interfacial resistance between electrode/electrolyte systems is enhanced, which may reduce the stability and charge-storage performance.[49,86]

2.2.4 Precautions and suggestions. This method needs extra precautions due the corrosive nature of HF (etching agent)[78] as well as persons familiar with safety measures. Materials must be treated appropriately after experimentation.[79,87]

2.3. Molten salt substitution

To avoid the etching risks in other approaches, MXenes can also be prepared using fluoride molten salts (*i.e.*, KF, LiF, NaF, $CuCl_2$ and bifluoride salts) (Fig. 3c). If the salt contains bromide rather than fluoride, the resulting MXene has –Br as a terminating group that can be easily substituted with other groups.[88] Similarly, iodine-terminating MXenes can also be synthesized using iodine-containing molten salts. The adsorption strengths of –Br and –I are overestimated when assessed under a gas phase compared with the elemental state.[84] According to Li *et al.*, MXenes synthesized using molten salt synthesis exhibit an enhanced capacity for lithium-ion storage, which results in higher electrochemical performances.[89]

2.3.1 Mechanism. The molten salt (*i.e.*, $CuCl_2$, $ZnCl_2$) facilitates the etching of MAX phases by reacting with the A-layer. This reaction generates the metal as a byproduct, while the negative parts of the salt (Cl_2) terminated to MXene. The etching process is depicted through eqn (10) and (11):

$$Ti_3AlC_2 + 1.5CuCl_2 = Ti_3CuC_2 + 0.5Cu + AlCl_3 \quad (10)$$

$$Ti_3CuC_2 + CuCl_2 = Ti_3C_2(Cl)_2 + 2Cu \quad (11)$$

2.3.2 Advantages. The distinct advantage is that the salt precursors of chlorine, fluorine, and iodine exhibit satisfactory binding, but the binding strength is dependent upon the surface terminations. In the case of iodine, the disparity between low and full surface terminations is comparatively large, and can reach up to 2 eV for Nb_4C_3.[84] The other advantage of this approach is that, due to the termination of Cl, stable MXenes can be developed (which is uncommon using other methods).[90] Cl-terminating groups provide excellent durability to MXenes. Additionally, molten salt etching has a broader etching range comparatively.[91] Lewis-acid etching does not require the use of HF, so it is a practical and environment friendly method for generating MXenes.[10]

2.3.3 Drawbacks. This approach requires a high temperature (>500 °C). The other drawback linked with this approach is the production of unwanted byproducts. In this approach, further purification may be the sole requirement. This method enhances the complexity on MXene surfaces, which may alter or affect chemical properties.[49]

2.3.4 Precautions and suggestions. Appropriate heating equipment/instruments that can control and precisely measure the temperature are necessary.[79,87] To obtain targeted and desired properties, extra care and expertise are mandatory for setting the required conditions (etching salt and temperature).[78]

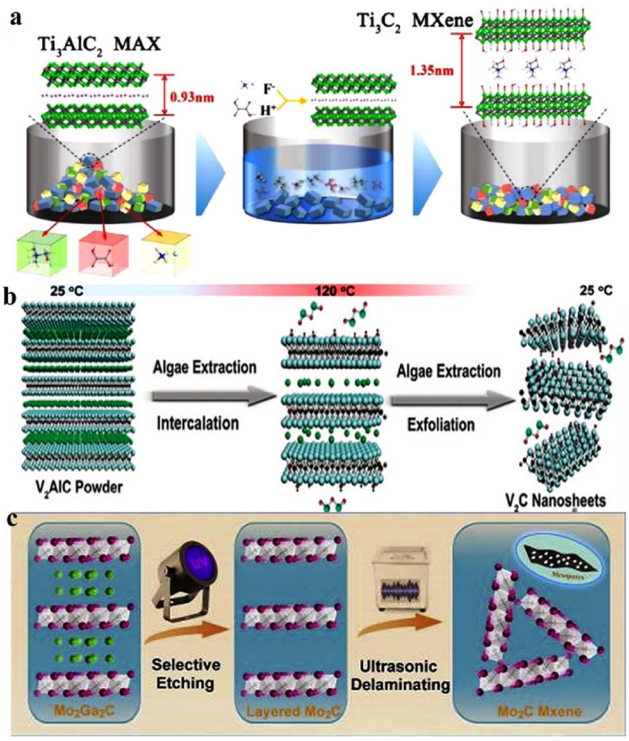

Fig. 4 Synthesis of MXenes *via* electrochemical, algae-extraction and UV-induced selective etching methods. (a) Synthesis of MXenes *via* electrochemical etching, reproduced from ref. 79 with permission from Springer Nature, Elsevier, copyright 2020. (b) Production of V_2C NSs *via* algae extraction (schematic), reproduced from ref. 58 with permission from Wiley, copyright 2020. (c) Synthesis of MXene *via* a UV-induced selective etching method, reproduced from ref. 96 with permission from Elsevier, copyright 2020.

2.4. Electrochemical etching

Electrochemical etching that usually performed in HCl may cause combinations of =O, –OH and –Cl terminating groups. Fig. 4a illustrates the synthesis of MXene *via* electrochemical etching. Yang *et al.*[57] demonstrated that $Ti_3C_2T_x$ MXenes can be synthesized through electrochemical corrosion. However, in some cases, electrochemical etching can lead to the generation of carbon-derived carbides (CDC).[92] However, by altering the electrolyte composition, aluminium atoms can be substituted with OH groups. As a result, double- or single-layer $Ti_3C_2T_x$ nanosheets can be generated at >90% yield.[54] Three types of MXenes, namely Ti_2CT_x, V_2CT_x, and Cr_2CT_x, have been synthesized and reported by this method.[93]

2.4.1 Mechanism. In the electrochemical processes, MAX reacts with chloride ions to form MXenes. Subsequently, MXenes react with water and hydroxide ions to produce –OH-terminated MXenes. The etching process is depicted through eqn (12)–(14):

$$Ti_3AlC_2 + 3Cl^- - 3e^- = Ti_3C_2 + AlCl_3 \quad (12)$$

$$Ti_3C_2 + 2OH^- - 2e^- = Ti_3C_2(OH)_2 \quad (13)$$

$$Ti_3C_2 + 2H_2O = Ti_3C_2(OH)_2 + H_2 \quad (14)$$

2.4.2 Advantages. Thermal-assisted electrochemical etching provides a universal method but is also a straight forward approach to MXene synthesis that was difficult previously. The major benefit is that the proportion of active sites increases significantly by increasing the number of O-terminating groups. O-terminating groups facilitate greater adsorption of lithium ions in electrode materials.[86] This approach offers a new pathway for the rapid, straightforward, and safe synthesis of MXenes.[10] It is a "green" and inexpensive synthetic method. The resulting MXene can have excellent activities attributable to relatively greater lateral diameters compared with MXenes obtained in other reported methods.[49]

2.4.3 Drawbacks. The significant problem associated with this method is that when Ti_2AlC (MAX) is subjected to a higher cathodic potential, removal of Ti along with Al layer may occur, which can result in CDC formation. Moreover, the structures of developed MXenes can be damaged by the use of inappropriate electrolytes. A safety risk is increased due to the toxicity of the intercalation.[49]

2.4.4 Precautions and suggestions. The etching setup may be altered so that wires provide electricity during experimentation.[77] It has been suggested that control of key parameters (*e.g.*, voltage, temperature, etching time, electrode preparation and handling) may significantly affect the quality of the MXene obtained.[87]

2.5. Algae extraction etching

Zada *et al.*[58] introduced a new approach that emphasizes the use of vanadium carbide nanosheets (V_2C NSs) to generate MXenes. This methodology involves the intercalating and delaminating of MAX with algal extraction (Fig. 4b). The V_2C NSs exhibited strong structural integrity and excellent NIR absorption.[94] Also, the V_2C NSs exhibited effective photothermal-conversion efficiencies compared with MXenes prepared by other methods.[58] However, this synthetic method has not been applied much.

2.5.1 Advantages. The special feature of the algae extraction etching method is that it is comparatively biocompatible as compared with traditional chemical methods. Also, the raw material (algae) are relatively inexpensive and can be cultivated using sunlight.[95] The quick, easy, low-cost, and high-yielding delamination process creates a novel path for breaking down MAX and creating MXenes with suitable characteristics for various applications.[58] These multiple advantages make this method superior to other approaches used for MXene development.

2.5.2 Mechanism. The MAX, when exposed to algae, transforms into a MXene. The proposed etching process is depicted in eqn (15).

$$V_2AlC + \text{algae} = V_2C + Al - \text{algae} \quad (15)$$

2.5.3 Drawbacks. The etching process is extremely slow and time-consuming. Moreover, control over the purity during etching and its reliability is challenging.

2.5.4 Precautions and suggestions. The composition and properties of algae can vary and may affect the reaction for MXene synthesis. It has been suggested that the species of algae should be selected to avoid unwanted byproducts. Another suggestion is that the species of algae should be characterized before use in etching of the MAX phase.[77]

2.6. Photolithography

A novel and efficient UV-induced selective etching method was proposed by Mei and co-workers.[96] The specialty aspect of this method is that it delivers rapid growth of MXenes in the presence of UV-light. This method propagates in 85% phosphoric acid solution (Fig. 4c). By employing this approach, an exceptional rate potential and stability can be achieved for lithium-ion batteries (LIBs) as well as sodium-ion batteries (SIBs).[97] It has been reported that MXenes obtained *via* this approach, when used as anode material, exhibit promising results. Thus, Mo_2C MXene advanced materials hold great promise for various energy-storage applications.[98,99]

2.6.1 Mechanism. UV irradiation on MAX with acid leads to the formation of a MXene followed by reactions to produce –OH- and –Cl-terminated MXenes. The proposed etching process is depicted in eqn (16)–(18).

$$Mo_2Ga_2C + UV + 6HCl = Mo_2C + 2GaCl_3 + 3H_2 \quad (16)$$

$$Mo_2C + 2H_2O = Mo_2C(OH)_2 + H_2 \quad (17)$$

$$Mo_2C + 2HCl = Mo_2C(Cl)_2 + H_2 \quad (18)$$

2.6.2 Advantages. In this approach, use of hazardous and highly corrosive acids is avoided. MXenes obtained by this method can achieve fine structures with targeted morphologies and properties. Moreover, the product can be reproduced easily using this method. Use of MXene-based batteries can be effective, so MXenes developed by this approach can be widely utilized in energy conversion and energy-storage devices.

2.6.3 Drawbacks. The drawbacks linked with this approach are its high cost, multiple steps and complex reaction process. The complexity of multiple processes increases the chance of errors and can lead to impurities in the final product. The chemicals used can be hazardous and more caution is needed for handling and disposal.

2.6.4 Precautions and suggestions. The substrate must be transparent to pass the UV-light it is exposed to. Similarly, UV-protective glasses and adequate clothing should be used during experimentation. Additionally, exposure time and UV intensity must be optimized to achieve the desired results and target morphologies.[87]

2.7. Hydrothermal synthesis

HF is necessary in most MXene-etching processes.[100] Despite being successful, some procedures are hazardous to the environment. The alkalis used for synthesis are considered to be etching agents due to the powerful affinity for amphoteric elements (*i.e.*, Al, Ga, Pb and Sn).[101] High-purity multilayer MXenes have not been prepared using traditional methods. The main challenge to obtain MXenes *via* alkali attack is the *in situ* formation of oxide or hydroxide layers.[102] Li *et al.* reported a hydrothermal method that used NaOH for the etching of Ti_3AlC_2 (MAX phase) and synthesis of MXene $Ti_3C_2T_x$ (where T_x is –OH, =O). The synthesis *via* a hydrothermal method is illustrated in Fig. 5a. Results indicated that a temperature of 270 °C led to the aluminium layer being proficiently removed with NaOH solution. Using this method, MXenes with –OH and =O terminations and 92% purity have been reported.[103] Peng *et al.*[66] synthesized $Ti_3C_2T_x$ and Nb_2CT_x MXene using hydrothermal etching-assisted by $NaBF_4$/HCl media.

2.7.1 Mechanism. The hydrothermal reaction involves the interaction of the MAX phase with hydroxide ions and water. This results in the formation of –OH- and =O-terminated MXene, along with byproducts and H_2 gas, as shown in eqn (19) and (20):

$$Ti_3AlC_2 + OH^- + 5H_2O = Ti_3C_2(OH)_2 + Al(OH)_4^- + 2.5H_2 \quad (19)$$

$$Ti_3AlC_2 + OH^- + 5H_2O = Ti_3C_2O_2 + Al(OH)_4^- + 3.5H_2 \quad (20)$$

2.7.2 Advantages. By employing a hydrothermal approach, MXenes can be produced quicker compared with HF-etching or other methods. The main advantage is that MXenes developed by the hydrothermal method exhibit more layers compared with that using other traditional methods. Moreover, hydrothermal

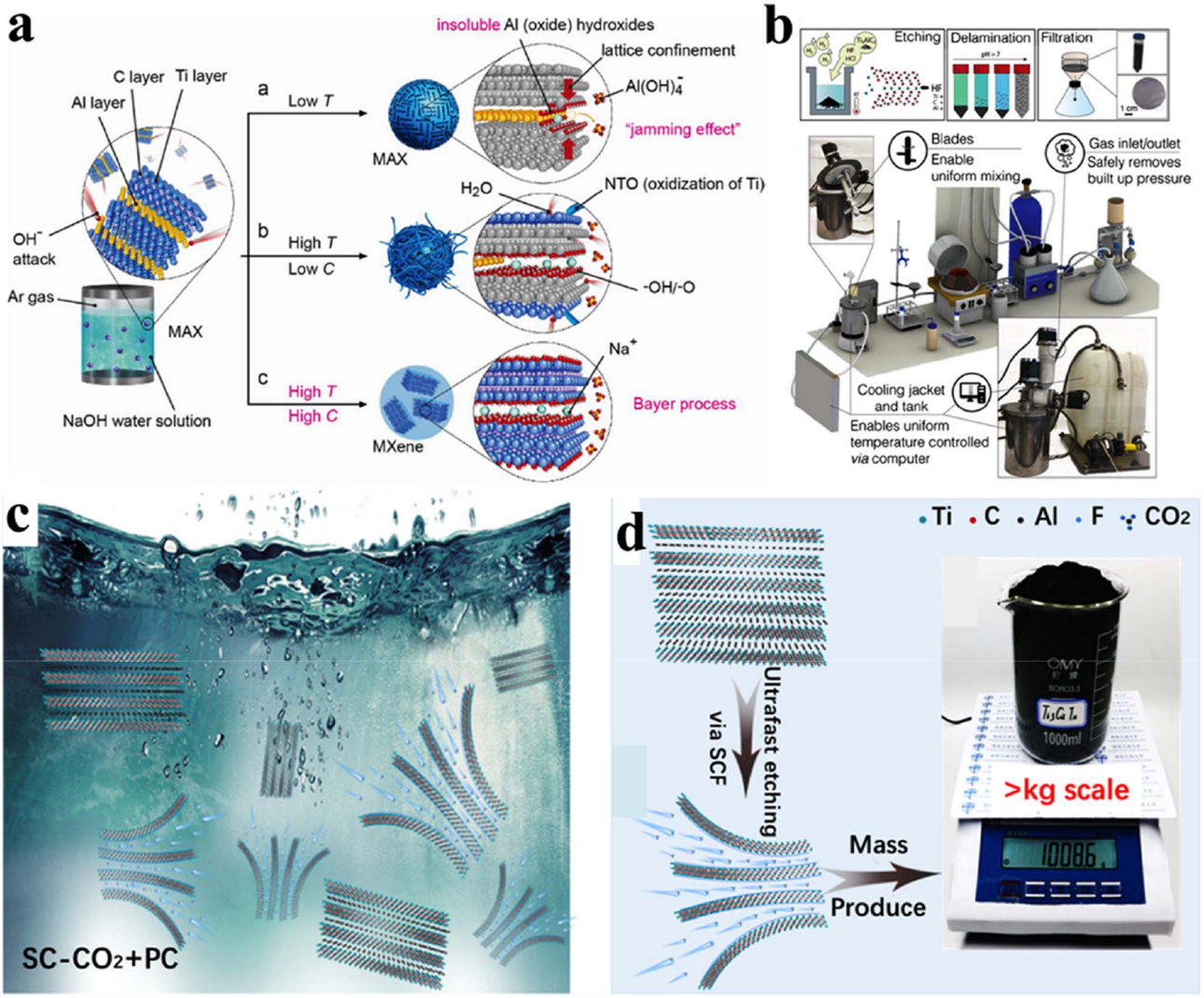

Fig. 5 (a) Representation of hydrothermal synthesis, reproduced from ref. 103 with permission from Wiley, copyright 2018. (b) Synthesis of MXene *via* a scalable approach, reproduced from ref. 67 with permission from Wiley, copyright 2020. (c) Large-scale synthesis of MXenes *via* immersion of Ti_3AlC_2 in PC solution. (d) Etching *via* SCF and obtained $Ti_3C_2T_x$ in kilogramme-scale, reproduced from ref. 109 with permission from Elsevier, copyright 2023.

is a simple and eco-friendly approach that is preferable to other approaches.[104] Also, this method is based on alkali-etching precursors to produce high-purity multilayer MXenes, which is a fluorine-free approach. This method can be utilize for specific and targeted applications.[103] For example, MXenes obtained *via* a hydrothermal method exhibit capacitance 214% greater than that of MXenes prepared by the HF-etching method.[105]

2.7.3 Drawbacks. MXene synthesis *via* a hydrothermal approach typically requires an autoclave reactor, which requires stealth to avoid explosions. Additionally, the hydrothermal reaction requires relatively high temperatures that may oxidize the product. During the hydrothermal reaction, MXene sheets may contain multiple defects on surfaces due to the high rate of particle collision.[106]

2.7.4 Precautions and suggestions. The hydrothermal approach can be dangerous due to the use of high temperatures and pressures. The morphologies of targeted MXenes may alter due to etching at high pressures and airtight environments. It has been suggested that safety measures must be engaged prior to the hydrothermal reaction. Also, a safe environment is needed to avoid explosion of the reactor due to a collapse of temperature or electricity.[77]

2.8. MXene synthesis *via* a scalable approach

Reports have suggested that the synthesis of MXenes can be scaled up to an industrial level, but experimental proof is lacking. In 2022, Shuck *et al.* reported a chemical reactor that was designed for scalable production of MXenes.[67] Then, they compared the amounts of MXene produced using large (50 g) and small (1 g) batches. They predicted no appreciable changes between materials using large and small batches in terms of structural morphology.[107] Sizes of MXene flakes (layers) between

these two batches were nearly comparable. Fig. 5b demonstrates experimental setup of a 1 L MXene reactor along with a 3D model of the apparatus. This system had a cooling tank and interior jacket that ensured maintenance of temperature during the entire reaction. In this protocol, MAX powder was uniformly added using a screw feeder equipped with a gas input accessory. To prevent reactor parts from HF (which can dissolve metal or glass), the mixer and thermocouple jacket were made from a stable polymer (*i.e.* Teflon™).[67,108] Overall, method has been advised for large-scale synthesis of MXenes.

Chen *et al.* developed a supercritical etching method using carbon dioxide as an etchant for the large-scale production of various MXenes ($Ti_3C_2T_x$, Nb_2CT_x, Ti_2CT_x, Mo_2CT_x, and Ti_3CNT_x) (Fig. 5c). Thermally powered supercritical carbon dioxide accelerated the etching rate and gave a yield of ~1 kg (Fig. 5d). The prepared MXenes possessed remarkable charge-storage capacity and ~100% coulombic efficiency.[109]

2.8.1 Mechanism. The supercritical carbon dioxide-assisted reaction involves the etching of MAX with NH_4HF_2, which results in the formation of an –OH-terminated MXene. The proposed etching process is depicted in eqn (21).

$$Ti_3AlC_2 + CO_2 + 3NH_4HF_2 = Ti_3C_2(OH)_2 + (NH_4)_3AlF_6 + 1.5H_2 \quad (21)$$

2.8.2 Advantages. This method can be used for the large-scale synthesis of MXenes. Overall expenditures and per-unit costs can be reduced because a higher yield of product is achieved using a single-step batch reaction using this method. Also, energy consumption using this approach is less as compared with that using other methods.

2.8.3 Drawbacks. Instrumental setup is complicated and is not commercially available. Like other methods, this approach can also be undertaken using HF and CO_2, which are costly and hazardous to handle. Moreover, material disposal or residues after etching merit need extra care to ensure safety.[79]

2.8.4 Precautions and suggestions. The etching process used in this method is highly exothermic, so safety measures must be adopted before starting the reaction. The flow rate of the MAX phase for HF-etching must be controlled carefully. Moreover, special safety equipment (*i.e.*, gloves, goggles, face shield, fume hoods) is needed.

2.9. Iodine-assisted etching

Shi *et al.* reported this method in 2021. Fig. 6a demonstrates the preparation of MXenes using this method.[110] This method involves the use of non-aqueous iodine (I_2) during etching. Initially, $Ti_3C_2I_x$ is formed by subjecting Ti_3AlC_2 to iodine etching in anhydrous acetonitrile at 100 °C. Subsequently, $Ti_3C_2I_x$ is transformed to $Ti_3C_2T_x$ layers, whose diameters become relatively small (~1.8 nm). More than 71% of layers exhibit a thickness <5 nm. The resulting $Ti_3C_2T_x$ flakes reveal exceptional stability even under ambient conditions.[110]

2.9.1 Mechanism. The mechanism involves the sequential reactions of MAX with iodine, oxygen, H_2O and HCl. These reactions result in the formation of an iodine-substituted MXene. Oxidation and subsequent hydrolysis gives an –OH-terminated MXene. The proposed etching process is depicted in eqn (22)–(26).

$$Ti_3AlC_2 + \frac{x+3}{2I_2} = Ti_3C_2 - I_x + AlI_3 \quad (22)$$

$$Ti_3C_2 - I_x + \frac{x}{2O_2} = Ti_3C_2 - O_x + \frac{x}{2I_2} \quad (23)$$

$$Ti_3C_2 - I_x + xH_2O = Ti_3C_2 - (OH)_x + xHI \quad (24)$$

$$AlI_3 + 3H_2O = Al(OH)_3 + 3HI \quad (25)$$

$$Al(OH)_3 + 3HCl = AlCl_3 + 3H_2O \quad (26)$$

2.9.2 Advantages. This approach is relatively simple (in terms of handling) and cost-effective as compared with the other methods reported herein. MXenes produced by this method have high stability, purity and durability. A gelatine approach allows researchers to "fine tune" the morphology of the MXene. Moreover, this approach is protective and relatively environment friendly.

2.9.3 Drawbacks. This approach may require more time to achieve targeted synthesis of MXene nanostructures. The precursors needed in this approach are not widely available as compared with others used in MXene syntheses. Due to its simplicity, this approach requires more attention when setting the reaction conditions.

2.9.4 Precautions and suggestions. Handling of iodine merits attention and care because it is volatile and hazardous. Maintenance of a precise temperature during synthesis is crucial for higher output and accuracy.

2.10. Ion-induced gelation

In 2021, Wang and colleagues[111] reported a quick metal ion-induced gelation approach. Using this method, $Ti_3C_2T_x$ MXene could be modified with minimally intensive layer delamination (MILD). This method involves sequential steps of reactions, washing, and centrifugation to obtain a MXene with a homogeneous monolayer. Additionally, MXene micro-gels were prepared using a MXene in a KOH environment. The resulting mixture delivered a MXene membrane filter (MMF) by vacuum-assisted filtration.[111] Fig. 6b illustrates the scheme of this approach. The effect of MXene delamination *via* dimethyl sulfoxide is explained in ESI Section S1.‡

2.10.1 Mechanism. Ion-induced gelation occurs as NaOH ions interact with $Ti_3C_2T_x$, which leads to the formation of MXene layers. This approach is depicted in eqn (27).

$$Ti_3C_2T_x + NaOH_{(aq)} = \text{MXene layers} + \text{byproducts} \quad (27)$$

2.10.2 Advantages. This approach is new and easy to handle. This method is unique due to mild processing conditions (*i.e.*, no extra-heat, no excessive solvents, or hazardous

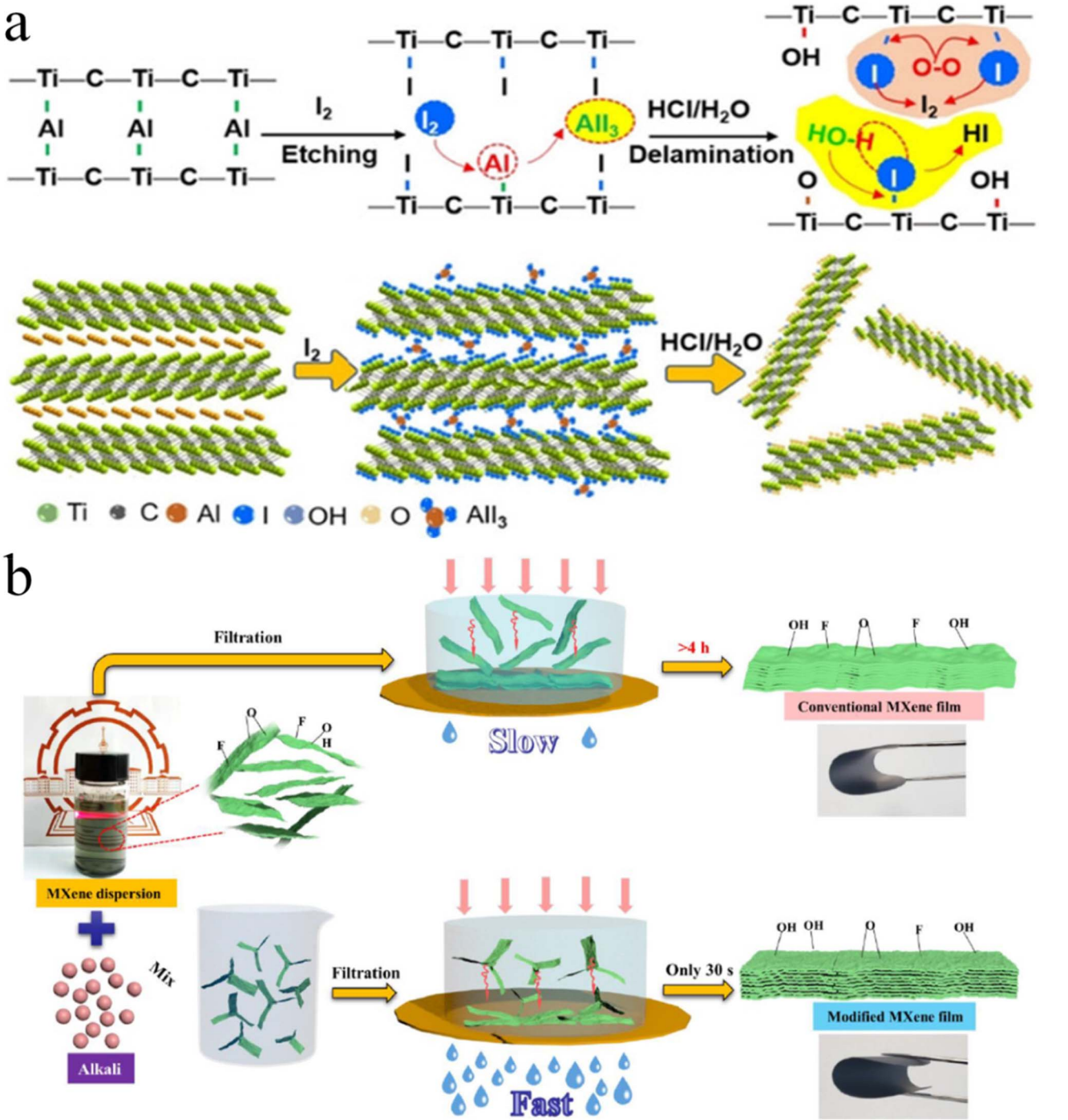

Fig. 6 (a) Iodine-assisted etching and delamination of Ti_3AlC_2, reproduced from ref. 110 with permission from Wiley, copyright 2021. (b) Schematic illustration of synthesis, reproduced from ref. 111 with permission from *Engineered Science*, copyright 2021.

environmental toxins). Moreover, this method is tuneable so it can be handled/computed with modern accessories.

2.10.3 Drawbacks. Scale-up of this method to an industrial setup has been done. This method has not been commercialised because it is a very recent approach (reported in 2021 by Wang and colleagues).[111] MXenes prepared by this method have not been tested on modern analytical instruments.

2.10.4 Precautions and suggestions. Selection of appropriate precursors must be compatible with an ion-induced approach.[87] Laboratory-based experiments should be undertaken to optimize the synthesis parameters.[77]

2.11. Other synthetic methods

Various other synthetic methods, including gas-phase synthesis and chemical vapour deposition (CVD), have also been

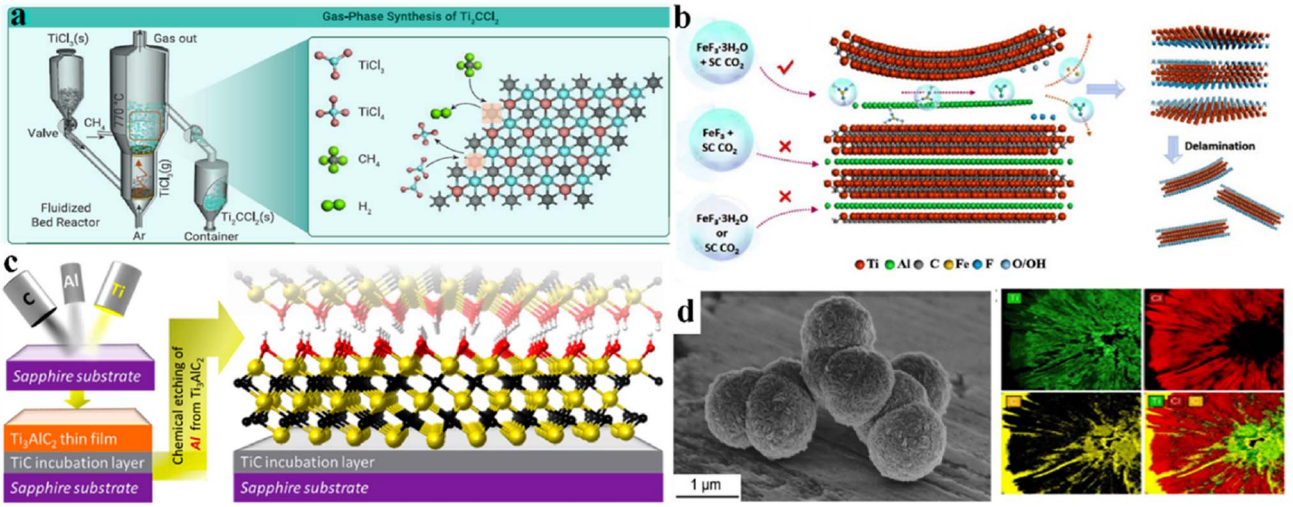

Fig. 7 (a) Gas-phase synthesis of Ti_2CCl_2 reproduced from ref. 82 with permission from ScienceDirect, copyright 2023. (b) CO_2-assisted synthesis of MXenes, reproduced from ref. 112 with permission from Royal Society of Chemistry, copyright 2023. (c) Magneto supporting for MXene synthesis, reproduced from ref. 76 with permission from American Chemical Society, copyright 2014. (d) SEM results and elemental maps of MXenes prepared *via* chemical vapour deposition, reproduced from ref. 113 with permission from *Science*, copyright 2023.

employed for the fabrication of MXenes. Each method offers distinct advantages and characteristics suitable for specific applications.

Xiang *et al.* utilized a fluidized bed reactor (FBR) for the synthesis of Ti_2CCl_2 through gas-phase synthesis (Fig. 7a). Solid $TiCl_3$ precursors were sublimated at 770 °C and reacted with CH_4 in the FBR to produce Ti_2CCl_2 (MXene). Approximately 100 g of MXene was generated per batch.[82] The synthesis mechanism is given in eqn (28) and (29):

$$6TiCl_3 + CH_4 = Ti_2CCl_2 + 4TiCl_4 + 2H_2 \quad (28)$$

$$2TiCl_3 + CH_4 = 2Ti_2CCl_2 + 4HCl \quad (29)$$

Feng *et al.* used supercritical (SC) CO_2 to etch MAX in the solid phase. They observed that SC CO_2 with $FeF_3 \cdot 3H_2O$ could synthesize and delaminate multilayer MXenes (Fig. 7b).[112] The synthesis mechanism is given in eqn (30)–(33):

$$Ti_3AlC_2 + 3FeF_3 \cdot 3H_2O + 3xCO_2 = Ti_3C_2 + AlF_3 + 9H_2O + [Fe(CO_2)_xF_2] \quad (30)$$

$$Ti_3C_2 + 3FeF_3 \cdot 3H_2O + 2xCO_2 = Ti_3C_2(F)_2 + 6H_2O + 2[Fe(CO_2)_xF_2] \quad (31)$$

$$Ti_3C_2 + H_2O = Ti_3C_2(OH)_2 + H_2 \quad (32)$$

$$Ti_3C_2 + H_2O = Ti_3C_2(O)_2 + H_2 \quad (33)$$

Halim *et al.* reported the fabrication of Ti_3C_2 films *via* targeted removal of aluminium from sputter-deposited MAX film. Aqueous HF and NH_4HF_2 were used for selective etching (Fig. 7c).[76] The synthesised MXene transmitted 90% of visible light and infrared light, and exhibited metallic conductivity down to 100 K. The synthesis mechanism is given in eqn (34)–(37):

$$Ti_3AlC_2 + 3HF = Ti_3C_2 + AlF_3 + 1.5H_2 \quad (34)$$

$$Ti_3C_2 + 2H_2O = Ti_3C_2(OH)_2 + H_2 \quad (35)$$

$$Ti_3C_2 + 2HF = Ti_3C_2F_2 + H_2 \quad (36)$$

$$Ti_3AlC_2 + 3NH_4HF_2 = (NH_4)_3AlF_6 + Ti_3C_2 + 1.5H_2 \quad (37)$$

$$Ti_3C_2 + aNH_4HF_2 + bH_2O = (NH_3)_c(NH_4)_dTi_3C_2(OH)_xF_y \quad (38)$$

MXenes are typically produced by etching MAX phases. Wang *et al.* introduced a novel method to synthesize MXenes by utilizing CVD, even for MXenes that have not been derived from MAX phases. They established a direct and scalable synthetic pathway for MXenes by reacting CH_4 with $TiCl_4$, $ZrCl_4$, or $ZrBr_4$. This approach involves the reactions of metals and metal halides with graphite, methane, or nitrogen. Direct synthesis facilitates the growth of MXenes in various diverse morphologies rather than a conventional layered structure (Fig. 7d). The synthesised MXenes from this method demonstrated impressive energy-storage capacity[113]

2.11.1 Advantages. Gas-phase synthesis offers precise control for MXene synthesis without forming thermodynamically stable TiC. It allows continuous operation and scalable production to industrial levels. CVD enables the synthesis of MXenes that cannot be conventionally derived from MAX phases. CVD offers a direct route of synthesis without need for MAX phase precursors. This method leads the synthesis of MXenes with diverse morphologies beyond conventional layered structures.

2.11.2 Drawbacks. The handling of multiple precursors can add complexity to the synthesis. Additionally, achieving

Table 1 Year-wise summary of different MXene materials developed *via* various synthetic strategies, terminations, and characterizations for useful applications

Year	MXene	Synthetic strategy	MAX precursor	Surface termination	Film thickness (nm)	Characterizations	Applications	Ref.
2011	Ti_3C_2	HF treatment	Ti_3AlC_2	–OH, –F	1.2	XRD, Raman, XPS, SEM, TEM & HRTEM	Synthesis of carbides and nitrides of Ti, V, Cr, Nb, Ta, Hf and Zr	80
2012	Ti_2C	HF treatment	Ti_2AlC	OH, –F	N/A	XRD & CV	LIBs	114
2012	Ti_2C	HF treatment	Ti_2AlC	=O, –F	N/A	SEM, BET & CV	LIBs	115
2012	Ti_3C_2	HF treatment	Ti_3AlC_2	–OH, –F	N/A	DFT, NEB & PAW method	LIBs	116
2013	Nb_2C	HF treatment	Nb_2AlC	=O, –F, –OH	N/A	XRD, XPS, SEM	LIBs	117
2013	V_2C	HF treatment	V_2AlC	=O, –F, –OH	N/A	XRD, XPS, SEM	LIBs	117
2014	Ti_3C_2	HF treatment	Ti_3AlC_2	=O, –F, –OH	<20	XRD, SEM, EDX, FT-IR & UV-vis-DRS	Electrochemical biosensors	118
2014	MXene-Cu_2O	HF treatment	Ti_3AlC_2 and $Cu(CH_3COO)_2 \cdot H_2O$	=O, –F, –OH	30 ± 10	XRD, FESEM & TG-DSC	Thermal decomposition of ammonium perchlorate (AP)	119
2014	Ti_3C_2	CO_2-assisted solid phase etching	Ti_3AlC_2	–Fe, =O, –F	N/A	SEM, TEM, AFM, XPS, & IR	HER	112
2015	Ti_2CT_x	HF treatment	Ti_2AlC	–OH –F=O	0.028	XRD, Raman, XPS, BET, SEM, TEM & HRTEM	Super capacitors	120
2015	$(Nb_{0.8}Ti_{0.2})_4C_3T_x$	LiF/HCl solution	$(Nb_{0.8}Ti_{0.2})_4AlC_3$	–OH –F=O	N/A	XRD, SEM, TEM, & XPS	Energy storage	121
2015	$(Nb_{0.8}Zr_{0.2})_4C_3T_x$	HF treatment	$(Nb_{0.8}Zr_{0.2})_4AlC_3$	–OH –F=O	N/A	XRD, SEM, TEM, & XPS	Energy storage	121
2015	$Ti_3C_2T_x$	Dilute HF	Ti_3AlC_2	–OH –F=O	0.9 ± 0.3	SEM, TEM, BET & XRD	High performance super capacitor	122
2015	Mo_2C	HF treatment	Mo_2Ga_2C	–OH –F=O	N/A	SEM, TEM-EDX & XRD	N/A	123
2016	Mo_2CT_x	HF/mixture of LiF and HCl	Mo_2Ga_2C	–OH, –F, =O	0.02	SEM, TEM, XRD & XPS	LIBs and super capacitors	124
2016	$Ti_3C_2T_x$	Ultra-sonication	Ti_3AlC_2	–F and =O	0.002–90	SEM, TEM, EDX & XRD	Water treatment & biomedical applications	125
2016	$Zr_3C_2T_z$	HF treatment	$Zr_3Al_3C_5$	–OH, –F, =O	N/A	XRD, SEM, TEM, TGA-DSC & XPS	N/A	126
2017	Ti_2N	KF + HCl	Ti_2AlN	–OH, –F, =O	N/A	XRD, Raman, SEM, EDX, XPS	SERS substrate	127
2017	$Hf_3C_2T_z$	HF etching	$Hf_3[Al(Si)]_4C_6$	–OH, –F, =O	0.9	XRD, SEM, TEM, AFM	Electrochemical	128
2017	Ta_4C_3	HF etching	Ta_4AlC_3	OH, –F, =O	1.00	XRD, SEM, TEM, Raman, XPS, DFT	Anticancer	129
2018	V_2C	NaF + HCl	V_2AlC	–OH, –F, =O	0.854	XRD, SEM, EDX, Raman& TG-DTA	Reported thermal stability of V_2C	130
2018	$W_{1.33}CT_x$	LiF + HCl	$(W_{1.5}Y_{0.3})_2AlC$	–OH, –F, =O	—	TEM, XRD, DFT	HER	131
2019	=O terminated $Ti_3C_2T_x$	HF treatment + *n*-butyllithium-treated method	$Ti_3C_2T_x$	=O	N/A	SEM, XPS, BET & XRD	High performance pseudo capacitors	132
2020	Scalable synthesis of $Ti_3C_2T_x$	HF treatment	Ti_3AlC_2	–OH, –F, =O	0.007	SEM, XRD, Raman, XPS & UV-vis	Scale-up synthesis	67
2020	Sc_2CO_x	Sputtering	—	–OH, –F, =O	N/A	XPS, PL, DRS	Optical properties study	133
2020	Cr_2CT_x	$FeCl_3$ + $C_6H_6O_6$ etching	Cr_2AlC	=O, –OH	N/A	SEM, EDS, XRD, Raman, TEM, FTIR, XPS	Hydrazine detection	134
2020	Y_2CF_2	Solid-state reactions	Y2C + YC + YF_3	–OH, –F	N/A	XRD, DRS, SEM, XPS	Photocatalytic activity	135
2021	Ti_2C, Nb_2C, V_2C, Mo_2C, Ti_3C_2, and Nb_4C_3	Various chemical environments	Ti_2AlC, Nb_2AlC, V_2AlC, Mo_2AlC, Ti_3AlC_2 and Nb_4AlC_3	O, OH, N, NH, NH_2, S, SH, H, F, Cl, Br, and I	N/A	DFT, final state approximation, NEB & dimer method	New synthesis routes	84
2021	ZrC	Sputtering	—	—	N/A	SEM, Raman, AFM	Lock fiber lasers	136
2021	$Ti_3C_2T_x$	LiF + HCl	Ti_3AlC_2	N/A	N/A	SEM, AFM, TEM, EDX & XPS	Electrical wiring and signal transmission	137
2022	TMSe@MXene	HF treatment	$Ti_3C_2T_x$ & Nb_2CT_x	=O	N/A	SEM, TEM, HRTEM, STEM, XRD, XPS& BET	ZIBs	138
2022	MXene/CAC films	LiF + HCl	$Ti_3C_2T_x$	–F, –OH	N/A	SEM, TEM, HRTEM, STEM, EDS, XRD, XPS, TGA, FT-IR, BET & DFT	Super capacitors	139

Table 1 (*Contd.*)

Year	MXene	Synthetic strategy	MAX precursor	Surface termination	Film thickness (nm)	Characterizations	Applications	Ref.
2023	PDPZ@MXene	Vacuum-assisted filtration technology	PDPZ and MXene	–F, –OH	—	SEM, TEM, NMR, XRD, SAED, Raman & FT-IR	Super capacitors	140
2023	V_2N	HF treatment	V_2AlN	–OH, –F, =O	3.7	SEM, TEM, XRD, XPS	Anti-effective therapy	141
2023	MXene@Co_9S_8/$CoMo_2S_4$	HF treatment and sulfidation	Ti_3AlC_2	–F, –OH, =S	1.37	XRD, FE-SEM, EDS, TEM & XPS	SIBs	142
2023	GN/MXene/FeS foam	Hydrothermal	rGO, MXene, FeS	–OH, –F, =O	N/A	SEM, XRD & XPS	Electromagnetic absorption	143
2023	Ti_2CCl_2 Zr_2CCl_2 Zr_2CBr_2	CVD	$CH_4 + TiCl_4$ $CH_4 + ZrCl_4$ $CH_4 + ZrBr_4$	–Cl, –Br	N/A	FBI-SEM, AFM, TEM, XRD, Raman, STEM, XRF, XPS	Energy storage	113
2024	Pd@$Ti_3C_2T_x$	HF etching + wet impregnation	Ti_3AlC_2	–OH, –F, =O	N/A	XRD, SEM, XPS, UV-VIS/DRS	Water splitting	144
2024	Ti_2CCl_2	Gas phase	$TiCl_3 + CH_4$	–Cl	N/A	XRD, SEM, AFM, STEM, HRTEM, EPR	LSBs	82

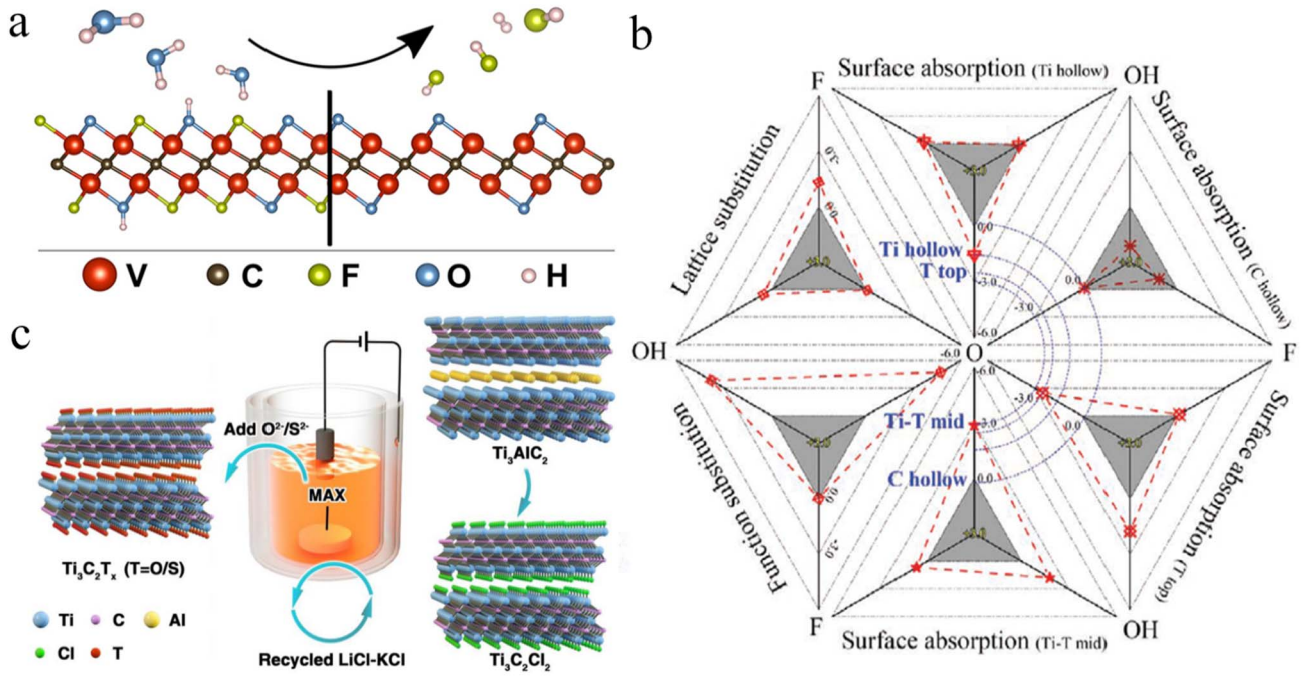

Fig. 8 (a) Removal of fluoride terminations by gas hydrolyzation, reproduced from ref. 147 with permission from American Chemical Society, copyright 2022. (b) Simulation with nitrogen dopants in Ti_3C_2, reproduced from ref. 149 with permission from Wiley, copyright 2020. (c) MXene synthesis by molten salt etching, reproduced from ref. 151 with permission from Wiley, copyright 2021.

uniform and controlled growth of MXenes with diverse morphologies might create challenges in maintaining consistent properties during large-scale production.

2.11.3 Precautions and suggestions. To maintain consistent surface chemistry and excellent conductivity across batches, continuous optimization of synthesis conditions and parameters is needed. Safety protocols must be followed while operating the FBR for MXene synthesis. Reaction parameters (*e.g.*, temperature, pressure and precursor ratios) must be standardized to maintain reproducibility and ensure consistent MXene properties. To identify ideal conditions for uniform MXene growth, systematic experimentation and testing are necessary.

Numerous methods that have been reported for the synthesis of MXene *via* various synthetic strategies, terminations, and characterizations for useful applications are shown in Table 1.

3. Insights into the doping and scope of MXene terminations

3.1. MXene terminations

Diverse compositions and a complex nature of terminations are involved in various etching methods. Despite inadequate scrutiny regarding the impact on MXene applications, researchers are striving to enhance performance by modifying the terminations linked to synthetic approaches.[145] Surface variations and element doping on MXene terminations have been extensively reported, particularly for battery and supercapacitor applications. The choice of etching method is important because it can affect surface terminations.[146] MXenes produced through fluorine-based etching methods typically exhibit terminations such as –OH, =O, and –F.[60] Alkali and electrochemically assisted etching methods yield non-F-terminated MXenes but with lower efficiency.[10] Methods involving molten salt etching generally result in the production of a single termination that can substituted *via* substitution reactions.[55] Gas hydrolyzation has been found (Fig. 8a) to be very effective to substantially reduce F terminations.[147] By employing gas hydrolyzation, oxygen (O) content remains relatively stable at ~0.3 per unit formula of V_2CT_x. Some studies claim that, by doping MXenes with heteroatoms such as nitrogen (N) or sulfur (S), the electrical properties of supercapacitors are significantly enhanced.[148] For example, if nitrogen is introduced into $Ti_3C_2T_x$ frameworks, its thermal stability changes, thus improving its activities.[149] A similar study was done for supercapacitors by annealing MXene in an ammonia environment.[150] Fig. 8b illustrates that simulation of nitrogen dopants in Ti_3C_2. LiCl, or KCl has been utilized to synthesize Cl-terminated MXenes using electrolysis. Similarly, upon addition of Li_2O/Li_2S to the molten state, MXenes with –O or –S have been prepared[151] (see the scheme in Fig. 8c).

In 2019, Schultz *et al.* reported photoelectron spectroscopy (PES) and density functional theory (DFT) for computational studies.[152] They investigated the electronic properties of $Ti_3C_2T_x$ having different surface terminations. Fig. 9a demonstrates different adsorption sites on $Ti_3C_2T_x$ that were computed *via* DFT studies.[153] Fig. 9b exhibits the XPS core-level spectra of $Ti_3C_2T_x$. For the three sets of spectra: one is for its loaded state (lower row); second one is for annealed MXene at 470 °C (middle row); third one is for a MXene annealed at 750 °C (upper row).[152] In Fig. 9b, solid lines exhibit curve-fitting, whereas hollow circles indicate data points. The left side displays confirmation of estimated terminations at various temperatures. Fig. 9c demonstrates work functions that govern due to surface terminations with justifications about actual surface stoichiometric ratios. In Fig. 9c, the blue line represents calculated work functions, whereas red lines exhibit the experimentally determined stoichiometric values of $Ti_3C_2O_2$, $Ti_3C_2F_4$, $Ti_3C_2OH_2$, and Ti_3C_2.[152]

3.1.1 Fluorine-terminated MXenes. The most suitable method for fabricating MXenes with F-terminations is HF etching.[154] These are mostly utilized as cathodes in aqueous zinc-ion batteries. Halogenated MXenes exhibit exceptional performances as cathodes because they offer a stable platform, high energy density, and excellent rate performances.[155,156] Similarly, rich F-terminated MXenes have been found to be effective electrocatalysts for the HER.[51] Some studies have shown that F-terminations enhance the photocatalytic activities of Ti_3C_2 by increasing its hydrophilicity.[157] Additionally, F-terminations aid the adsorption of various pollutants at the surface of Ti_3C_2.[158] For example, methylene blue (MB) in

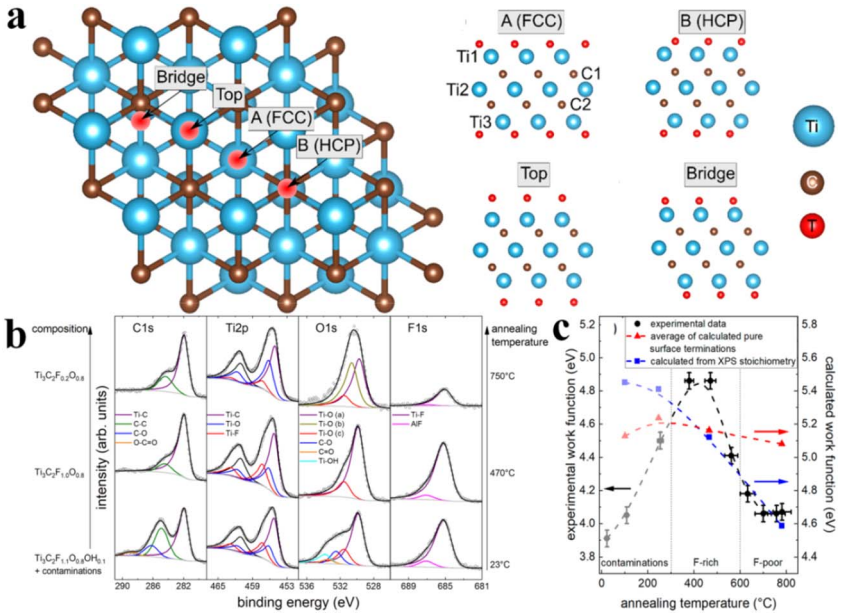

Fig. 9 (a) Adsorption sites on $Ti_3C_2T_x$ according to DFT calculations. The FCC adsorption site is located on top of a Ti atom in the third atomic layer. HCP was exhibited on top of a C atom in the second atomic layer. (b) XPS core-level spectra of $Ti_3C_2T_x$. (c) Work functions of different surface terminations calculated by DFT, reproduced from ref. 152 with permission from American Chemical Society, copyright 2019.

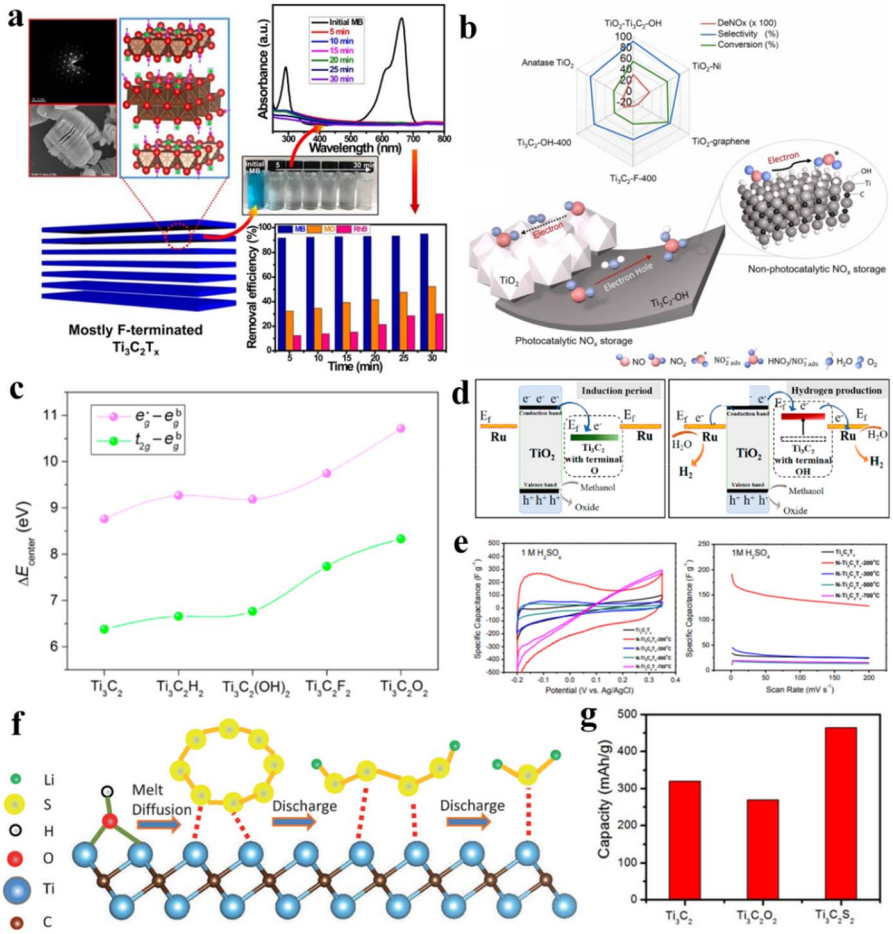

Fig. 10 (a) F-terminated $Ti_3C_2T_x$ MXene used for the removal of methylene blue, reproduced from ref. 358 with permission from Elsevier, copyright 2021. (b) OH-terminated MXene used for photocatalytic reactions, reproduced from ref. 160 with permission from Elsevier, copyright 2022. (c) Energy differences between Ti_2 3d orbitals in unterminated and terminated MXenes along with their stability order, reproduced from ref. 162 with permission from American Chemical Society, copyright 2017. (d) Charge exchange during photoreactions, reproduced from ref. 169 with permission from American Chemical Society, copyright 2020. (e) Comparative CV results obtained at a scan rate of 1 mV s^{-1}, reproduced from ref. 189 with permission from Elsevier copyright 2017. (f) Heat-treatment interaction with polysulfides, reproduced from ref. 188 with permission from Wiley, copyright 2015. (g) Maximum carrying capacities of Ti_3C_2, $Ti_3C_2O_2$, and $Ti_3C_2S_2$, reproduced from ref. 173 with permission from Royal Society of Chemistry, copyright 2018.

wastewater can be effectively adsorbed on F-terminated $Ti_3C_2T_x$ MXene (Fig. 10a). The effect of Lewis-basic halides on MXenes is explained in ESI Section S3.‡

3.1.2 Hydroxyl-terminated MXenes. Hydroxyl terminations can help to capture and activate CO_2 molecules.[159] MXenes synthesized *via* molten salt etching have been reported to be effective because negative electrodes are much better for applications based on electrochemical energy storage.[89] In order to synthesize an –OH-terminated MXene ($Ti_3C_2OH_x$), Al Mayyahi *et al.*[160] reported a one-step hydrothermal process involving alkali-assisted aluminium etching in NaOH along with hydrazine as a delaminating agent. The special feature of $Ti_3C_2OH_x$ is that it exhibits strong synergism with TiO_2 as a co-catalyst during the oxidation of NO_x,.[160] Moreover, –OH-terminations exhibit higher selectively for targets during photocatalytic reactions.[161] See the –OH terminations in Fig. 10b. Quantitatively, the stability order is $Ti_3C_2O_x$ > $Ti_3C_2F_x$ > Ti_3C_2-OH_x > $Ti_3C_2H_x$ > Ti_3C_2 [162] (Fig. 10c).

3.1.3 Oxygen-terminated MXenes. Oxygen termination is preferred for energy-storage applications such as super-capacitors and lithium-ion batteries.[163] The surface of =O-terminated MXenes provides extra stability and electrochemical performances in energy-storage devices.[164] Additionally, =O termination facilitates better interactions with electrolytes that extend charge-storage capabilities.[165] Although, –OH functional groups cannot hold sufficient capacitance as compared with =O terminations. Thus, –OH functional groups can be decreased to increase capacitance by an annealing approach.[166] =O terminations on the surface of Ti_3C_2 can have a significant effect on its photocatalytic performance because =O terminations can act as electron-acceptors. Additionally, =O terminations can increase the surface area of Ti_3C_2, thereby providing more active sites for photocatalytic reactions to occur. H^+ can be reduced with =O terminations specifically in acidic electrolytes.[162,167] However, too many =O terminations can also have negative effects on photocatalytic performance.[168]

Excessive =O terminations can result in the formation of oxygen vacancies that can act as recombination centres. These recombination sites can affect the overall efficiencies of Ti_3C_2-based catalysts.[169] For evaluation, see Fig. 10d. However, a moderate number of =O terminations has been suggested for optimal photocatalytic performances.[170] The optimal amount of =O terminations depend on the specific application and reaction conditions.[160]

3.1.4 Sulfur-terminated MXenes. Metal–sulfur batteries have high energy-storage density. Lithium–sulfur batteries have been found to be more attractive for energy-storage applications.[171] Recent studies have demonstrated that S-terminated MXenes could be utilized as anode materials. Fig. 10f demonstrates heat-treatment interactions between polysulfides and Ti–OH on the surface of Ti_3C_2. According to Mehta *et al.*,[172] S-terminated Mo_2C (MXene) significantly boosted Li adsorption capacity that led to higher performances. Fig. 10g illustrates a comparison of the maximum charge-carrying capacities of Ti_3C_2, $Ti_3C_2O_2$, and $Ti_3C_2S_2$ (the maximum carrying capacity of a material refers to its ability to host or store a certain substance or molecule[146]). The presence of =S facilitates stronger adsorption/chemical reactions, enabling it to host/store a greater amount of substances, resulting in a higher maximum carrying capacity compared with Ti_3C_2 and $Ti_3C_2O_2$.[173] Extra detail of this section has been included ESI Section S4.‡

3.1.5 MXenes with mixed/other terminations. Since the discovery of $Ti_3C_2T_x$, over 30 MXenes with diverse M and X elements have been reported. MXene properties are significantly influenced by surface terminations that offer various opportunities to optimize them for targeted applications. Natu *et al.* presented their perspectives on termination engineering and their impact on MXene properties.[174] They stated that various terminations (*e.g.*, =O, –OH, –F, –Cl, =S, =NH) could be introduced to fabricate MXene surfaces (*i.e.*, $Ti_3C_2Cl_x$, $Ti_3C_2Br_x$, $Ti_3C_2S_x$) (Fig. 11a). Different methods have been reported to fabricate MXene surfaces, but control over MXene terminations is not possible by etching of the MAX phase through fluorine-based acids. Acid etching covers MXene surfaces with –F, –Cl, –Br, –I, =O or –OH terminations (Fig. 11b). Halogen-based surface terminations can be removed and replaced by post-etching processes. As discussed in the "Synthesis" section, molten salts such as $ZnCl_2$ and $CuCl_2$ can remove the A-layer by a Lewis acid–base reaction (Fig. 11c). This method facilitates obtaining homogeneous and single halogen-terminated MXenes. In 2023, Ding *et al.* produced MXenes with =S, =Se, =Te and Sb terminations (Fig. 11d).[175]

Hope *et al.* quantified the surface terminations of $Ti_3C_2T_x$ using ^1H, ^{13}C and ^{19}F NMR (Fig. 11e–g). A lower concentration of –OH terminations in LiF and HF etched Ti_3C_2 compared with –F and =O terminations was noted. Specifically, –F terminations are more prevalent in the HF method, whereas =O

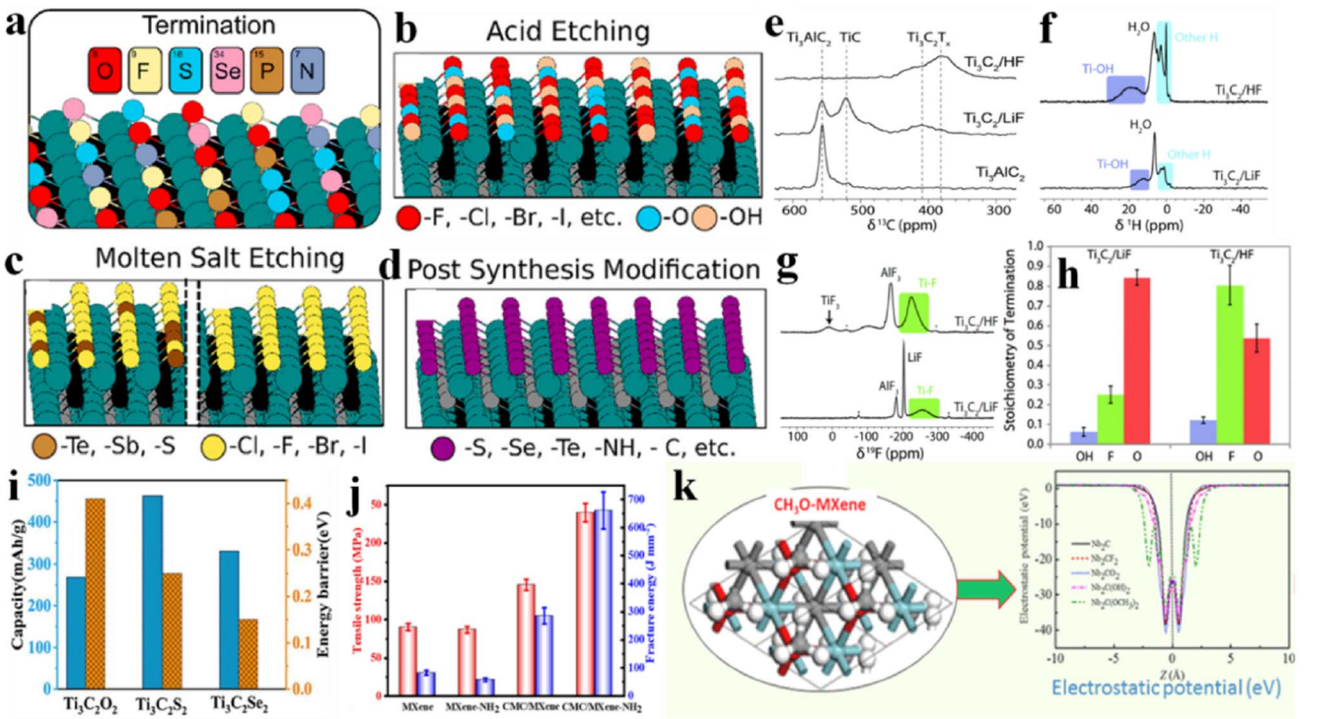

Fig. 11 (a) Surface terminations of MXenes by (b) acid etching, (c) molten salt etching, and (d) post-synthesis modifications, reproduced from ref. 174 with permission from American Chemical Society, copyright 2023. (e) ^{13}C NMR, (f) ^1H NMR, and (g) ^{19}F NMR of HF- and LiF-etched Ti_3C_2, and (h) comparison of surface compositions of LiF- and HF-etched $Ti_3C_2T_x$, reproduced from ref. 176 with permission from Royal Society of Chemistry, copyright 2016. (i) Comparison of storage capacity and energy barrier for =O, =S, and =Se terminated MXenes, reproduced from ref. 177 with permission from Elsevier, copyright 2020. (j) Tensile strength and fracture energy of $–NH_2$-terminated MXenes, reproduced from ref. 85 with permission from Elsevier, copyright 2021. (k) CH_3–O-terminated Nb_2C as an electrode and its potential, reproduced from ref. 178 with permission from Elsevier, copyright 2017.

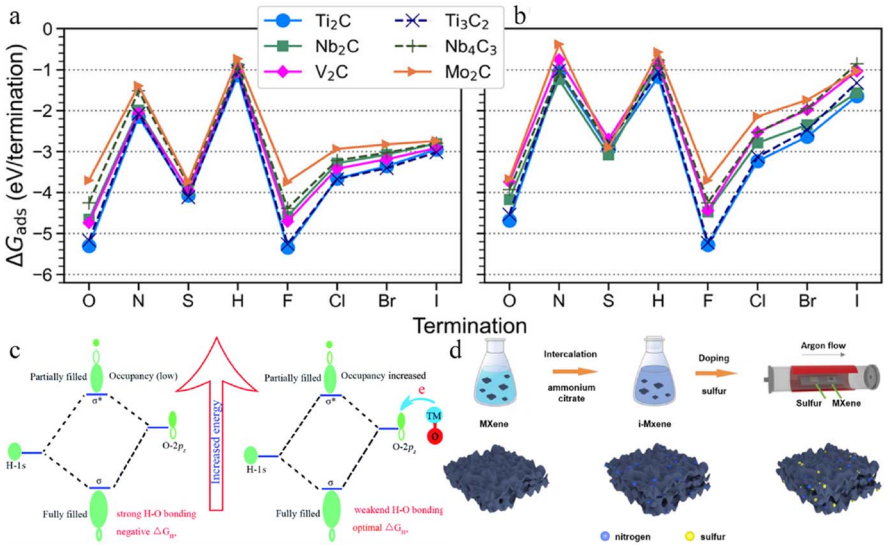

Fig. 12 Adsorption free energy of various terminations over different MXenes: (a) low ($x = 1/8$) and (b) full coverage ($x = 2$), reproduced from ref. 84 with permission from American Chemical Society, copyright 2021. (c) Impact of doped metal on Cr_2CO_2 for the HER, reproduced from ref. 182 with permission from Royal Society of Chemistry, copyright 2018. (d) Two-step intercalation and annealing for generating N/S-doped MXenes, reproduced from ref. 184 with permission from Elsevier, copyright 2022.

terminations dominate in the LiF (*in situ* HF etching) method. These proportions exhibit high sensitivity to the synthetic method utilized (Fig. 11h).[176]

Li *et al.* studied the role of =O, =S, =Se and =Te terminations over Ti_3C_2 for Li-ion batteries. Interestingly, these terminations maintained the metallic band structure and exhibited low Li-ion diffusion barriers of 0.25 and 0.15 eV for $Ti_3C_2S_2$ and $Ti_3C_2Se_2$, respectively. Furthermore, these terminations improved the mechanical strength of Ti_3C_2 anodes, which effectively addressed the issue of electrode pulverization (Fig. 11i).[177]

Peng *et al.* compared the tensile strength and fracture energy of pristine MXenes with $-NH_2$ terminated MXenes. $-NH_2$ terminations increased the tensile strength (Fig. 11j). The enhanced mechanical properties were primarily attributed to the hydrogen bonding between NH_2-MXene and CMC.[85] The mechanism of the enhanced strength of NH_2-terminated MXenes is explained in ESI Section S2.‡ Xin *et al.* functionalized Nb_2C with $-OCH_3$ terminations, and showed ultralow work function (1.0 eV) potential (Fig. 11k) in field emitters.[178]

Björk *et al.* theoretically explored 12 distinct terminations (=O, –OH, ≡N, =NH, $-NH_2$, =S, –SH, –H, –F, –Cl, –Br, and –I) over six MXenes (Ti_2C, Nb_2C, V_2C, Mo_2C, Ti_3C_2, and Nb_4C_3). The adsorption free energies at low and full coverage (Fig. 12a and b) revealed that all species energetically favoured adsorption on MXenes, with Ti_2C and Ti_3C_2 displaying the strongest adsorption and Mo_2C the weakest. In the case of terminations, a consistent trend was observed regardless of chemical potential. Notably, –F and =O terminated MXenes exhibited the most favourable adsorption free energies.[179]

3.2. Doped MXenes

To enhance the effectiveness of MXene for targeted applications, substituting elements (doping) at M or X sites is a promising strategy. For this purpose, various methods have been reported, such as thermal annealing, thermal sintering, solvothermal and hydrothermal approaches, coprecipitation method, and strong electrostatic adsorption.[180]

3.2.1 Doping in M sites. The exceptional properties of MXenes are largely attributed to the accessible d-orbitals of metal atoms. Khazaei *et al.* predicted that bandgap energies decrease (*e.g.*, $Hf_2CO_2 > Zr_2CO_2 > Ti_2CO_2$) as the size of the metal atom decreases.[181] This indicates doping has the potential to alter the intrinsic properties of MXenes. The incorporation of two transition metals in MXene structures lead to exhibition of the distinct characteristics of the two transition metals. In Cr_2CO_2 (MXene), introduction of electron-donor transition metals can effectively reduce the ability of O* to accept extra electrons from H* (Fig. 12c), thereby weakening their interaction and eventually improving the HER activity.[182]

3.2.2 Doping in X sites. Balcı *et al.* investigated the electronic properties of X-doped Sc_2CF_2 (MXene) by substituting C atoms with F, S, Si, Ge, Sn, B, N, or B + N. They demonstrated that doping caused variations in bandgap and transitions between semiconductor and metal states.[183] For the co-doping of N and S, the MXene was intercalated in the presence of ammonium citrate and annealed with sulfur in an argon gas stream for 2 h (Fig. 12d)[184]. Despite the significant impact on MXene properties, elemental doping at X sites has garnered more attention after the discovery of oxycarbides.[185]

Notably, recent modifications in MXenes by partial substitution of carbon or nitrogen with oxygen from the MXene lattice are known as “oxycarbides” or “oxynitrides”. Oxycarbide MXenes reported so far exhibit <50% oxygen in their lattice. The incorporation of oxygen can control the structures and properties of MXenes. The research community has made significant progress in addressing challenges and achieving uniform surface terminations. However, further research is necessary to

understand the arrangement of X-site atoms. 2D borides (MBenes or boridenes) exist as a separate group due to their distinct crystal structure.[186]

The development of sulfur-based electrodes in batteries addresses several challenges. Generally, sulfur is loaded onto conductive materials having a porous nature (*e.g.*, carbon, MXene). MXenes are now regarded as the best sulfur host materials due to their success in suppressing the shuttle effect of polysulfides.[187] Ti_2CT_x/S was initially developed as a cathode material for lithium–sulfur batteries (LSBs) by Liang *et al.* in 2015.[188] This is the main reason why there has been increased research on utilizing MXenes in metal–sulfur batteries. A nitrogen-doped MXene, N–$Ti_3C_2T_x$, can be produced by ammonia post-etch annealing[189] and with plasma treatment.[190] Due to its large surface area and higher pore volume, it exhibits exceptional electrochemical capabilities for LSB applications.[149] Lu *et al.*[149] investigated the atomic positions and effects of nitrogen dopants in MXenes. DFT calculations showed that among the three sites in MXene, nitrogen (N) dopants replaced –OH terminations. It has been found that electrical double-layer and pseudo-capacitance are significantly enhanced as a result of these aforementioned replacements. Additionally, they altered the spacing and surface absorptions as an electric double-layer capacitor (EDLC). By annealing in an ammonia environment, N-doped $Ti_3C_2T_x$ electrodes were reported by Wen *et al.*[189] in 2017. N-doped $Ti_3C_2T_x$ showed magnetic characteristics, and hence had a greater ability to enhance MXene properties for better performances.[190] In order to enhance nitrogen dopants, a two-step pre-intercalation annealing technique has been reported along with addition of ammonium citrate (AC) as an intercalant and antioxidant addition. Subsequently, a precursor material has been subjected to annealing in an ammonia atmosphere.[191] The heat treatment expands the interlayer space by incorporating nitrogen atoms into the lattice of the MXene, and additionally reduces the concentration of fluorine terminations. This treatment enhanced electrochemical capacitances with values of 192 F g^{-1} (1 M H_2SO_4 electrolyte) and 82 F g^{-1} (1 M $MgSO_4$ electrolyte).[146] Fig. 10e demonstrates that the cyclic voltammetry (CV) profiles obtained in the presence of 1 M H_2SO_4 did not exhibit the perfect rectangular geometry of pure EDLC on carbon electrodes. Moreover, in the case of MXene as well as N-doped MXenes using H_2SO_4 electrolyte, capacitance "humps" within a potential range of −0.2 V to −0.1 V relative to an Ag/AgCl reference electrode were noted.[192] Surprisingly, at high voltage, N–$Ti_3C_2T_x$ exhibited robust capacitance (128 F g^{-1}) measured at a scan rate of 200 mV s^{-1}.[189]

4. Properties of MXenes and evaluation for various applications

MXenes are composed of transition-metals carbides and nitrides with variable terminations that exhibit diverse properties depending on their composition. MXene stability is associated with the number of transition-metal atoms in the unit cell. DFT calculations indicate that MXenes exhibit good stability under ambient conditions, maintaining their structure without alteration. Transition-metal carbides display superior stability as compared with their nitrides because carbon-based MXenes exhibit stronger binding energies than nitrogen-based Mxenes. The thermal stability of MXenes depends on their chemical composition and terminations. Exposed atoms on the MXene surface are often thermodynamically unstable and susceptible to oxidation in air. For example, the Ti_2C (MXene) surface interacts with O_2 to form TiO_2, which makes it unstable in the presence of oxygen. However, their thermal stability varies based on composition, environment, and surface atoms. MXenes inherently exhibit excellent electrical conductivity due to the layered arrangement of metal atoms. Titanium-based MXenes show electrical conductivity, whereas molybdenum-based MXenes exhibit semiconducting properties. Surface terminations, defects, and lamellar scale significantly affect their conductivity. The exceptional thermal conductivity of MXenes contributes to efficient heat dissipation in electronic devices, enhancing their reliability. In terms of mechanical strength, MXenes are better than graphene in terms of elasticity and flexural strength along their plane. The nature of terminal groups and metal atoms influences their mechanical robustness. Oxygen-terminated MXenes generally exhibit higher mechanical strength than other functionalization types. MXenes, being hydrophilic, maintain a stable dispersion due to charged surfaces in water. They possess some transparency (97% at a thickness of 1 nm) and are suitable for photoelectronic applications. MXenes without surface functional groups exhibit magnetism, but the presence of functional groups diminishes it, with certain exceptions (*e.g.*, chromium-based MXenes). These properties have led to extensive exploration of MXenes in energy storage, catalysis, electromagnetic shielding, sensing, biology, and flexible electronics. MXene properties that have led to state-of-the-art applications are illustrated in Fig. 13.

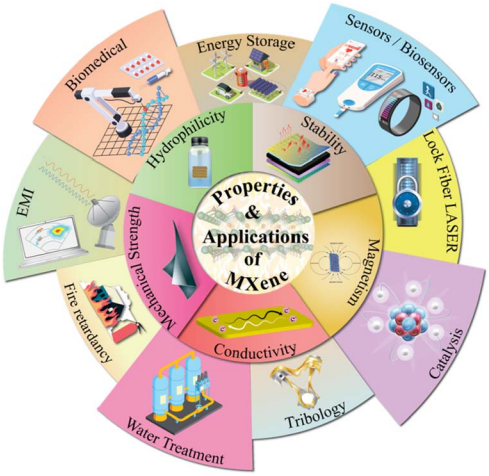

Fig. 13 MXene properties that have led to state-of-the-art applications.

MXenes are commonly synthesized by etching the A-layer from MAX with the help of an etching agent. The choice of etching agent influences inherited terminations and

subsequently impacts on the properties of MXenes for target applications. Exfoliation of MXenes is achieved by employing polar organic solvents such as dimethyl sulfoxide and isopropanol, along with multiple sonication.[193–195] Ti_3C_2 includes terminations such as –OH, =O, and –F, and annealing of MXenes in open air can lead to their oxidation.[196]

Various researchers have reported advanced applications after etching of Ti_3AlC_2 along with functional-group linkages in the presence of HF. For example, they described the detailed mechanistic insights to functional groups mostly involved in photocatalysis. When comparing the traditional HF etching method to a hydrothermal approach using $NaBF_4$, both methods were found to generate termination of –OH groups. However, the elemental distribution of Ti_3C_2 synthesized through the hydrothermal method revealed much better performances in energy-storage applications such as supercapacitors.[66,197]

Peng *et al.* explored the potential of –OH termination to enhance quick charge transfer in photocatalytic degradations of organic pollutants.[198] Another investigation revealed a significant impact specifically due to –OH terminations to achieve a low work function (1.6 eV) of MXenes.[199] Another study predicted that in the presence of –OH functional groups, Li-ion storage could not hold enough capacitance (which is contrary to =O terminations). It has been noted that annealing of MXenes can favour conversion of –OH functional groups which results in an increase in capacitance for various electronic applications.[166] In a similar manner, annealing of MXenes in a hydrogen environment can be utilized to remove –F groups for charge-storage applications. Annealing of MXenes has proven beneficial for ion transport, so exposure of active sites is increased to involve catalytic reactions.[200] Some reports have suggested that hydrophilic terminations (*e.g.*, =O and –OH) enable $BiPiO_4/Ti_3C_2$-type semiconductors to serve as additional agents for remediation of pollutants from wastewater.[201] In another study, Ti_3C_2 quantum dots were developed by employing TiO_2/g-C_3N_4 for photocatalytic CO_2 reduction.[202] The heterojunction ability of MXenes to bond with terminations provides well-tolerated dispersion onto g-C_3N_4, so these quantum dots could serve as charge-transfer tracks.[203]

Similarly, due to inherently negative Fermi levels, Ti_3C_2 can deliver efficient photocatalytic H_2 generation in the form of g-C_3N_4/Ti_3C_2 hybrid catalysts.[204,205] Higher hydrogen activities are due to separation of charges through electron transfer from g-C_3N_4 to Ti_3C_2, which is facilitated by more conducting sites for charge transfer.[206] Consequently, if this Ti_3C_2 material is combined with Ag_3PO_4, it aids photodegradation reactions.[207] Zhang *et al.* demonstrated the significance of =O and –OH on MXenes that carry negative charges for catalytic reactions.[208] Another study discovered that functional groups present in Ti_3C_2 may serve as "electron traps" owing to their metal-like characteristics, which serve as co-catalysts.[209] Functional groups can control the morphology and surface of layers during the synthesis of composite materials.[210] The incorporation of organic/MXene composites has been shown to enhance the electrochemical performance of energy-storage devices.[211,212] These composites offer two key advantages. First, the high conductivity of the MXene promotes improved conductivity of organic materials, thereby enhancing material utilization.[213] Second, the presence of surface multi-functional groups and large layer spacing facilitates electrolyte adsorption for ion transport.[214]

Ti_3C_2 with terminal groups is extremely effective for many applications, but few reports have focused on terminations.[215,216] Study on terminations requires more attention with regard to the optimized ratio of different terminations that can enhance the characteristics and stability of Ti_3C_2.[216] Table 2 summarizes the various etching methods reported for MXene synthesis, terminations and specific applications linked to synthetic methods. Additionally, Table 2 highlights the advantages and disadvantages of reported methods for specific applications.

Table 2 Summary of etching methods, related terminations, advantages, disadvantages and applications of MXene synthetic strategies

Etching methods	Terminations	Advantages	Disadvantages	Applications	Ref.
HF etching	–F, –OH	Tunable bandgap, good conductivity and ductility	Highly corrosive, toxic and eco-unfriendly	Polymer composite fillers, LIBs, pseudo capacitors	80
In situ HF etching	–Cl	Single termination	Requires high temperature	LIBs	217
Alkali based etching	–OH, =O	Non-toxic, corrosive resistance, excellent electrical conductivity	Low efficiency, requires high temperature	Catalyst support in electrochemical system	218
Molten salt etching	=O, –Cl	Exfoliated from multi- to few-layer MXene	Aforementioned	LIBs	219
Molten salt etching followed by KOH washing	–F, –OH	Safe, hydrophilicity	Aforementioned	Energy storage	220
Electrochemical assisted etching	–OH, =O	Non-toxic, fluorine free	Low efficiency	Super capacitors	57
Algae extraction etching	N/A	Cost effective, environment friendly, high yielding	Aforementioned	Photothermal agents	58
Hydrothermal method	–OH	More efficient than HF etching, environmental benign	Need expensive autoclave	Improved adsorption properties	221
In situ etching	–OH, =O	Improved rate performance	Aforementioned	High performance asymmetric super capacitors	222
Gas phase	–Cl	Aforementioned	Aforementioned	Energy storage	82

In recent years, MXenes has been found to be suitable choices for a wide range of applications due to their distinct and desired properties: excellent electronic conductivity, chemical stability, ion intercalation, and morphology.[223] MXenes have been utilized in biomedicine, energy storage, sensors, catalysis, electromagnetic-interference shielding, tribology, water treatments, fire retardancy, and lock fibre laser technologies.

4.1. Biomedical applications of MXenes

Recent research has shown that MXenes and their composites have enormous potential in the healthcare sector. MXenes are used in sensors, bone regeneration, bioimaging, antibacterial treatment, photothermal therapy, drug-delivery systems, and tissue engineering.[224–228] This is due to their unique 2D structure and excellent properties, such as mechanical flexibility, hydrophilicity, light-to-heat conversion, and biocompatibility.[229] Utilizing the significant surface area of SP-modified Ti_3C_2 nanosheets (Ti_3C_2-SP), the anticancer drug doxorubicin (Dox) can be effectively loaded onto the surface of MXenes[230,231] (Fig. 14a). Upon endogenous or external triggering, loaded anticancer medicines can be released from MXene nanosheets for chemotherapy. The small planar nano-sizes of these Ti_3C_2-SP nanosheets allow them to easily circulate within the blood vessels that passively accumulate in tumour tissues,[232] thereby leveraging the permeability-and-retention effect[233] (Fig. 14b). A schematic of a nanoplatform, chemotherapy, photodynamic therapy, and photothermal therapy of tumours[234] on Ti_3C_2 is illustrated in Fig. 14c. *In vivo* computed tomography (CT) was done by injecting 4T1 intravenously in tumour-bearing mice with TaC_3-SP (20 mg kg^{-1}).[232] Surprisingly, after administering

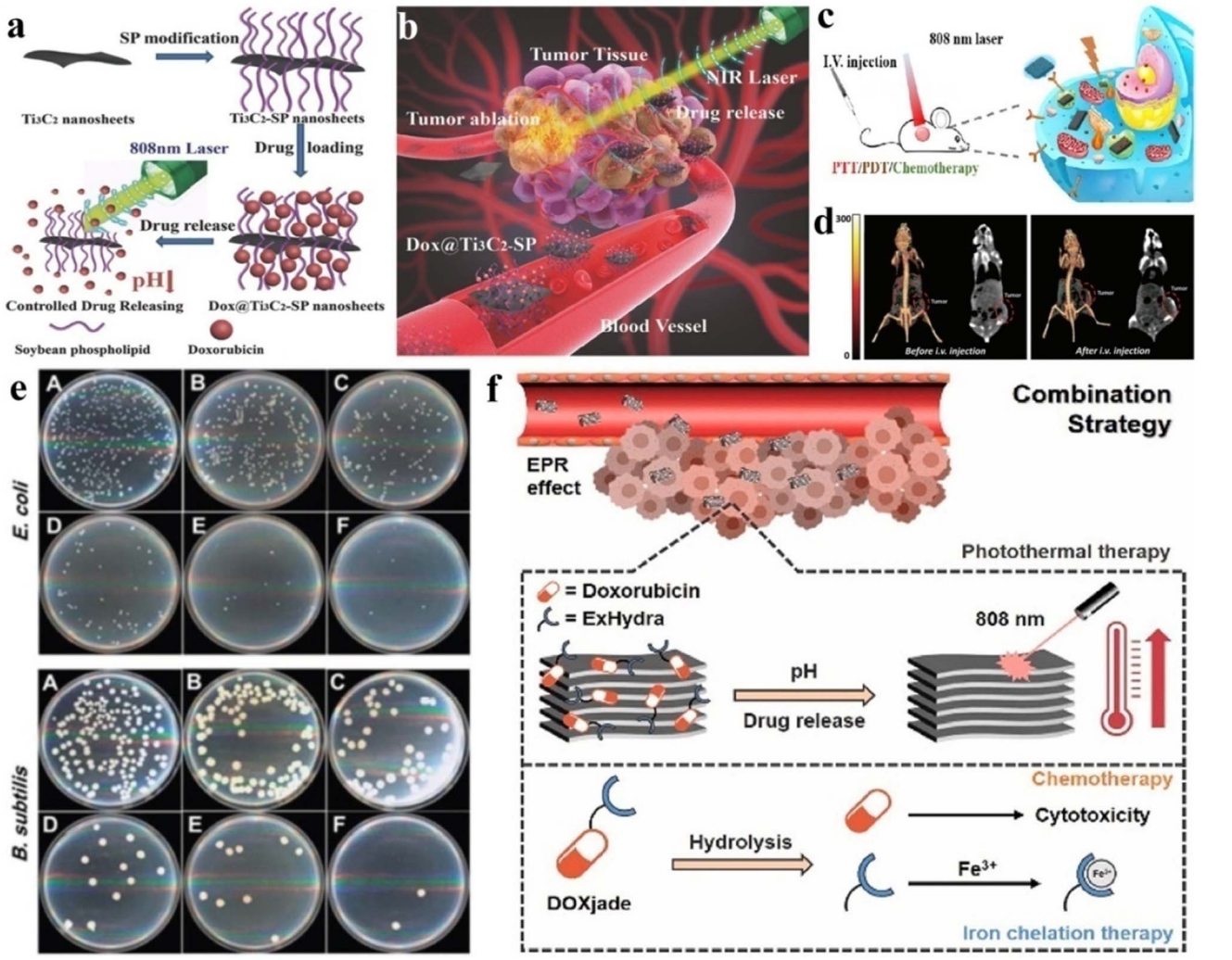

Fig. 14 (a) MXene modification for drug loading and control release. (b) Use of Ti_3C_2 for drug delivery *in vivo* for photothermal and chemotherapy of cancer, reproduced from ref. 231 with permission from Wiley, copyright 2018. (c) Photothermal, photodynamic, and chemotherapy of tumours, reproduced from ref. 234 with permission from American Chemical Society, copyright 2017. (d) Evaluation of CT results for controlled tests on mice (receiving an intravenous drug at 10 mg mL^{-1}) for 24 h, reproduced from ref. 129 with permission from Wiley, copyright 2018. (e) Images of agar plates displaying re-cultivated *Escherichia coli* and *Bacillus subtilis* after treatment with various doses of $Ti_3C_2T_x$ for 4 h, reproduced from ref. 125 with permission from American Chemical Society, copyright 2016. (f) Iron chelation-based chemo-photothermal treatments, reproduced from ref. 236 with permission from Elsevier, copyright 2022.

Ta_4C_3-SP intravenously, CT taken 24 h later showed a clear image that was only possible due to application of a MXene (Fig. 14d).[129]

$Ti_3C_2T_x$ also exhibits antibacterial properties, as shown by re-cultivating *Escherichia coli* and *Bacillus subtilis* cells on agar plates after 4 h of exposure to a MXene (Fig. 14e). These images provide evidence of the antibacterial properties exhibited by $Ti_3C_2T_x$ in aqueous suspensions.[235] Fig. 14f displays DOXjade loading onto 2D ultrathin MXene nanosheets, which enables iron chelation through chemo-photothermal treatments.[236]

4.1.1 Drawbacks. From a medical viewpoint, the drawback associated with MXene-based materials is their poor dispersibility in water. This can cause obstruction of cell transit along with blood circulation.[39] In addition, MXene-based materials may accumulate in the reticuloendothelial system (RES) upon intravenous injection, which can lead to toxicity.

4.1.2 Suggestions/precautions. Defects can be resolved by altering the MXene and its surface terminations.[237] It is necessary to design MXene-based compounds that are biocompatible and biologically non-toxic for medical applications.[77]

4.2. Energy-storage applications of MXenes

In recent decades, the world has been facing energy crises due to rising energy use and continuous decline of fossil-fuel resources.[238] Hence, there is a great demand to replace these diminishing sources of energy by developing alternatives that must be clean and sustainable.[239] The most common renewable energy source would be solar energy, which could be harvested by use of advances materials such as MXenes or their derivatives. Such solar-based technology would need energy conversion and appropriate storage, such as batteries and

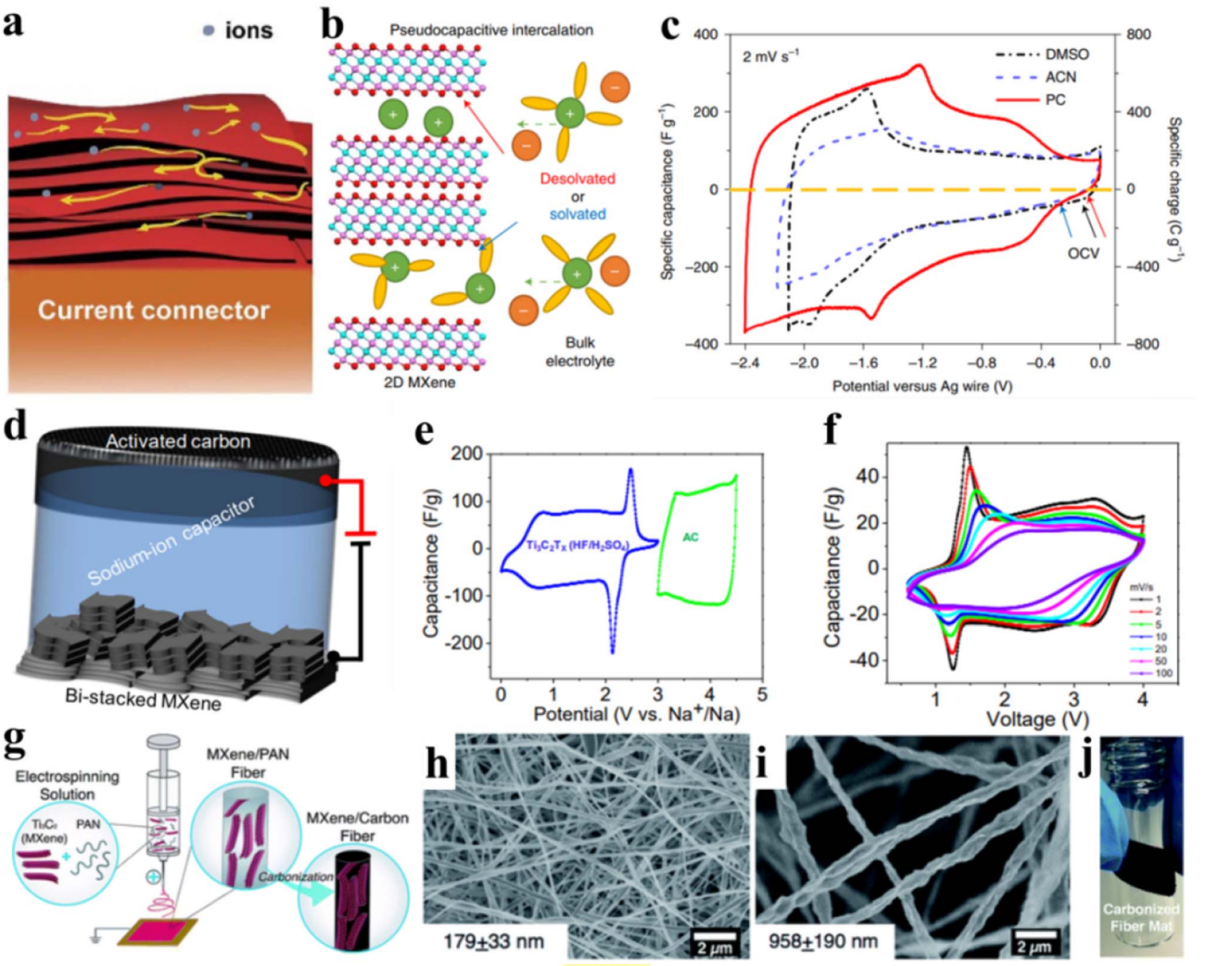

Fig. 15 (a) Ion-transport channel of MXene films, reproduced from ref. 245 (b) Supercapacitor for electrolytes and MXenes (schematic). (c) CV results, reproduced from ref. 245 with permission from *Nature Energy*, copyright 2019. (d) High-rate energy storage using bi-stacked titanium carbide. (e) CVs of bi-stacked MXene and AC electrodes. (f) CVs of a hybrid Na-ion capacitor at various scan rates, reproduced from ref. 247 with permission from American Chemical Society, copyright 2018. (g) Scheme employed for the synthesis of MXene/carbon nanofibers. (h) SEM images of PAN fibers. (i) PAN fiber developed with a MXene (16 wt%). (j) Digital image of carbonized PAN fibers, reproduced from ref. 249 with permission from Royal Society of Chemistry, copyright 2019.

Table 3 Comparative summary of reported supercapacitor applications of MXene-based materials along with specific capacitance [F g^{-1}], energy density [W h kg^{-1}], power density [W kg^{-1}] and % capacitance retention

Derived material	Precursors	Specific capacitance [F g^{-1}]	Energy density [W h kg^{-1}]	Power density [W kg^{-1}]	Capacitance retention [%]	Life cycle [cycles]	Ref.
Ti_2CT_x/polyaniline	MXene + PANI	635	42.3	950	94.25	10 000	251
MXene/CAC film	MXene films	344.9	8.3	36.1	93.5	30 000	139
TCBOC//TCBOC SSC	$Ti_3C_2T_x$–MXene	247.8	15.2	567.4	85	5000	252
$Ti_3C_2T_x/MnO_2$	MnO_2/Ti_3C_2	611.5	n.a	n.a	96	1000	253
Polyaniline–graphene hybrid hydrogel	MXene + GO + Zn particles	137.5	30.3	1130	81	10 000	254
$NiCo_2$-LDHs@MXene/rGO//MXene/rGO	MXene and NiCo–LDHs	240	65.3	700	92.8	10.000	255
VS_2/MXene	Vanadium disulfide + MXene	115.7	41.13	793.50	85	5000	256
MoS_2-$Ti_3C_2T_x$	$(NH_4)_2MoS_4$ + CH_4N_2S + MXene	115.2	5.1	298	72.3	10 000	257
$NiCo_2S_4$/MXene	$NiCo_2S_4$ & MXene	621	72.82	635	95.21	10 000	258
$Ti_3C_2T_x/CoS_2$	CoS_2 & MXene	1320	28.8	800	78.4	3000	259

supercapacitors.[240] Supercapacitors can be built to provide high power density, which is ideal for automobile and industrial applications. MXene-based batteries offer high energy density, which is advantageous for portable devices.[223,241] In this context, MXene-based supercapacitors have attained significant attention as new and advanced systems. Compared with batteries, supercapacitors exhibit higher power density, charge–discharge rates, and cycle stability.[223] Jiang *et al.*[242] developed 2D MXene (titanium carbide) nanosheets for processing to develop electrochemical applications. MXene-based wafer-scale supercapacitors (MSCs) can proficiently remove a pulsed DC voltage. Besides MXenes, all-solid-state supercapacitors (SCs) utilizing polyvinyl alcohol (PVA)/KOH gel electrolyte demonstrated a density of 63 mW h cm^{-3} at a power density of 0.06 W cm^{-3}, and MXene-based supercapacitors underwent 10 000 charge/discharge cycles at a current density of 5 A g^{-1}. Their capacitance remained unchanged, indicating the sustained and stable performance of energy conversion and storage devices (ECSDs).[243] Moreover, MXenes with a large surface area make good capacitors because they have double electrical layers. Fig. 15a shows a schematic representation of an in-plane ion-transport channel of MXene films. These measurements allow monitoring of the changes in the interlayer space, as illustrated in Fig. 15b for Ti_3C_2 electrodes as they are involved in cycling. In Fig. 15c, a comparison is presented of CV results obtained at a scan rate of 2 mV s^{-1} for macroporous Ti_3C_2 electrodes.[244] These electrodes were tested in three 1 M LiTFSI organic electrolytes containing different solvents: DMSO, ACN, or PC. CV results demonstrated that the PC-based electrolyte had a higher coulombic efficiency (96%) with a wider negative voltage window of 2.4 V.[245] DMSO and ACN showed a negative voltage window of 2.1 V and 2.2 V, respectively.[245]

Fig. 15d represents a schematic diagram of Bi-stacked MXene supercapacitors and CVs of bi-stacked MXenes. AC electrodes and hybrid Na-ion capacitors in the CV curves are exhibited in Fig. 15e.[246] These curves exhibit sharp redox peaks. Contrarily, CV curves for the AC electrode were rectangular. Combination of a pseudo-capacitive MXene electrode demonstrated a mixed behavior for battery and capacitor that was perhaps due to multiple layers in the MXene.[247] This device could be categorized as a "hybrid" capacitor due to its unique composition.[248] As shown in Fig. 15f, the lower cutoff voltage was set at 0.6 V, whereas the upper voltage limit was set at 4 V. A schematic representation of the electrospinning process for MXene/carbon nanofibers is illustrated in Fig. 15g.[249] Delaminated MXene flakes were dispersed in dimethylformamide (DMF) before being combined with polyacrylonitrile (PAN) to produce MXene/PAN solutions.[250] SEM results of electrospun MXene/PAN fibers are illustrated in Fig. 15h for pure PAN fibers and Fig. 15i for a MXene (10 wt%). Fig. 15j shows a fiber mat carbonized at 700 °C for 1 h using 10 wt% of $Ti_3C_2T_x$ (MXene) and 8 wt% of PAN fibers.[250]

4.2.1 Drawbacks. Some MXene-based electrode materials lack mechanical stability, especially if used in bendable devices. MXenes are sensitive to environmental factors such as moisture and oxygen. MXenes can undergo structural modifications that lead to reduced performance for energy-storage devices.

4.2.2 Suggestions and precautions. For applications of MXenes in energy conversion or storage applications, MXenes must be sufficiently stable and moisture-free.[77] To achieve optimal performance in MXene-based devices, collaborative efforts between skilled engineers and experienced professionals can be helpful.[79]

Table 3 summarizes the features of MXene-based materials used in supercapacitor applications, including specific capacitance [F g^{-1}], energy density [W h kg^{-1}], power density [W kg^{-1}], and % capacitance retention.

4.3. Use of MXene as sensors and biosensors

In the context of sensing applications, certain characteristics are required in sensing materials: sensitivity; optimized limit of detection; excellent conductivity; ability to customize required surface properties; selectivity towards specific analytes.[260,261] These characteristics have been attained by MXenes and their composites for use in electrochemical biosensors. MXene-based

materials possess exceptional transducing properties that make them highly suitable for a diverse range of sensors, such as bio-electrochemical, electrochemical, gas, strain, chem-iluminescence, pressure, and photochemical sensors. Additionally, they exhibit stable mechanical characteristics and outstanding surface attributes.[262] Fig. 16a shows a chip that was specifically designed for complete blood analyses. The chip consists of four layers. The uppermost layer contains a dedicated blood-flow channel, whereas the second layer is a dialysis membrane.[263] This MXene-based chip enables the passage of molecules such as urea and uric acid (UA) that are smaller than 1000 Da.[250] The third layer holds a sensing chamber that controls the flow channels for isotonic solutions. The channel within this chip allows for the dialysis of blood analytes, which then accumulate within the detection chamber. In the latter, a sensing electrode (located on the bottom layer) detects analytes and generates the corresponding signals.[264] Fig. 16b illustrates the electrocatalytic process of UA on the MXene-modified sensor. To enhance the UA concentration at the electrode/electrolyte interface for subsequent electrocatalysis,

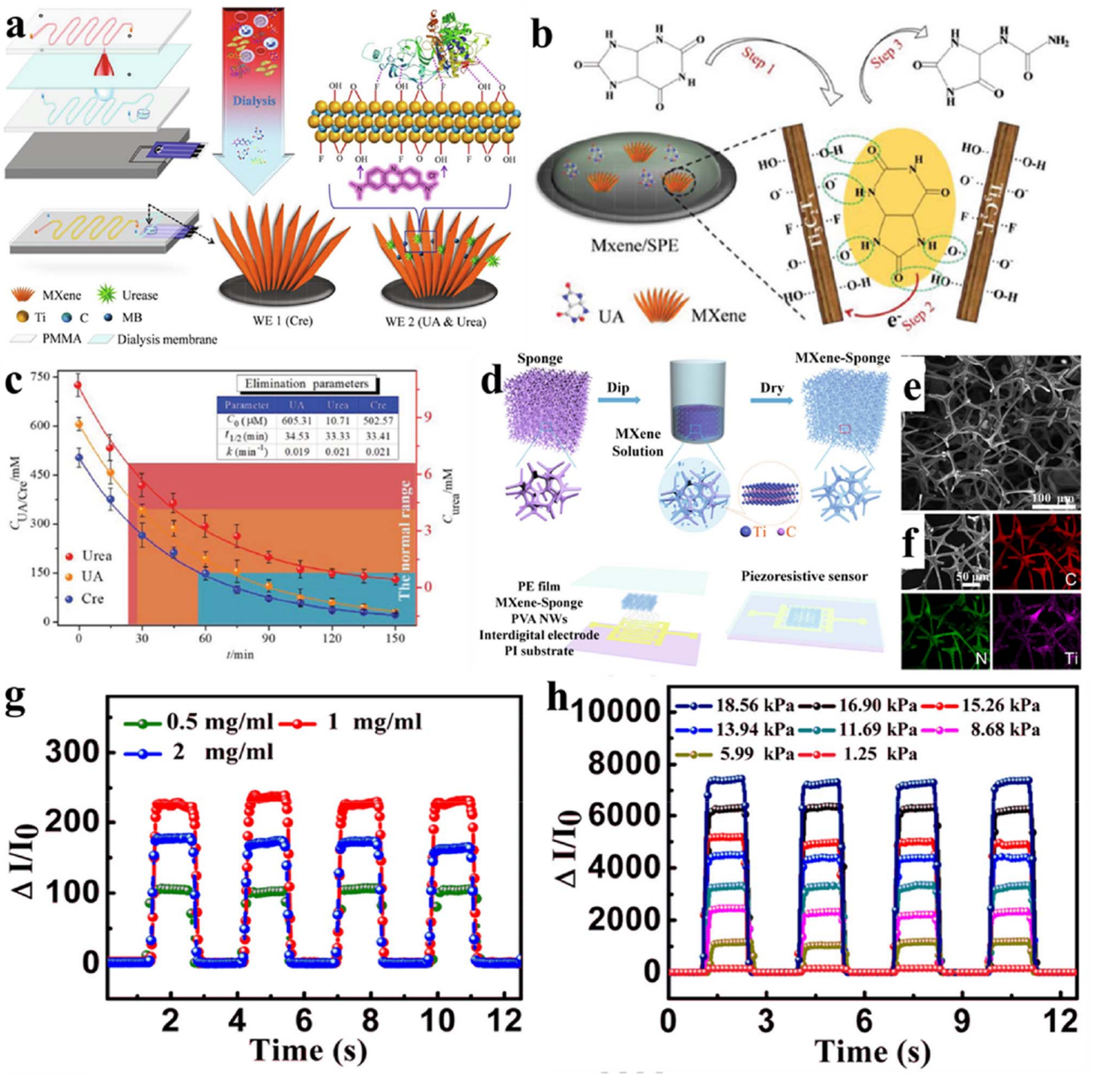

Fig. 16 (a) Fabrication of a micro-fluidic chip with a MXene. (b) Scheme used for determination of uric acid on MXene/SPE. (c) Comparative curves for uric acid, urea, and creatinine in blood, reproduced from ref. 263 with permission from Wiley, copyright 2018. (d) Fabrication of a MXene-sponge. (e) SEM image of a MXene-sponge. (f) Elemental mapping of a MXene-sponge. (g) *I*–*T* curves of MXene-sponge sensors. (h) *I*–*T* curves of an MSP device. Reproduced from ref. 266 with permission from Elsevier, copyright 2018.

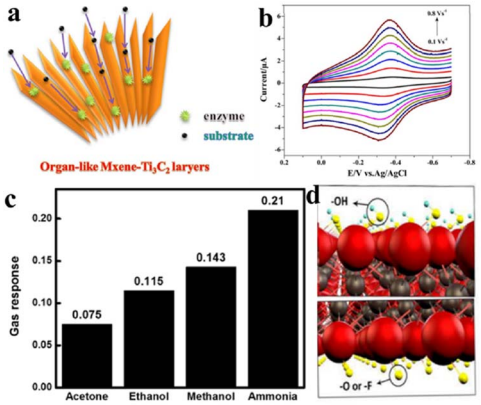

Fig. 17 (a) Encapsulation of haemoglobin in an organ-like MXene. (b) CV results of a Nafion/Hb/Ti_3C_2/GC electrode, reproduced from ref. 267 with permission from IOP Science, copyright 2015. (c) Different terminations on MXene nanosheets. (d) Average sensing response for various gases, reproduced from ref. 269 with permission from American Chemical Society, copyright 2017.

UA molecules initially adsorb by forming hydrogen bonds with the functional groups (OH, O, and F) of MXene. Fig. 16c illustrates the concentration–time curves of UA, urea, and creatinine in blood during haemodialysis. The terms C_0, $t_{1/2}$, and k denote the concentration before dialysis, half-life of elimination, and the rate constant for elimination, respectively.[264]

Fig. 16d represents the MXene-sponge synthetic process specifically designed for sensing applications. SEM results for the MXene-sponge and pictures of the elemental mapping for C, N, and Ti of the MXene-sponge are represented in Fig. 16e and f. Fig. 16g depicts the current–time curve of the MXene-sponge with different initial concentrations (0.5, 1, and 2 mg mL^{-1}) under the same pressure conditions. Notably, when the initial concentration of the MXene solution is 1 mg mL^{-1}, the MXene-based sensor exhibits the highest on/off current ratios.[265,266] The current variations of the MPI-based sensor under different pressures can be seen in Fig. 16h. The current increases steadily as the pressure rises. Fig. 17a and b illustrate organ-like MXene-Ti_3C_2 nanomaterials encapsulating haemoglobin and cyclic voltammograms of the Nafion/Hb/Ti_3C_2/GC electrode, respectively.[267,268]

Fig. 17c displays the average response of $Ti_3C_2T_x$ towards the sensing of various gases, including ammonia, methanol, ethanol, and acetone. The respective response values for these gases are 0.210, 0.143, 0.115, and 0.075.[269] The $Ti_3C_2T_x$ sensor can be utilized for multiple sensing applications, such as sensing VOC gases, toxic organic gases, greenhouse gases (*i.e.* CO_2, N_2O), and dangerous exploratory gases (H_2, CH_4, C_2H_4, NH_3) with a high response. Moreover, MXene-based sensors are widely utilized in chemical industries, food industries, electronic industries, pharmaceuticals, biomedical, and rocket or space science. In Fig. 17d, a schematic representation of a 2D $Ti_3C_2T_x$ structure is presented that illustrates its surface

Table 4 Summary of solution-based electrochemical-sensing performance of MXene-derived materials, including the analyte detected, sensing technique, linear range, and sensitivity

MXene derived sensing materials	Analyte detected	Sensing technique	Linear range	LOD	Sensitivity	Ref.
GO_x-Au-MXene-naf/GCE	Glucose	Amperometry	0.1–18 μM	5.9 μM	4.2 μA mM^{-1} cm^{-2}	273
Tyr-MXene-chi/GCE	Phenol	Amperometry	0.05–15.5 μM	12 nM	414.4 mA M^{-1}	30
Hb-naf-MXene/GCE	NO_2^{-1}	Amperometry	0.5 μM–11.8 mM	0.12 μM	n.a.	274
MXene-PtNP/GCE	H_2O_2	Amperometry	490 μM–53.6 mM	448 nM	n.a.	275
MXene/GCE	BrO_3^-	Differential pulse voltammetry	50 nM–5 μM	41 nM	n.a.	276
MXene–FET	DA	Field effect transistor	100×10^{-9}–50×10^{-6} M	100×10^{-9} M	n.a.	277
$Ti_3C_2T_x$/GCE	H_2S	Cyclic voltammetry	100 nM–300 μM	16.0 nM	0.587 μA μM^{-1} cm^{-2}	278
Nafion/Hb/Ti_3C_2/GCE	H_2O_2	Cyclic voltammetry	0.1–260 μM	20 nM	n.a	118
Ti_3C_2/GOD	Glucose	Amperometry	39.8 μM–1.319 mM	1.96 μM	98.1 μA mM L^{-1} cm^{-2}	279
Chit/ChO_x/$Ti_3C_2T_x$/GCE	Cholesterol	Differential pulse voltammetry	0.3–4.5 nM	0.11 nM	132.66 μA mM^{-1} cm^{-2}	280

Table 5 Gas-sensing performances of various MXene-based materials

MXene derived sensing materials	Target species	Conc.	Optimal temperature (°C)	Response	T_{Res} (sec)	T_{Recov} (sec)	Ref.
$W_{18}O_{49}$ $Ti_3C_2T_x$	Acetone	0.17 ppm	300	11.6	5.6	6	281
MoO_3/WO_3	Acetone	0.5 ppm	320	10	8	7	282
V_2CT_x	Methane	10 000 ppm	RT	142	38	47	283
V_2CT_x	NH_3	500 ppm	RT	3.41	41	109	284
Mo_2CT_x	CO_2	50 ppm	30	1.14	30	45	285

functional groups or terminations. The structure comprises three titanium layers "sandwiched" between two carbon layers.[269]

4.3.1 Advantages and drawbacks. MXene-based sensors possess high sensitivity and large surface area that allow for effective detection of biomolecules. These sensors exhibit a rapid response and can detect analytes even in trace amounts.[78,270] However, drawbacks include limited stability in aqueous solutions, susceptibility to oxidation, complexity, and cost of synthesis. The limited stability in aqueous solutions (especially at extreme pH) affects the long-term performance of sensors.

4.3.2 Percussions and suggestions. Careful surface modification is important for functionalization and surface stability.[270,271] Thus, ongoing research must focus on understanding MXene–bimolecular interactions for their further sensing applications.[272]

Table 4 is a comparison of the solution-based electrochemical-sensing performances of MXene-derived materials, including analyte detected, sensing technique, linear range, and sensitivity. Table 5 reveals the gas-sensing performances of various recent MXene-based materials.

4.4. Applications of MXenes in catalysis

Attention in electrochemical and photocatalytic water splitting, organic pollutants, and CO_2/CO reduction has been sparked by the need to develop effective and sustainable technologies.[2,286,287] High-performance catalysts play a vital part in the effective use of these technologies.[45,50,288–290] Pt, Pd, Au, Ag, Cu, TiO_2, CdS, RuO and IrO are the main components of conventional catalysis. However, these materials have a number of drawbacks, including high cost and limited supply.[291] On the other hand, MXene-based catalysts have been employed in electrochemical and photochemical catalysis because of superior electronic conductivity and outstanding hydrophilicity.[292] Moreover, MXene-derived catalysts demonstrate outstanding performances as co-catalysts that have excessive potential to replace expensive metals.[223] In order to prepare MXenes having electron transport layers (ETLs) for targeted applications, a spin-coating technique has been recommended with a $Ti_3C_2T_x$ colloidal dispersion (1 mg mL^{-1}) onto ITO.[293] Subsequently, such materials undergo different durations of UV-ozone treatments (0, 10, 30, or 60 min) (Fig. 18a). Devices with an architecture of ITO/ETL/$CH_3NH_3PbI_3$/spiro-OMeTAD/Ag were developed to compare the performance of $Ti_3C_2T_x$ as an ETL in perovskite solar cells (involved in catalysis reactions) before and after UV-ozone treatments (Fig. 18b).[294]

A typical cross-sectional SEM image of a planar PSC device fabricated using a $Ti_3C_2T_x$ thin layer as ETL is shown in Fig. 18c. The SEM image demonstrates the six layers of the material (glass, ITO, ETL, $CH_3NH_3PbI_3$, spiro-OMeTAD and Ag), which is extremely useful for photocatalytic reactions. Fig. 18d illustrates the computed integrated currents and external quantum efficiency (EQE) spectra for ETLs with varying UV-ozone treatment durations that correlate with performances in catalytic reactions. Finally, Fig. 18e is a schematic representation of a flexible

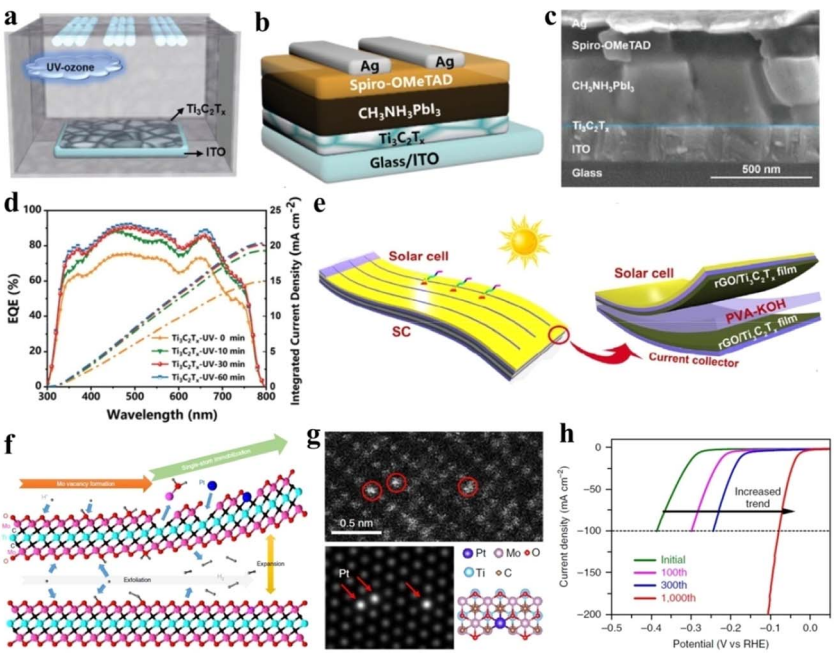

Fig. 18 (a) UV-ozone treatments on a $Ti_3C_2T_x$ film *via* spin-coating. (b) Device architecture of ITO/ETL/$CH_3NH_3PbI_3$/spiro-O MeTAD/Ag on MXene. (c) SEM image of a planar perovskite solar cell (PSC). (d) Percent EQE spectra (external quantum efficiency) along with integrated current densities, reproduced from ref. 293 with permission from Wiley, copyright 2019. (e) Energy conversion and storage device (schematic), reproduced from ref. 243 with permission from Royal Society of Chemistry, copyright 2017. (f) Mechanism for the HER on $Mo_2TiC_2O_2$-PtSA. (g) HAADF-STEM of $Mo_2TiC_2T_x$-PtSA. (h) HER polarization curves of $Mo_2TiC_2T_x$ with a Pt foil as the counter electrode, reproduced from ref. 295 with permission from *Nature*, copyright 2018.

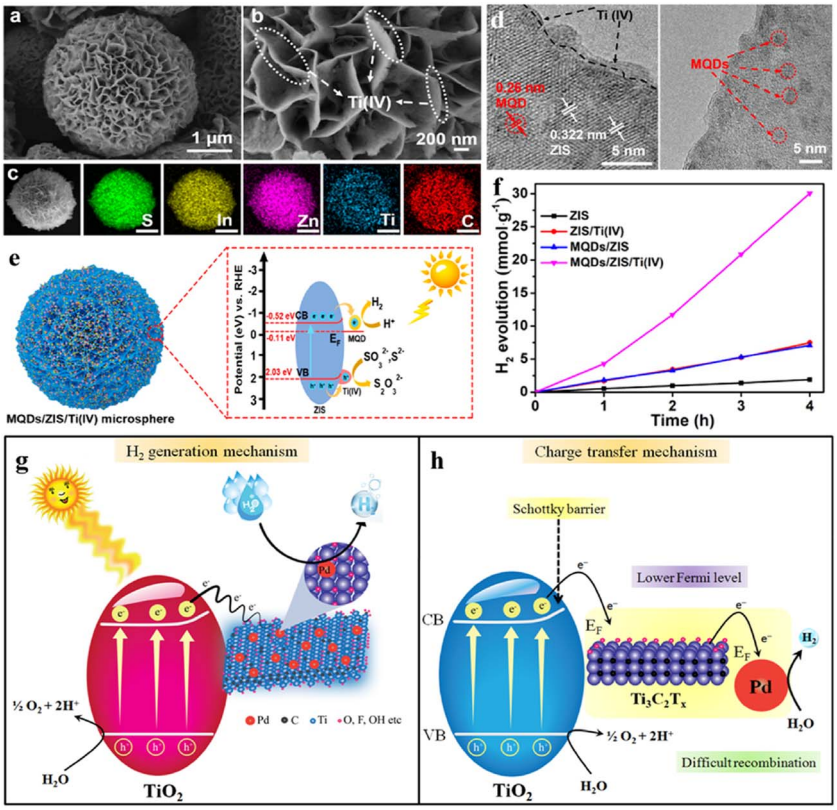

Fig. 19 (a and b) SEM images of a MXene QD-supported ZIS/Ti(IV) composite. (c) Elemental mapping of S, In, Zn, Ti, and C. (d) HRTEM of MQDs/ZIS/Ti(IV). (e) Mechanism for photocatalytic H_2 evolution on MQDs/ZIS/Ti(IV). (f) Comparison of photocatalytic H_2 evolution on ZIS, ZIS/Ti(V), MQDs/ZIS, and MQDs/ZIS/Ti(IV), reproduced from ref. 297 with permission from MDPI, copyright 2021. (g) Hydrogen-generation mechanism and (h) charge-transfer mechanism on Pd@$Ti_3C_2T_x$-TiO_2, reproduced from ref. 144 with permission from Royal Society of Chemistry, copyright 2024.

integrated ECSD employed in catalysis. Fig. 18f illustrates the electrochemical process that facilitates hydrogen cations for reductions on the MXene surface.[295] In Fig. 18g, it can be observed that Pt atoms are fixed at the Mo sites on $Mo_2TiC_2T_x$. This indicates that the Pt atoms are immobilized or anchored specifically to the Mo positions within $Mo_2TiC_2T_x$ structures. The catalytic performance of the hydrogen-evolution reaction (HER) was evaluated using different cycles, with Pt serving as the counter electrode.[296] The results of these evaluations are depicted in Fig. 18h, illustrating the HER catalytic performance. Other than energy-conversion applications, there are many other important applications of MXenes in catalysis, such as the HER, oxygen-evolution reaction (OER), carbon dioxide reduction reactions (CRR), nitrogen reduction reactions (NRR), organic pollutant degradation reactions (OPDR), biological catalytic reactions, Li-ion batteries, supercapacitors, and chemical/biosensing applications. Some reports have demonstrated that the microsphere structure of MQDs/ZIS/Ti(IV) resembles that of flowers, and that it can be synthesized by utilizing MXene quantum dots as co-catalysts. Fig. 19a and b demonstrate the SEM images of MQDs/ZIS/Ti(IV) microspheres. In Fig. 19c, elemental mappings reveal the uniform distribution of elements S, In, Zn, Ti, and C of MQDs/ZIS/Ti(IV) microspheres. Fig. 19d illustrates the presence of Ti(IV) nanoclusters at the edges of the MQDs/ZIS/Ti(IV). The lattice fringe interplanar spacing of 0.322 nm corresponds to the (102) plane of hexagonal ZIS, whereas 0.26 nm corresponds to the (110) plane of MQDs.[297] Based on these findings, a potential mechanism is proposed in Fig. 19e that explains the high photocatalytic H_2-evolution activity of the novel flower-like ZIS microsphere photocatalyst. It has been revealed that, under sunlight irradiation, electrons are photoexcited from the valence band (VB) of ZIS in MQDs/ZIS/Ti(IV) to its conduction band (CB), leaving photogenerated holes in the VB of ZIS. MQDs enhance the photocatalytic production due to the formation of a Schottky barrier at the interface of ZIS and Ti(IV) that progressively suppresses the charge recombination. Fig. 19f represents photocatalytic H_2 evolution on ZIS, ZIS/Ti(IV), MQDs/ZIS, and MQDs/ZIS/Ti(IV) catalysts using sunlight irradiation.[297] The H_2-evolution results confirm that utilization of a MXene as a co-catalyst in the form of MQDs boosts photocatalytic activities. Abid *et al.* reported that Pd metal over the $Ti_3C_2T_x$ surface improved the hydrogen-production activities of TiO_2 by effectively quenching more electrons (Fig. 19g). The higher work function and lower Fermi levels of co-catalysts promote and facilitate higher hydrogen generation (Fig. 19h).[144] These results indicate that the presence of MXene QDs and Pd@$Ti_3C_2T_x$ delivers higher H_2-generation efficiencies compared with other conventional catalysts in similar conditions.[298]

Table 6 Comparative summary of H_2 evolution on reported MXene-based electrocatalysts

Catalysts	Precursors	Over potential [η_{10} mV]	Tafel slope [mV dec^{-1}]	Electrolyte	Applications	Stability	Ref.
MoS_2/Ti_3C_2-MXene@C nanohybrids	C-coated MoS_2 & C-stabilized MXene	112	82	1 M KOH	H_2 evolution and Li-storage	>18 h	305
O-terminated $Ti_3C_2T_x$	Ti_3AlC_2	190	60.7	0.5 M H_2SO_4	H_2 evolution	24 h	306
$MoS_2@Mo_2CT_x$	Mo_2AlC_2	197	113	1 M KOH	H_2 evolution	> 8	307
Pt_x Ni NWs/Ti_3C_2	Pt_xNi NWs and Ti_3C_2	18.55	13.37	0.5 M H_2SO_4	H_2 evolution	<2 h	308
$Pt/Ti_3C_2T_x$	TBA–$Ti_3C_2T_x$ & $Pt(NH_3)_4Cl_2$	55	70	0.5 M H_2SO_4	H_2 evolution	20 h	309
Mo_2CT_x:Co	β-Mo_2C:Co	180	59	1 M H_2SO_4	H_2 evolution	3 h	310
NiS_2/V_2CT_x	V-MXene flakes	179	85	1 M KOH	H_2 evolution	NA	311
$TiOF_2@Ti_3C_2T_x$	$Ti_3C_2T_x$ & TiOF	197	56.2	0.5 M H_2SO_4	H_2 evolution and humidity sensing	24 h	312
$MoS_2/Ti_3C_2T_x$	MoS_2 and $Ti_3C_2T_x$	152	70	0.5 M H_2SO_4	H_2 evolution	12 h	313

Table 7 Comparative summary of photocatalytic performances on MXene-based photocatalysts

Photocatalyst	Synthesis method	Photocatalytic application	Light source	Performance	Ref.
Ti_3C_2/g-C_3N_4	Electrostatic self-assembly approach	H_2 production	200 W Hg lamp	72.3 μmol g^{-1} h^{-1}	314
d-Ti_3C_2/TiO_2/g-C_3N_4		H_2 production	300 W Xe lamp	1.62 mmol g^{-1} h^{-1}	315
Ti_3C_2MXene/O-doped g-C_3N_4	Electrostatic self-assembly approach	H_2 production	300 W Xe lamp	25 124 μmol g^{-1} h^{-1}	316
Ti_3AlC_2 MAX co-catalyst with proton-rich C_3N_4	Ultra-sonication method	CO_2 reduction	35 W HID lamp	786 μmol g^{-1} h^{-1}	317
TiO_2/Ti_3C_2	HF-etching	CO_2 reduction	300 W stimulated solar Xe arc lamp	0.22 μmol h^{-1}	318
$CdS@Ti_3C_2@TiO_2$	Hydrothermal method	Dye degradation	Visible light ($\lambda \geq 420$ nm)	Removal of RhB, MB, SCP and phenol at 60, 88, 88 and 150 min, respectively	319
Ti_3C_2/CdS	HF-etching	H_2 production	Visible light	825 μmol g^{-1} h^{-1}	320
CHI/Ti_3C_2	HF-etching	H_2 production	Visible to near IR	52 ± 5 μmol g^{-1} h^{-1}	321
CS@g-C_3N_4/MX	Hydrothermal method	Dye degradation	250 W Xe lamp	MB ∼99% and RhB∼98.5%	322
Ti_3C_2/TiO_2 nanoflowers	HF-etching	H_2 production	300 W Xe arc lamp	783.11 μmol g^{-1} h^{-1}	323
$Pd@Ti_3C_2T_x$-TiO_2	HF-etching	H_2 production	450 W Xe lamp	35.66 mmol g^{-1} h^{-1}	144

4.4.1 Advantages and drawbacks. Due to their intrinsically hydrophilic nature, MXenes have distinct advantages of higher electrical conductivity and mechanical properties for catalytic reactions.[299] Their conductivity is higher than that of other reported materials, such as graphene or reduced carbon nitride. MXenes have more functionalized surfaces to facilitate bonding with other species that are not available in graphene.[300] Additionally, MXenes can be utilized in energy-storage devices like Li-ion batteries, pseudo-capacitors, and sensors. MXenes and their supported catalysts can be very helpful for sustainable technologies. Besides these advantages, MXenes have fundamental drawbacks: (i) agglomeration as well as poor long-term recyclability; (ii) preparation of MXenes having monolayers is complex; (iii) MXene-based catalysts can easily be oxidized in water; (iv) preparation of MXenes with few layers or targeted layers is not easy.[301,302]

4.4.2 Suggestions and precaution. MXenes and MXene-supported catalysts may be ideal in many catalytic reactions.[303] $Ti_3C_2T_x$ has been widely utilized for the HER.[304] Hydrophilic surfaces should be conducive for the charge transportation and adsorption on active sites in photocatalytic reactions. In the case of Mxenes, Gibbs free energy approaches zero infinity, which should be conducive for proton (H^+) reduction reactions.[301] Correct washing of MXenes is important for safe use in catalysis. Photocatalytic and pH-dependent reactions must be performed in special reactors or equipment. During washing, centrifugation, or any catalytic reaction, it is important to completely disperse the MXene or MXene-supported catalyst in the reaction mixture.[79]

Table 6 details evaluation of hydrogen evolution on various reported MXene-based electrocatalysts. Table 7 details various photocatalytic applications of MXene-based electrocatalysts.

4.5. Use of MXene in electromagnetic interference (EMI) shielding

EMI is generated by various electrical devices that significantly affect the device lifespan and its environment. To reduce this problem, the common approach is employment of EMI-shielding materials. MXenes and their supported materials

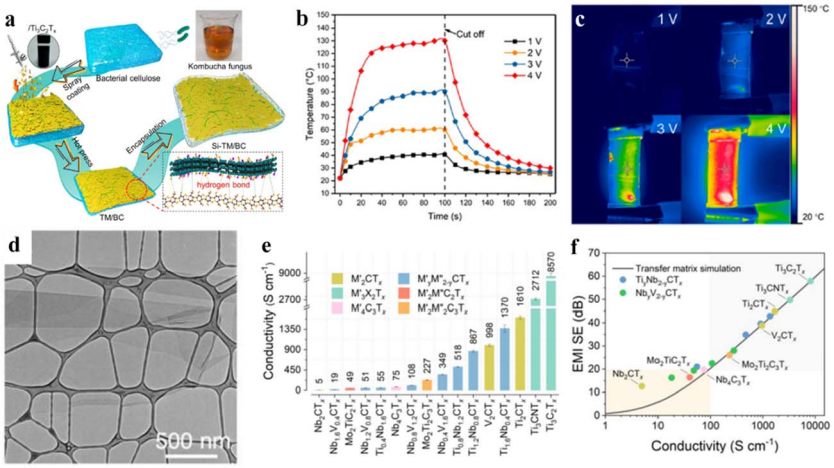

Fig. 20 (a) Fabrication scheme for TM/BC and Si-TM/BC film. (b and c) Electrothermal conversion of light into heat on Si-TM50/BC, reproduced from ref. 326 with permission from American Chemical Society, copyright 2021. (d) TEM image of targeted Ti_2CT_x. (e) Electrical conductivity of MXene films. (f) Comparison of EMI-SE values between matrix simulation and MXene films, reproduced from ref. 327 with permission from American Chemical Society, copyright 2020.

Table 8 Summary of EMI-shielding performance of MXene-based composites

MXene composite	Synthesis method	Conductivity	EMI shielding	Ref.
MXene-graphene-PVDF composite	Spray-coating process	13.68 S cm^{-1}	53.8 dB (99.99%)	328
CoPA/MXene	Simple casting method	1.4×10^{-2} S cm^{-1}	Transparency exceeds 75%	329
MXrGO@PMMA	Electrostatic assembly	0.98–3.96 W m^{-1} K^{-1}	28–61 dB	330
MXene/CNT	Vacuum-assisted filtration	1851.9 S cm^{-1}	78.9 dB	331
MXene/GNP	Electro hydrodynamic atomization (EHDA)	105 S cm^{-1}	N/A	332

can act as absorbers for incoming EMI signals and protect them from the influence of the environment (*e.g.*, moisture).[223] MXenes exhibit exceptional EMI-shielding performance due to extrinsic alterations and inherent characteristics, which include dielectric inclusions, pores, or other fabrications in MXene structures.[324] MXene $Ti_3C_2T_x$ has been incorporated into a variety of polymeric matrices, including sodium alginate (SA), polyaniline, and ultra-high molecular weight polyethylene structures. MXene-polymeric nanocomposites display increased tensile strength but exceptional conductivity.[325] Fig. 20a illustrates a schematic fabrication process for robust and flexible Si-TM/BC multifunctional MXene-based films. As EMI-shielding materials, utilization of MXenes has received remarkable attention compared with other reported 2D materials. This is due to their weak mechanical properties and instability. Fig. 20b shows the surface temperature of a Si-TM/BC film over time at stable voltages of 1 to 4 V. Temperature climbed quickly before stabilization. In accordance with Joule's law, $Q = I^2Rt$ (where Q represents the generated heat, I is the applied voltage, R is the electrical resistance, and t is the working time), the temperature resulting from Joule heating is directly proportional to the applied voltage.[326] The saturation temperature of the Si-TM/BC film at different driving voltages can be clearly observed in infrared thermal images (Fig. 20c). The TEM image of Ti_2CT_x at 500 nm is illustrated in Fig. 20d, whereas the electrical conductivity (S cm^{-1}) of various MXene films is graphically illustrated in Fig. 20e and f. Comparison of electromagnetic interference shielding effectiveness (EMI-SE) values between transfer matrix simulation and MXene films of thickness ~5 μm at a frequency of 10 GHz has been evaluated.[327] The EMI-shielding performances of various MXene-based composites is shown in Table 8.

4.5.1 Advantages and drawbacks. MXenes and their supported materials can act as absorber for incoming EMI signals and protect the environment. Mxenes, due to their high conductivity and large surface area, can absorb electromagnetic waves effectively. This is why their demands have been increased in electronic and telecommunications. However, some drawbacks may interfere in such applications: (i) MXene compounds can be oxidized in aqueous media; (ii) hydrophilic surfaces should be conducive and non-protective for EMI shielding.

4.5.2 Suggestions and precautions. MXene-supported IMI filters in electronic circuits can prevent the conducive interference from travelling back. MXene-polymeric nanocomposites display increased tensile strength that promotes exceptional conductivity for better performances and targeted applications.[333] Nevertheless, before developing the device, testing for EMI is necessary. MXene-based electronic devices must be preserved in standard or optimized conditions of temperature, pressure, and pH.[334]

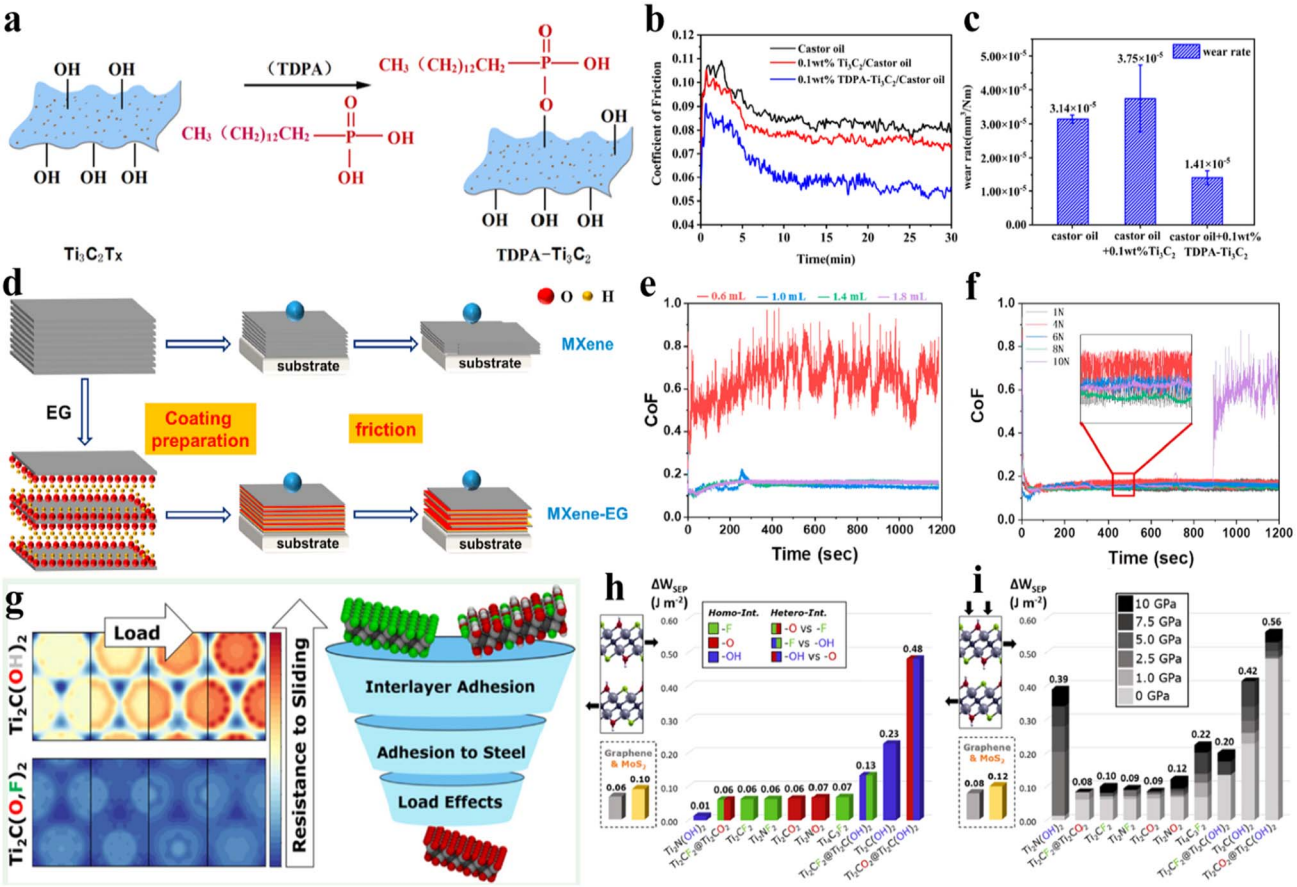

Fig. 21 (a) Representation of molecules of tetradecylphosphonic acid grafted on a MXene. (b and c) Comparative coefficients of friction and wear rates of castor oil, castor oil with 0.1 wt% Ti_3C_2, and 0.1 wt% TDPA-Ti_3C_2, reproduced from ref. 336 with permission from Elsevier, copyright 2021. (d) Friction mechanism (schematic). (e) Friction tests employed for different amounts of MXene-EG coatings. (f) Friction tests performed by varying the overall load, reproduced from ref. 338 with permission from Elsevier, copyright 2021. (g) Lubrication effect of MXene-derived compounds for interlayer and substrate adhesion. (h) Potential corrugation values for homogeneous and heterogeneous MXene terminations on interfaces. (i) Potential corrugation growth as a function of applied normal load, reproduced from ref. 340 with permission from American Chemical Society, copyright 2022.

4.6. Role of MXene in tribology applications

Recently, MXene-derived compounds have been developed for utilization in tribology because they are excellent lubricating agents in solid and liquid forms. They have extraordinary lubricating characteristics suitable for enhancing the quality of lubricants.[335] Using MXene-derived lubricants, the effectiveness of mechanical instruments is significantly improved. For an environmental viewpoint, better tribological performances are expected to minimize gas emissions for environmental hazards. Utilization of MXene-based materials in tribology is a novel and relatively unexplored area of research.[223] Fig. 21a is a schematic illustration of tetradecylphosphonic acid (TDPA) grafted to Ti_3C_2. Fig. 21b and c demonstrates that the average coefficient of friction and wear rate for three samples (castor oil, castor oil with 0.1 wt% Ti_3C_2, and 0.1 wt% TDPA-Ti_3C_2). It has been predicted that the presence of –OH groups in the MXene-EG coating causes a significant reduction in shear force.[336] In turn, this reduction decreases interlayer slip during friction and facilitates the formation of a more compact friction-transfer film (Fig. 21d). The reduction in direct contact between surfaces was greater with a MXene coating, which led to a reduction in frictional characteristics.[337] It has been reported that, amount of coating of The MXene also influenced friction. The coating maintained a low coefficient of friction (0.16) at 1.0 mL. This value changed to 0.6 mL during friction tests because this coating was removed quickly (Fig. 21e). The results of gradient friction tests conducted on MXene-EG coatings employing different loads on MXene-EG are shown in Fig. 21f.[338] The lubrication effect of a MXene on the interlayer and substrate adhesion are illustrated in Fig. 21g. Fig. 21h illustrates the possibility for corrugation without applying an external load on homogeneous and heterogeneous MXene contacts. In this context, the weighted sum of enclosed pixels (WSEP) is a hurdle for two neighbouring layers of a MXene to slide upon each other.[339] Fig. 21i demonstrates how the potential corrugation changes depending on the typical stress placed on the upper slab of a MXene bilayer. This phenomenon is more commonly observed in bilayers that have –OH terminations at interfaces.[340]

Table 9 Comparative summary of tribological performances of MXene-based compounds

Types of MXene	Friction pairs	Testing parameters	Lubrication mechanism	Outcomes	Ref.
Ti_3C_2	Probe: MESP-HM	30 nN–8 μN, 25–40 °C, velocity 0.2–1.0 μm, delay time 1–5 s, RH 20%	Structure change	The first research on micro-tribology of MXene	341
Ti_3C_2, F-Ti_3C_2 & TMA-Ti_3C_2	Probe: nitride	0–30 nN, RH 15–45%, 24 °C	Surface properties	Distinct tribological properties of different modified Ti_3C_2 dependent on hydrophilicity	342
PTFE/Al^{3+}-MXene	Ball: GCr15, Φ 3 mm; disk: PTFE/Al^{3+}-MXene heterogeneous coating on Si wafers	1 N, 1 Hz, 4 mm, 27 ± 2 °C, RH 24 ± 2%	Synergistic effect of Al^{3+}-MXene coating and PTFE	Preparation of friction-induced PTFE/Al^{3+}-MXene film, and formation of secondary transfer film	343
Ti_3C_2/graphene oxide	Ball: AISI 52100 bearing steel; disk: copper disk (20 × 15 × 2 mm)	1 N, 200 rpm, 2 mm	Transferred film and evenly distributed tribolayer	N/A	344

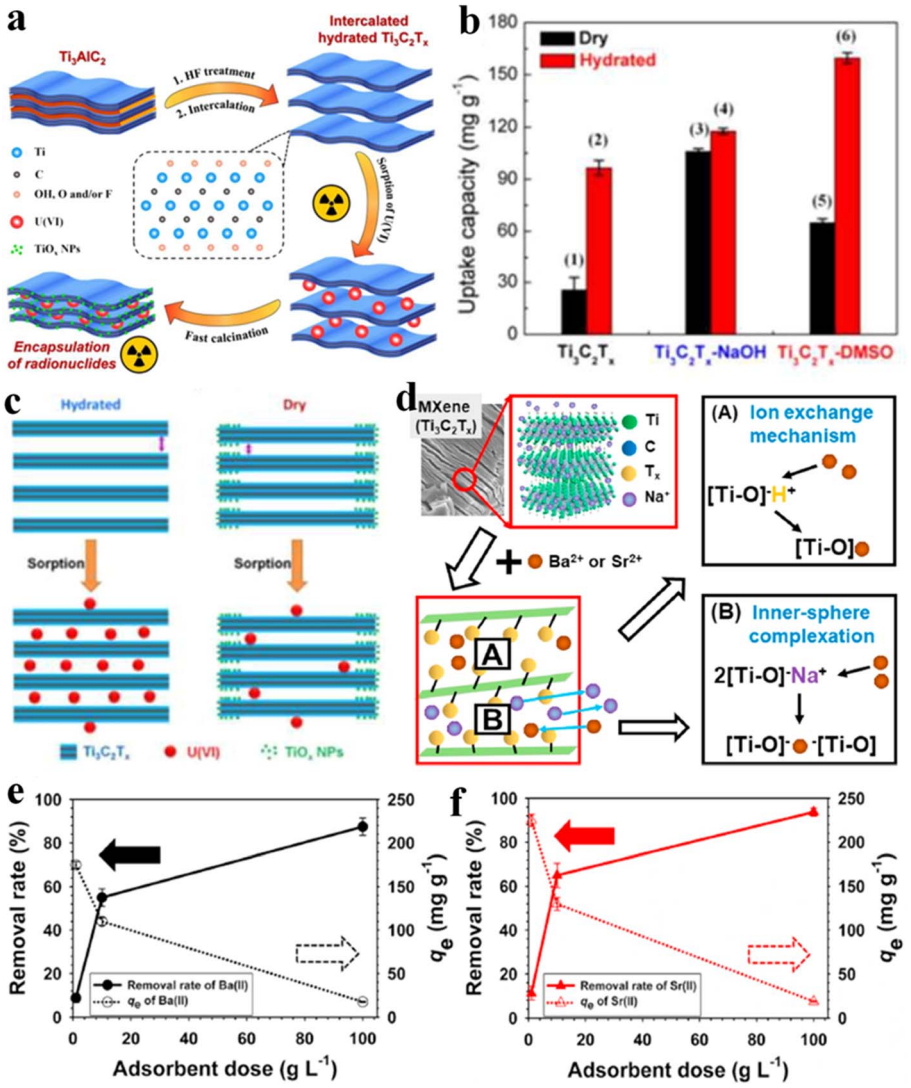

Fig. 22 (a) Synthesis of $Ti_3C_2T_x$ *via* a hydrated-intercalation approach. (b) Comparative performances obtained for $Ti_3C_2T_x$, $Ti_3C_2T_x$-NaOH, and $Ti_3C_2T_x$-DMSO. (c) Sorption of U(VI) on hydrated and dry MXenes, reproduced from ref. 361 with permission from Royal Society of Chemistry, copyright 2017. (d) Adsorption of Ba/Sr *via* MXene. (e) Percentage removal and q_e (mg g^{-1}) of Ba and (f) percentage removal and q_e (mg g^{-1}) of Sr by increasing the dose of MXene (g L^{-1}), reproduced from ref. 362 with permission from Elsevier, copyright 2020.

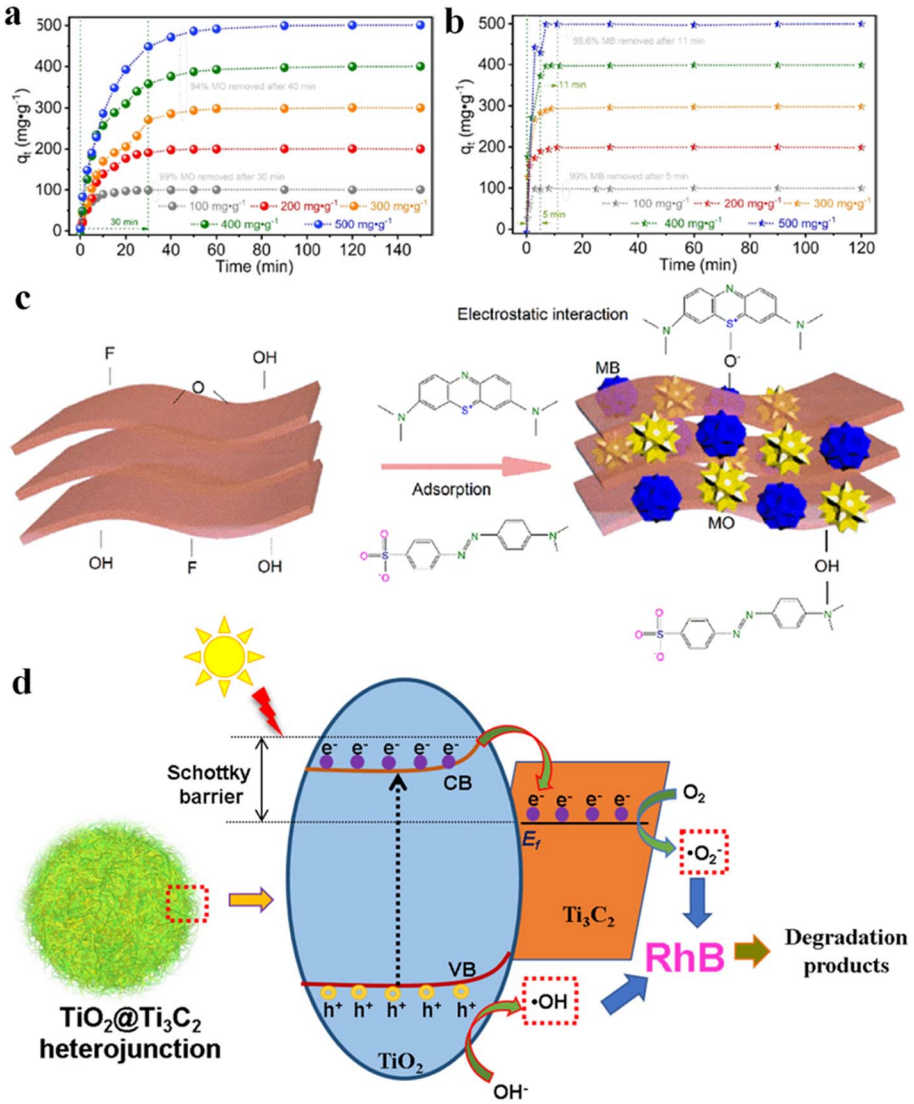

Fig. 23 (a) Adsorption of methyl orange on Nb_2CT_x and (b) adsorption of methylene blue at various contact times. (c) Dye adsorption *via* electrostatic interactions, reproduced from ref. 363 with permission from American Chemical Society, copyright 2021. (d) Photocatalytic degradation of RhB *via* $TiO_2@Ti_3C_2$, reproduced from ref. 364 with permission from Elsevier, copyright 2021.

4.6.1 Advantages and drawbacks. The special features of MXenes are exceptional mechanical strength and wear resistance. These characteristics make MXenes excellent candidates for applications in tribology. MXenes can enhance the durability of lubricants markedly, which leads to the long life of mechanical applications. As lubricating agents, the main features of MXenes are oxidation/destabilization in harsh tribological environments.

4.6.2 Suggestions and precautions. MXenes require protective coatings or modifications to maintain their effectiveness under extreme conditions. Thus, conducting compatibility tests of a lubricant to other ingredients before employment in mechanical applications is a rational approach. In some cases, materials may react adversely with MXene-based lubricants. Applications of MXene reported specifically for tribological performances are shown in Table 9

4.7. Application of MXenes for water treatment

MXenes have been at the forefront of research on water treatments as photocatalysts or membranes to remove toxic pollutants. Wastewater containing antibiotics such as tetracycline, lincomycin, sulfonamides, and fluoroquinolones arising from animal farming, industries, and hospitals are treated with MXene-supported compounds to separate microbes.[47,345–348] Water arising from mining, metal extraction and industrial processes containing hazardous metal ions (*e.g.*, Zn^{2+}, Cd^{2+}, Pb^{2+}, Cr^{6+} and Cu^{2+}) can be treated to obtain natural water systems.[349–354] Karthikeyan[355] reported on the ability of MXenes to absorb and remove Cr(VI) and MO from water. According to Wang *et al.*,[356] biosurfactants along with MXene nanosheets enhance the adsorption of Pb(II) from contaminated water. Similarly, removal of mercury ions (Hg^{2+}) on nanolayered molybdenum disulfide (MoS_2/MX-II)-functionalized MXene has

Table 10 MXenes employed for the removal of selected pollutants

Membrane	Pollutant	Conc. (mg L^{-1})	Efficiency (%)	Ref.
$Ti_3C_2T_x$ MXene nanosheets	Cytochrome C	20	97 ± 1	366
$Ti_3C_2T_x$ MXene nanosheets	Evans blue (EB)	10	90 ± 1	366
Thermal cross-linked 2-D MXenes ($Ti_2C_3T_x$)	Pb^{2+}	100	Hydrated rejection of Pb^{2+}: 99	367
PFDTMS-modified hydrophobic 2-D d-Ti_3C_2 membrane	Cu^{2+}	NA	100	368
MXene-anchored goethite heterogeneous Fenton composite	Hg^{2+}	60	99.7	369

been reported by Shahzad *et al.*[357] Jun *et al.* reported successful removal of radioactive Cs^+ from nuclear wastewater *via* a MXene.[358]

Furthermore, Ti_2CT_x has been reported to remove uranium efficiently *via* a sorption–reduction method. MXene nanosheets functionalized with nanolayered MoS_2 have been found to be effective for the treatment of wastewater having uranium contents.[359] Removal of several medicinal substances on $Ti_3C_2T_x$ was reported by Yoon *et al.*[360] Fig. 22a shows the synthesis and sorption mechanisms of $Ti_3C_2T_x$. Significant adsorptive removal of radionuclides on $Ti_3C_2T_x$ was achieved through a hydrated-intercalation strategy. $Ti_3C_2T_x$-DMSO-

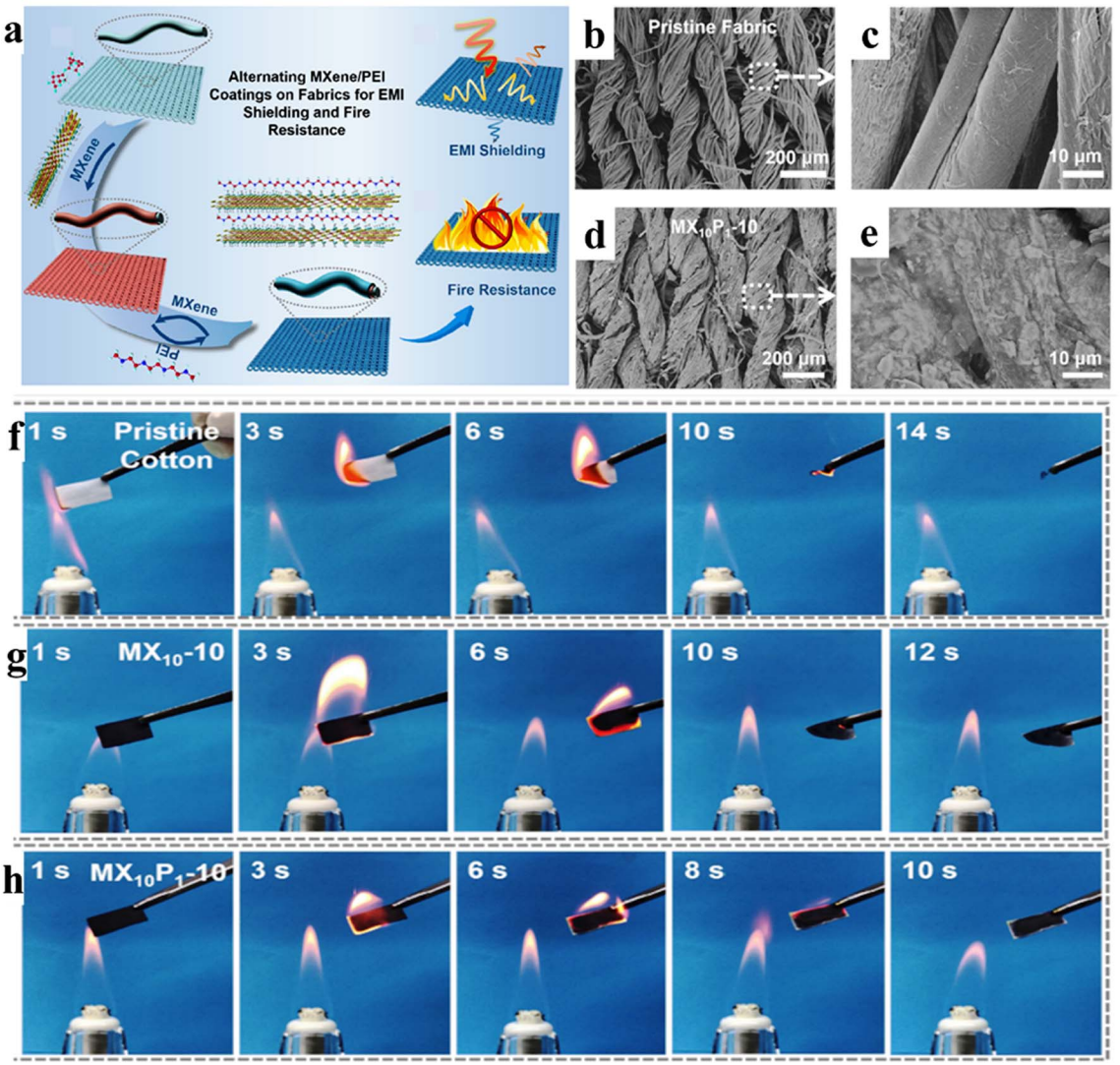

Fig. 24 (a) Assembly of a MXene/PEI-coated fabric. (b and c) SEM images of pristine cotton fabric. (d and e) SEM images of $MX_{10}P_1$-10. (f–h) Investigation of the fireproof properties of MX_{10}-10 and $MX_{10}P_1$-10 fabrics, reproduced from ref. 370 with permission from American Chemical Society, copyright 2021.

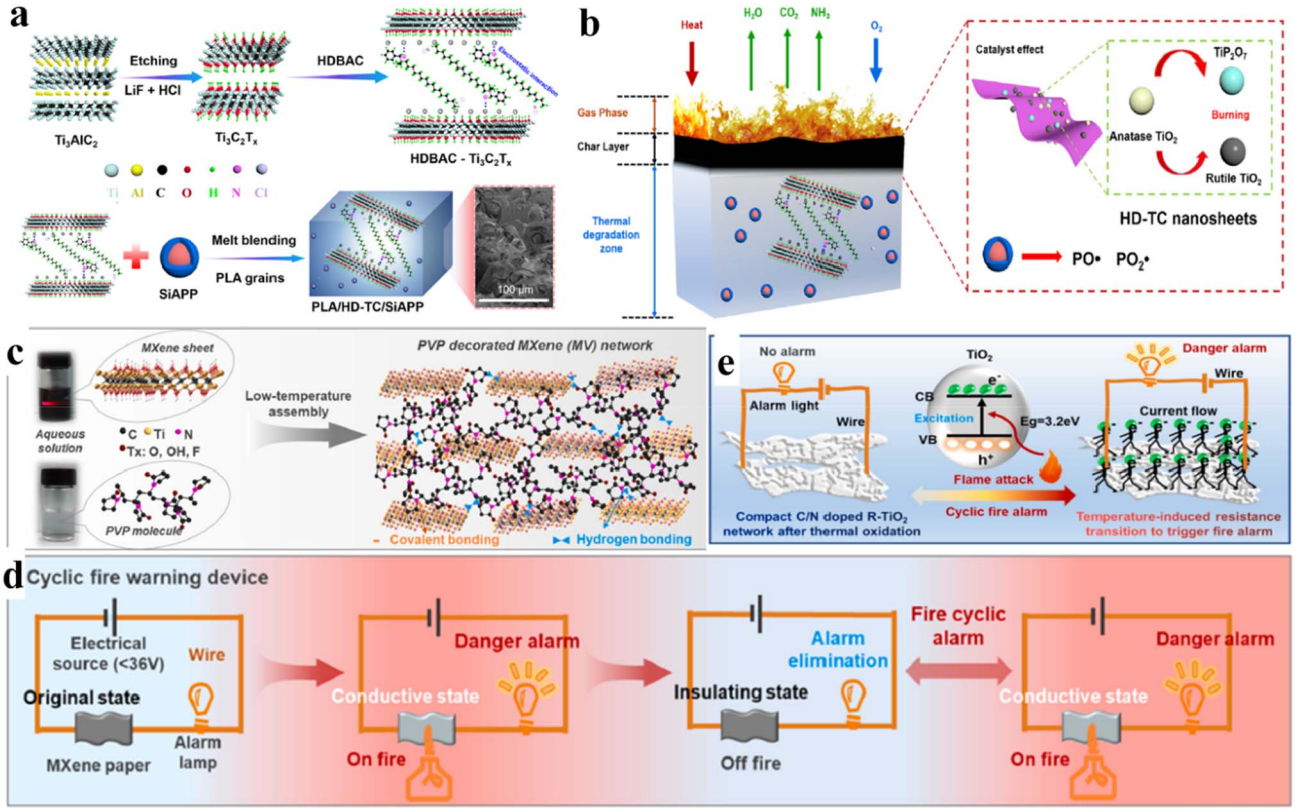

Fig. 25 (a) Synthetic scheme for HDBAC-$Ti_3C_2T_x$ and PLA/HD-TC/SiAPP. (b) Flame-retardant mechanism, reproduced from ref. 373 with permission from Elsevier, copyright 2022. (c) Low-temperature assembly for PVP-decorated MXene paper. (d) MXene paper-based fire-detecting sensing device (schematic). (e) Resistance transition mechanism of a C/N-doped TiO_2 network, reproduced from ref. 374 with permission from Elsevier, copyright 2022.

Table 11 Flame-retardant MXene-associated materials based on neat MXenes

Material	Structure	MXene (wt%)	(PHRR) reduction	Thermal conductivity ($W\ m^{-1}\ K^{-1}$)	Combustion performance	Ref.
MXene/CNF	Film	60	77.8	14.93	No ignition	376
MXene/PI	Film	40	77.2	5.12 ± 0.37	Self-extinction	377
MXene/GO	Film	40	97.7	26.49	No ignition	378
MXene/PI	Aerogel	16.1	42.0	N/A	No ignition	379
Wood/MXene	Coating	13.1	58.8	N/A	No ignition	380

hydrated (Fig. 22b) demonstrated the highest removal (160 mg g^{-1}) for U(VI) compared with $Ti_3C_2T_x$-dry (26 mg g^{-1}). In particular, 1 kg of $Ti_3C_2T_x$-DMSO-hydrated could treat nearly 5000 kg of uranium-containing wastewater, reducing the residual U(VI) content to <15 μg L^{-1}. These reports align with WHO standards for the development and delivery of safe drinking water.[361] The proposed mechanism demonstrates the sorption of uranium by hydrated/dry $Ti_3C_2T_x$ (Fig. 22c).[361] The mechanism for the removal of toxic metals *via* MXenes is discussed in ESI Section S5.‡

MXenes have been utilized for the removal of alkaline-earth metal ions. Fig. 22d is a schematic diagram of the adsorption mechanism of Ba/Sr ions. Studies have illustrated the remarkable adsorption of Ba^{2+} (180 mg g^{-1}) and Sr^{2+} (225 mg g^{-1}) on MXenes, (Fig. 22e and f, respectively).[362] Fig. 23a and b show the relationship between the adsorption capacity of Nb_2CT_x and contact time for MO and MB removal.[363] Fig. 23c shows a dye-adsorption process that offers a promising approach for the removal of dyes from wastewater. Fig. 23d demonstrates the mechanism of degradation for RhB dye over TiO_2/Ti_3C_2 photocatalysts.[364,365] These applications demonstrate the effectiveness of MXenes for wastewater-treatment technologies.

4.7.1 Advantages and drawbacks. Due to their excellent adsorption properties, MXenes can efficiently remove heavy metals, radioactive contaminants, organic pollutants, and other toxins from polluted water. Their high adsorption capacity makes them promising materials for water purification/

treatment technologies. The stability and scalability of MXenes are the main limitations for large-scale applications.

4.7.2 Suggestions and precautions. The rate of adsorption must be monitored to optimize the contact time and design for water-treatment systems. The optimized capacity is important because certain contaminants may be adsorbed more readily than others, so choosing or modifying MXenes accordingly is important.

Table 10 demonstrates the MXene-supported materials used for the removal of selected pollutants.

4.8. Applications of MXenes for fire retardancy/warning

MXenes exhibit great potential as flame-retardant polymers. Some reports have indicated that TiO_2 formed *in situ* on MXene surfaces exhibits a significant fire-inhibitory effect.[370] Polyethylenimine (PEI) and MXenes have been introduced to fire-retardant materials because they can efficiently slow down the speed of fires.[371] Liu *et al.* developed a flame-resistant cotton fabric using a layer-by-layer deposition technique. These layers consisted of PEI, MXene, ammonium polyphosphate (APP) and silicone elastomer.[372] Fig. 24a illustrates the assembly and fireproof properties of MXene/PEI-coated fabrics. Fig. 24b and c illustrate the SEM images (at 200 and 10 μm) of pristine cotton fabric material.[371] Furthermore, Fig. 24d and e demonstrate the SEM images of MXene/PEI-coated fabrics. Comparison of the fire-resistance properties of pristine cotton and MXene/PEI-coated fabric has been justified *via* digital photographs (Fig. 24f–h).[371] Similarly, preparation of the flame-retardant materials HDBAC-$Ti_3C_2T_x$ and PLA/HD-TC/SiAPP is illustrated in Fig. 25a. The flame-resistance mechanism over PLA/HD-TC/SiAPP composite has been illustrated in Fig. 25b.[373] The low-temperature evaporation assembly method to synthesize MXene-polymer papers (PVP) is demonstrated in Fig. 25c.[374]

Fig. 25d demonstrates a fire-warning sensor device. This device has been constructed by connecting a modified MXene paper at a low-voltage (36 V) assisted with an alarm bulb. The purpose of this setup is to detect flames. Fig. 25e is a schematic diagram illustrating the resistance mechanism of a C/N-doped TiO_2 network during cyclic flame detection. When this network exposed to flames, the temperature rise leads to a change in electrical conductivity.[374] This variation in conductivity results in a transition of the resistance. By monitoring resistance transition, the presence and intensity of flames can be detected.[375] Various reported MXene-based flame-retardant materials with their values for thermal conductivity (W m^{-1} K^{-1}), combustion performance, and PHRR reduction are represented in Table 11.

4.8.1 Advantages and drawbacks. MXenes exhibit excellent flame-retardant properties, and can enhance the fire resistance of polymers and textiles materials. Due to their ability to form protective layers, MXenes can be preferred to other fire-retardant materials. The significant advantage is that they can provide "passive" fire protection; fewer flames spread in the case of a fire. However, the environmental impact of MXene-based fire retardant materials requires attention because these can release some harmful byproducts during combustion.

4.8.2 Suggestions and precautions. Surface modification or blending methods are preferable for the uniform dispersion of MXenes to develop fire-retardant fabrics. Various methods can be used to integrate the MXene into polymers and textiles effectively. Advanced research on the toxicity of MXene-based fire retardants is lacking. The spread of combustion products

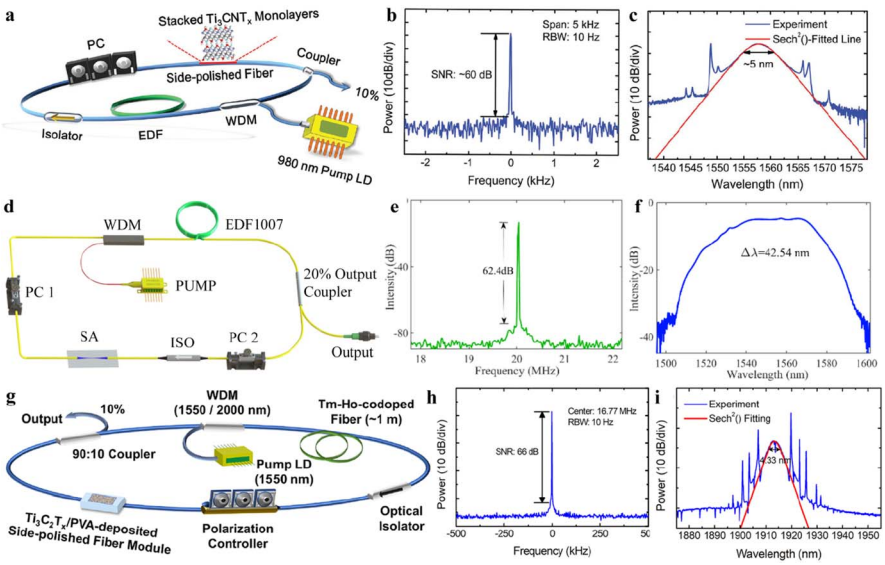

Fig. 26 (a) Scheme used for a fiber laser incorporated stacked Ti_3CNT_x for SAs. (b) Electrical spectrum. (c) Optical spectrum of output pulses, reproduced from ref. 381 with permission from Wiley, copyright 2017. (d) Stretched-pulse mode-locked fiber laser scheme. (e) RF spectrum. (f) Optical spectra, reproduced from ref. 386 with permission from Optica, copyright 2019 (g) ring-cavity Tm-Ho-co-doped fiber laser system (schematic). (h and i) Electrical and optical spectrum of output laser pulses, reproduced from ref. 388 with permission from De Gruyter, copyright 2021.

Table 12 Operational parameters of a mode-locked fiber laser employing MXene-based saturable absorbers

Material	SA structure	Deposition technique	λ_c (nm)	$\Delta\lambda$ (nm)	SNR (db)	Repetition rate (MHz)	Ref.
$Ti_3C_2T_x$	Tapered fiber	Optical deposition	1564.24	5.21	55.2	17.9	386
$Ti_3C_2T_x$	Tapered fiber	Optical deposition	1069.17	4.29	68	4.77	387
V_2CT_x	Tapered fiber	Optical deposition	≈1064	3	71	38.5	383
$Ti_3C_2T_x$	D-shaped fiber	Drop casting	1913.7	4.33	66	16.77	388
Ti_2AlC	Fiber ferrule	Film attachment	1559	N/A	64.6	5.16	389

may become more risky and challenging. Thus, no release of harmful gases or residues is mandatory during fire exposure.

4.9. Application of MXenes in mode-locked fiber lasers

MXenes have been identified as replacements of traditional saturable absorbers (SAs) such as graphene and carbon nanotubes. The major characteristics that make MXenes excellent candidates for SAs are: (i) high saturable absorption; (ii) remarkable modulation depth; (iii) flexible bandgap; (iv) electron density near to Fermi levels. According to Jhon *et al.*[381] utilization of MXenes as SAs in mode-locked fiber lasers is a promising application. Fig. 26a illustrates the scheme of fiber laser-stacked Ti_3CNT_x SAs. The setup includes a polarization controller (PC), erbium-doped fiber (EDF), wavelength division multiplexer (WDM), and laser diode (LD).[382] Output pulses for electrical and optical spectral results are demonstrated in Fig. 26b and c, respectively. A MXene-SA device on the stretched-pulse mode-locked fiber laser is illustrated in Fig. 26d. The radiofrequency spectrum exhibited in Fig. 26e demonstrates a signal-to-background difference of 62.4 dB.[383] The typical spectrum of the mode-locked ultra-short pulse is shown in Fig. 26f. The central wavelength of the ring-cavity Tm-Ho-co-doped fiber laser system was 1550 nm along with a spectral FWHM of 42.54 nm. Fig. 26g is a schematic diagram of this fiber laser system. The Tm-Ho-codoped fiber laser system allows deep understanding of its configuration and functionality.[384] Highly stacked $Ti_3C_2T_x$ SAs were used to generate a relatively stable mode-locked laser system (Fig. 26h.) Analysis of the electrical spectrum revealed distinct peaks at a repetition rate of 16.77 MHz, exhibiting a signal-to-noise ratio of 66 dB. The optical spectra of pulses and fitting in the $Sech^2$ curve for solitons is represented in Fig. 26i. The centre wavelength was determined to be 1913.7 nm, whereas the bandwidth of output pulses was 4.33 nm.[385] Table 12 provides a comprehensive overview of mode-locked fiber lasers derived from MXene-based SAs.

4.9.1 Advantages and drawbacks. MXenes serve as SAs that enable mode-locking in fiber lasers (an advanced application). MXene-based SAs offer various advantages, such as high modulation depth, ultrafast recovery time, and stable operation. The only drawback is integration of the MXene-based components into the fiber laser system. The stability and reliability of MXene-based SAs are crucial components for practical application in fiber lasers.

4.9.2 Suggestions and precautions. Due to unique characteristics, the use of MXene-based SAs to fiber laser systems is recommended. Necessary parameters are: (i) saturable absorption potential; (ii) modulation depth; (iii) flexible bandgap; (iv) electron density in Fermi levels should be optimized to achieve desired pulse durations for specific applications. To avoid accidental exposure to laser radiation, protective shielding and safety measures must be assured.

5. Conclusions

This review article delivers up-to-date information about the synthetic methods, mechanism, terminations, modifications, and important applications of MXenes. We highlight the advantages, drawbacks, suggestions, and precautions associated with MXene synthesis and applications. Each synthetic method has advantages and disadvantages. MXene synthesis is mostly reliant on etching of the A-layer. However, most etching methods are scientifically and economically challenging. Development of MXenes by CVD is a cost-effective and efficient "bottom-up" synthetic method. Controllable doping and surface terminations on MXenes have important roles for specific and targeted applications. The inherited properties of MXene (relatively higher thermal and electrical conductivity, mechanical strength, hydrophilicity, and structural stability) have been validated *via* interactions with other materials for the design of state-of-the-art applications. The composition of surface terminations is predominantly affected by the type of etching agent along with its concentration. For example, fluorine-based etching methods typically have hydrophilic terminations, such as –OH, =O, and –F, whereas electrochemical and alkali etching are less effective for some applications. MXenes with single terminations can be synthesized by molten salt etching. Sulfur terminations of MXenes exhibit remarkable performances for batteries and supercapacitors. F-terminated MXenes deliver excellent performances for electrocatalytic reactions, whereas N-doped MXenes exhibit exceptional electrochemical capabilities for LSBs and energy-storage applications. =O terminations are very effective for photocatalysis, but also for adsorption. We summarized recent developments on MXenes, terminations, and their roles in energy, catalysis, sensing, environment, medicine, water treatment, fire retardation, tribology, and EMI-shielding applications. For example, MXenes and their composites have been employed as catalysts or co-catalysts in electro/photocatalytic water-splitting reactions. Moreover, MXenes and their derived compounds exhibit strong adsorption affinities for the removal of radioisotopes, heavy-metal ions, and carcinogenic dyes from

contaminated water. Additionally, MXenes and their biocompatible composites have been utilized in biosensing applications, or immobilization of enzymes to facilitate electron transfer between enzymes and electrode surfaces. MXenes and MXene-derived compounds have unique and exciting characteristics for state-of-the-art applications. Their excellent conductivity, chemical stability, and tuneable properties promise utilization in many other applications.

6. Future perspectives

• To extend the applications of MXenes, theoretical calculations and simulations need to be performed. Advanced and sophisticated experimental setups may require endorsement for new applications.

• It is essential to explore diverse terminations and their impact on properties for improving the overall performance for targeted applications.

• For precise control of the synthesis and terminations, extra attention should be given to post-etching processing.

• The interface properties of MXene nanosheets with various other materials must be investigated.

• Changes in terminations that govern applications are unclear. Hence, sophisticated technologies that can extend utilization even in humid, oxygen, or high temperatures are needed.

• Discovery of new precursors rather than the MAX phase can open new synthetic routes for MXenes.

• Alternative synthetic methods may aid the design and morphologies of MXenes for targeted applications.

• Substitutes for MXenes, such as oxycarbides and oxynitrides, may need to be discovered for state-of-the-art applications.

• The conductivity of MXenes can be controlled by employing structural changes to selective applications such as electronic, semiconductor, and sensing devices.

Abbreviations

Ti_3C_2	Titanium carbide
RhB	Rhodamine B
EHDA	Electro hydrodynamic atomization
MO	Methyl orange
SE	Shielding efficiency
DFT	Density functional theory
NEB	Nudge elastic band
LSBs	Lithium–sulfur batteries
QD	Quantum dots
MA	Microwave absorption
MSC	Micro supercapacitor
ECSDs	Energy conversion and storage devices
SNR	Signal-to-noise ratio
RBW	Resolution bandwidth
LIBs	Lithium-ion batteries
SIBs	Sodium-ion batteries
CDCs	Carbon-derived carbides
MILD	Minimally intensive layer delamination
MMF	MXene membrane filter
PES	Photoelectron spectroscopy
HER	Hydrogen-evolution reaction
EDLC	Electric double-layer capacitor
AC	Ammonium citrate
CV	Cyclic voltammetry
RES	Reticuloendothelial system
SCs	Super capacitors
OCVs	Open-circuit voltages
DMF	Dimethylformamide
PAN	Polyacrylonitrile
ACN	Acetonitrile
PI	Polyimide
PSC	Perovskite solar cell
MQDs	MXene quantum dots
EMI	Electromagnetic interference
SA	Sodium alginate
PANI	Polyaniline
SAs	Saturable absorbers
TDPA	Tetradecylphosphonic acid
WSEP	Weighted sum of enclosed pixels
PRBs	Permeable reactive barriers
PVA	Polyvinyl alcohol
ETLs	Electron transport layers
PHRR	Peak heat release rate
EQE	External quantum efficiency
APP	Ammonium polyphosphate
WDM	Wavelength division multiplexer
PC	Polarization controller
EDF	Erbium-doped fiber
LD	Laser diode

Conflicts of interest

The authors announce no conflict of financial interests.

Acknowledgements

The authors acknowledge the Higher Education Commission of Pakistan for funding support ((377/IPFP-II, Batch-I)/SRGP/NAHE/HEC/2020/27). Dr Ejaz Hussain thanks Carnegie Mellon University (USA) and Ministry of Science and Technology of Pakistan for scientific support. This scientific contribution is highly credited to the resources of the Inorganic Material Laboratory (52S), Institute of Chemistry, Islamia University of Bahawalpur, Pakistan.

References

1 H. Zhang, *ACS Nano*, 2015, **9**, 9451–9469.
2 H. D. Mai, K. Rafiq and H. Yoo, *Chem.–Eur. J.*, 2017, **23**, 5631–5651.
3 Y. Gogotsi and B. Anasori, *ACS Nano*, 2019, **13**, 8491–8494.
4 M. Dahlqvist, M. W. Barsoum and J. Rosen, *Mater. Today*, 2023, DOI: **10.1016/j.mattod.2023.11.010**.

5 M. Li, J. Lu, K. Luo, Y. Li, K. Chang, K. Chen, J. Zhou, J. Rosen, L. Hultman and P. Eklund, *J. Am. Chem. Soc.*, 2019, **141**, 4730–4737.
6 L. Fu and W. Xia, *Adv. Eng. Mater.*, 2021, **23**, 2001191.
7 R. Qin, G. Shan, M. Hu and W. Huang, *Mater. Today Phys.*, 2021, **21**, 100527.
8 K. R. G. Lim, M. Shekhirev, B. C. Wyatt, B. Anasori, Y. Gogotsi and Z. W. Seh, *Nat., Synth.*, 2022, **1**, 601–614.
9 B. Anasori, J. Halim, J. Lu, C. A. Voigt, L. Hultman and M. W. Barsoum, *Scr. Mater.*, 2015, **101**, 5–7.
10 T. Bashir, S. A. Ismail, J. Wang, W. Zhu, J. Zhao and L. Gao, *J. Energy Chem.*, 2023, **76**, 90–104.
11 C. Lamiel, I. Hussain, O. R. Ogunsakin and K. Zhang, *J. Mater. Chem. A*, 2022, **10**, 14247–14272.
12 Y.-T. Du, X. Kan, F. Yang, L.-Y. Gan and U. Schwingenschlogl, *ACS Appl. Mater. Interfaces*, 2018, **10**, 32867–32873.
13 J. Miao, Q. Zhu, K. Li, P. Zhang, Q. Zhao and B. Xu, *J. Energy Chem.*, 2021, **52**, 243–250.
14 J. Xu, X. Hu, X. Wang, X. Wang, Y. Ju, S. Ge, X. Lu, J. Ding, N. Yuan and Y. Gogotsi, *Energy Storage Mater.*, 2020, **33**, 382–389.
15 L. Wang, Y. Lai, H. Tian, J. Wang, W. Zhao, Y. Wang, L. Li and L. Zhang, *J. Alloys Compd.*, 2023, **945**, 169366.
16 Y. Gao, Z. Tang, X. Chen, J. Yan, Y. Jiang, J. Xu, Z. Tao, L. Wang, Z. Liu and G. Wang, *Aggregate*, 2023, **4**, e248.
17 Y. Wang, Z. Luo, Y. Qian, W. Zhang and L. Chen, *Chem. Eng. J.*, 2023, **454**, 140513.
18 K. Hantanasirisakul and Y. Gogotsi, *Adv. Mater.*, 2018, **30**, 1804779.
19 M.-s. Cao, Y.-Z. Cai, P. He, J.-C. Shu, W.-Q. Cao and J. Yuan, *Chem. Eng. J.*, 2019, **359**, 1265–1302.
20 Y. Cheng, Y. Xie, Z. Liu, S. Yan, Y. Ma, Y. Yue, J. Wang, Y. Gao and L. Li, *ACS Nano*, 2023, **17**, 1393–1402.
21 Y. Cheng, Y. Xie, Y. Ma, M. Wang, Y. Zhang, Z. Liu, S. Yan, N. Ma, M. Liu and Y. Yue, *Nano Energy*, 2023, **107**, 108131.
22 S. Chertopalov and V. N. Mochalin, *ACS Nano*, 2018, **12**, 6109–6116.
23 X. Zhan, C. Si, J. Zhou and Z. Sun, *Nanoscale Horiz.*, 2020, **5**, 235–258.
24 X. Ma, A. Wang, J. Miao and T. Fan, *Sep. Purif. Technol.*, 2023, 123248.
25 Y. Chen, P. Zhao, Y. Liang, Y. Ma, Y. Liu, J. Zhao, J. Hou, C. Hou and D. Huo, *Talanta*, 2023, 124294.
26 K. Zhao, J. W. Lee, Z. G. Yu, W. Jiang, J. W. Oh, G. Kim, H. Han, Y. Kim, K. Lee and S. Lee, *ACS Nano*, 2023, **17**, 5472–5485.
27 A. Sinha, H. Zhao, Y. Huang, X. Lu, J. Chen and R. Jain, *TrAC, Trends Anal. Chem.*, 2018, **105**, 424–435.
28 S. Hroncekova, T. Bertok, M. Hires, E. Jane, L. Lorencova, A. Vikartovska, A. Tanvir, P. Kasak and J. Tkac, *Processes*, 2020, **8**, 580.
29 Y. Lei, W. Zhao, Y. Zhang, Q. Jiang, J. H. He, A. J. Baeumner, O. S. Wolfbeis, Z. L. Wang, K. N. Salama and H. N. Alshareef, *Small*, 2019, **15**, 1901190.
30 L. Wu, X. Lu, Z.-S. Wu, Y. Dong, X. Wang, S. Zheng and J. Chen, *Biosens. Bioelectron.*, 2018, **107**, 69–75.
31 H. Gu, Y. Xing, P. Xiong, H. Tang, C. Li, S. Chen, R. Zeng, K. Han and G. Shi, *ACS Appl. Nano Mater.*, 2019, **2**, 6537–6545.
32 H. L. Chia, C. C. Mayorga-Martinez, N. Antonatos, Z. k. Sofer, J. J. Gonzalez-Julian, R. D. Webster and M. Pumera, *Anal. Chem.*, 2020, **92**, 2452–2459.
33 S. J. Kim, H.-J. Koh, C. E. Ren, O. Kwon, K. Maleski, S.-Y. Cho, B. Anasori, C.-K. Kim, Y.-K. Choi and J. Kim, *ACS Nano*, 2018, **12**, 986–993.
34 A. Shahzad, K. Rasool, M. Nawaz, W. Miran, J. Jang, M. Moztahida, K. A. Mahmoud and D. S. Lee, *Chem. Eng. J.*, 2018, **349**, 748–755.
35 J. Peng, X. Chen, W.-J. Ong, X. Zhao and N. Li, *Chem*, 2019, **5**, 18–50.
36 Y. Wei, R. A. Soomro, X. Xie and B. Xu, *J. Energy Chem.*, 2021, **55**, 244–255.
37 Z. Li, S. Ning, F. Hu, H. Zhu, L. Zeng, L. Chen, X. Wang, T. Fujita and Y. Wei, *J. Colloid Interface Sci.*, 2023, **629**, 97–110.
38 P. D. Kolubah, H. O. Mohamed, M. Ayach, A. R. Hari, H. N. Alshareef, P. Saikaly, K.-J. Chae and P. Castaño, *Chem. Eng. J.*, 2023, **461**, 141821.
39 K. Huang, Z. Li, J. Lin, G. Han and P. Huang, *Chem. Soc. Rev.*, 2018, **47**, 5109–5124.
40 J. Xu, L. Chen, S. Ding, X. Dai, Y. Dai, Y. Chen and X. Ni, *Nano Today*, 2023, **48**, 101750.
41 Y.-U. Haq, R. Ullah, S. Mazhar, R. Khattak, A. A. Qarni, Z.-U. Haq and S. Amin, *J. Sci.: Adv. Mater. Devices*, 2022, **7**, 100390.
42 D. Chen, J. Yu, Z. Cui, Q. Zhang, X. Chen, J. Sui, H. Dong, L. Yu and L. Dong, *Electrochim. Acta*, 2020, **331**, 135394.
43 A. Liu, X. Liang, X. Ren, W. Guan and T. Ma, *Electrochem. Energy Rev.*, 2022, 1–33.
44 E. Hussain, I. Majeed, M. A. Nadeem, A. Badshah, Y. Chen, M. A. Nadeem and R. Jin, *J. Phys. Chem. C*, 2016, **120**, 17205–17213.
45 F. Saleem, M. Z. Abid, K. Rafiq, A. Rauf, K. Ahmad, S. Iqbal, R. Jin and E. Hussain, *Int. J. Hydrogen Energy*, 2024, **52**, 305–319.
46 Y. Liu, S. Chen, K. Li, J. Wang, P. Chen, H. Wang, J. Li and F. Dong, *J. Colloid Interface Sci.*, 2022, **606**, 1435–1444.
47 N. Wajid, K. Rafiq, M. Z. Abid, A. Ilyas, T. Najam, A. Rauf and E. Hussain, *Mater. Chem. Phys.*, 2023, **306**, 128062.
48 E. Hussain, I. Majeed, M. A. Nadeem, A. Iqbal, Y. Chen, M. Choucair, R. Jin and M. A. Nadeem, *J. Environ. Chem. Eng.*, 2019, **7**, 102729.
49 M. Tahir, A. A. Khan, S. Tasleem, R. Mansoor, A. Sherryna and B. Tahir, *J. Energy Chem.*, 2022, **5**, 18–54.
50 K. U. Sahar, K. Rafiq, M. Z. Abid, A. Rauf, U. u. Rehman, M. A. Nadeem, R. Jin and E. Hussain, *Colloids Surf., A*, 2023, **674**, 131942.
51 S. Li, P. Tuo, J. Xie, X. Zhang, J. Xu, J. Bao, B. Pan and Y. Xie, *Nano Energy*, 2018, **47**, 512–518.
52 H. Riazi, S. K. Nemani, M. C. Grady, B. Anasori and M. Soroush, *J. Mater. Chem. A*, 2021, **9**, 8051–8098.
53 A. Ali Khan, M. Tahir and N. Khan, *Energy Fuels*, 2022, **36**, 9821–9843.

54 S.-Y. Pang, Y.-T. Wong, S. Yuan, Y. Liu, M.-K. Tsang, Z. Yang, H. Huang, W.-T. Wong and J. Hao, *J. Am. Chem. Soc.*, 2019, **141**, 9610–9616.
55 M. Li, J. Lu, K. Luo, Y. Li, K. Chang, K. Chen, J. Zhou, J. Rosen, L. Hultman, P. Eklund, P. O. Å. Persson, S. Du, Z. Chai, Z. Huang and Q. Huang, *J. Am. Chem. Soc.*, 2019, **141**, 4730–4737.
56 M. Ghidiu, M. R. Lukatskaya, M.-Q. Zhao, Y. Gogotsi and M. W. Barsoum, *Nature*, 2014, **516**, 78–81.
57 S. Yang, P. Zhang, F. Wang, A. G. Ricciardulli, M. R. Lohe, P. W. Blom and X. Feng, *Angew. Chem.*, 2018, **130**, 15717–15721.
58 S. Zada, W. Dai, Z. Kai, H. Lu, X. Meng, Y. Zhang, Y. Cheng, F. Yan, P. Fu and X. Zhang, *Angew. Chem., Int. Ed.*, 2020, **59**, 6601–6606.
59 Q. Zhang, H. Lai, R. Fan, P. Ji, X. Fu and H. Li, *ACS Nano*, 2021, **15**, 5249–5262.
60 B. Anasori, M. R. Lukatskaya and Y. Gogotsi, *Nat. Rev. Mater.*, 2017, **2**, 1–17.
61 X. Zhang, W. Zhang and H. Zhao, *Int. J. Energy Res.*, 2022, **46**, 15559–15570.
62 Z. Li, L. Wang, D. Sun, Y. Zhang, B. Liu, Q. Hu and A. Zhou, *Mater. Sci. Eng. B*, 2015, **191**, 33–40.
63 W. Sun, S. A. Shah, Y. Chen, Z. Tan, H. Gao, T. Habib, M. Radovic and M. J. Green, *J. Mater. Chem. A*, 2017, **5**, 21663–21668.
64 S. Zada, W. Dai, Z. Kai, H. Lu, X. Meng, Y. Zhang, Y. Cheng, F. Yan, P. Fu, X. Zhang and H. Dong, *Angew. Chem., Int. Ed.*, 2020, **59**, 6601–6606.
65 C. Couly, M. Alhabeb, K. L. Van Aken, N. Kurra, L. Gomes, A. M. Navarro-Suárez, B. Anasori, H. N. Alshareef and Y. Gogotsi, *Adv. Electron. Mater.*, 2018, **4**, 1700339.
66 C. Peng, P. Wei, X. Chen, Y. Zhang, F. Zhu, Y. Cao, H. Wang, H. Yu and F. Peng, *Ceram. Int.*, 2018, **44**, 18886–18893.
67 C. E. Shuck, A. Sarycheva, M. Anayee, A. Levitt, Y. Zhu, S. Uzun, V. Balitskiy, V. Zahorodna, O. Gogotsi and Y. Gogotsi, *Adv. Eng. Mater.*, 2020, **22**, 1901241.
68 S. Zhang, P. Huang, J. Wang, Z. Zhuang, Z. Zhang and W.-Q. Han, *J. Phys. Chem. Lett.*, 2020, **11**, 1247–1254.
69 H. Shi, P. Zhang, Z. Liu, S. Park, M. R. Lohe, Y. Wu, A. Shaygan Nia, S. Yang and X. Feng, *Angew. Chem., Int. Ed.*, 2021, **60**, 8689–8693.
70 G. Wang, N. Jiang, Z. Zhang, G. Wang and K. Cheng, *Appl. Surf. Sci.*, 2022, **604**, 154636.
71 M. S. Bhargava Reddy, S. Kailasa, B. C. G. Marupalli, K. K. Sadasivuni and S. Aich, *ACS Sens.*, 2022, **7**, 2132–2163.
72 V. Sharma, D. Kumar Das, R. K. Gupta, G. Yasin and A. Kumar, *Inorg. Chem. Commun.*, 2022, **141**, 109496.
73 M. Malaki, A. Maleki and R. S. Varma, *J. Mater. Chem. A*, 2019, **7**, 10843–10857.
74 V. Kotasthane, Z. Tan, J. Yun, E. B. Pentzer, J. L. Lutkenhaus, M. J. Green and M. Radovic, *ACS Appl. Nano Mater.*, 2023, **6**, 1093–1105.
75 X. Sheng, S. Li, H. Huang, Y. Zhao, Y. Chen, L. Zhang and D. Xie, *J. Mater. Sci.*, 2021, **56**, 4212–4224.
76 J. Halim, M. R. Lukatskaya, K. M. Cook, J. Lu, C. R. Smith, L.-Å. Näslund, S. J. May, L. Hultman, Y. Gogotsi and P. Eklund, *Chem. Mater.*, 2014, **26**, 2374–2381.
77 Y. Hai, S. Jiang, C. Zhou, P. Sun, Y. Huang and S. Niu, *Dalton Trans.*, 2020, **49**, 5803–5814.
78 C. E. Shuck, K. Ventura-Martinez, A. Goad, S. Uzun, M. Shekhirev and Y. Gogotsi, *ACS Chem. Health Saf.*, 2021, **28**, 326–338.
79 J. Wu, Y. Wang, Y. Zhang, H. Meng, Y. Xu, Y. Han, Z. Wang, Y. Dong and X. Zhang, *J. Energy Chem.*, 2020, **47**, 203–209.
80 M. Naguib, M. Kurtoglu, V. Presser, J. Lu, J. Niu, M. Heon, L. Hultman, Y. Gogotsi and M. W. Barsoum, *Adv. Mater.*, 2011, **23**, 4248–4253.
81 M. Tang, J. Li, Y. Wang, W. Han, S. Xu, M. Lu, W. Zhang and H. Li, *Symmetry*, 2022, **14**, 2232.
82 M. Xiang, Z. Shen, J. Zheng, M. Song, Q. He, Y. Yang, J. Zhu, Y. Geng, F. Yue, Q. Dong, Y. Ge, R. Wang, J. Wei, W. Wang, H. Huang, H. Zhang, Q. Zhu and C. J. Zhang, *Innovation*, 2024, **5**, 100540.
83 D. Xiong, X. Li, Z. Bai and S. Lu, *Small*, 2018, **14**, 1703419.
84 J. Björk and J. Rosen, *Chem. Mater.*, 2021, **33**, 9108–9118.
85 M. Peng, M. Dong, W. Wei, H. Xu, C. Liu and C. Shen, *Carbon*, 2021, **179**, 400–407.
86 R. Jasrotia, J. Prakash, G. Kumar, R. Verma, S. Kumari, S. Kumar, V. P. Singh, A. K. Nadda and S. Kalia, *Chemosphere*, 2022, **294**, 133706.
87 P. Lakhe, E. M. Prehn, T. Habib, J. L. Lutkenhaus, M. Radovic, M. S. Mannan and M. J. Green, *Ind. Eng. Chem. Res.*, 2019, **58**, 1570–1579.
88 T. Zhang, L. Pan, H. Tang, F. Du, Y. Guo, T. Qiu and J. Yang, *J. Alloys Compd.*, 2017, **695**, 818–826.
89 Y. Li, H. Shao, Z. Lin, J. Lu, L. Liu, B. Duployer, P. O. Persson, P. Eklund, L. Hultman and M. Li, *Nat. Mater.*, 2020, **19**, 894–899.
90 J. Lu, I. Persson, H. Lind, J. Palisaitis, M. Li, Y. Li, K. Chen, J. Zhou, S. Du and Z. Chai, *Nanoscale Adv.*, 2019, **1**, 3680–3685.
91 P. Liu, P. Xiao, M. Lu, H. Wang, N. Jin and Z. Lin, *Chin. Chem. Lett.*, 2023, **34**, 107426.
92 W. Sun, S. Shah, Y. Chen, Z. Tan, H. Gao, T. Habib, M. Radovic and M. Green, *J. Mater. Chem. A*, 2017, **5**, 21663–21668.
93 D. Laishram, D. Kumar, K. P. Shejale, B. Saini, Harikrishna, R. Krishnapriya and R. K. Sharma, *Heterog. Nanocatal. Energy Environ. Sustainability*, 2022, **1**, 165–198.
94 L. M. Dong, C. Ye, L. L. Zheng, Z. F. Gao and F. Xia, *Nanophotonics*, 2020, **9**, 2125–2145.
95 F. Gao, C. Xue, T. Zhang, L. Zhang, G. Y. Zhu, C. Ou, Y. Z. Zhang and X. Dong, *Adv. Mater.*, 2023, 2302559.
96 J. Mei, G. A. Ayoko, C. Hu, J. M. Bell and Z. Sun, *Sustainable Mater. Technol.*, 2020, **25**, e00156.
97 S. Iravani, *Ceram. Int.*, 2022, **48**, 24144–24156.
98 J. Yang, W. Bao, P. Jaumaux, S. Zhang, C. Wang and G. Wang, *Adv. Mater. Interfaces*, 2019, **6**, 1802004.
99 X. Xu, L. Yang, W. Zheng, H. Zhang, F. Wu, Z. Tian, P. Zhang and Z. Sun, *Mater. Rep.: Energy*, 2022, 100080.

100 M. Alhabeb, K. Maleski, B. Anasori, P. Lelyukh, L. Clark, S. Sin and Y. Gogotsi, *Chem. Mater.*, 2017, **29**, 7633–7644.
101 H. Diebler, *Inorganica Chim. Acta*, 1983, **79**, 93–94.
102 G. Li, K. Jiang, S. Zaman, J. Xuan, Z. Wang and F. Geng, *Inorg. Chem.*, 2019, **58**, 9397–9403.
103 T. Li, L. Yao, Q. Liu, J. Gu, R. Luo, J. Li, X. Yan, W. Wang, P. Liu and B. Chen, *Angew. Chem., Int. Ed.*, 2018, **57**, 6115–6119.
104 N. H. Solangi, R. R. Karri, S. A. Mazari, N. M. Mubarak, A. S. Jatoi, G. Malafaia and A. K. Azad, *Coord. Chem. Rev.*, 2023, **477**, 214965.
105 Y. Dall'Agnese, M. R. Lukatskaya, K. M. Cook, P.-L. Taberna, Y. Gogotsi and P. Simon, *Electrochem. Commun.*, 2014, **48**, 118–122.
106 D. Sundar, L. Gurusamy, L. Karuppasamy, S. C. Barton and J. J. Wu, in *Noble Metal-Free Electrocatalysts: New Trends in Electrocatalysts for Energy Applications*, ACS Publications, 2022, vol. 2, pp. 151–189.
107 D. J. Kubicki, S. D. Stranks, C. P. Grey and L. Emsley, *Nat. Rev. Chem*, 2021, **5**, 624–645.
108 C. E. Shuck and Y. Gogotsi, *Chem. Eng. J.*, 2020, **401**, 125786.
109 N. Chen, Z. Duan, W. Cai, Y. Wang, B. Pu, H. Huang, Y. Xie, Q. Tang, H. Zhang and W. Yang, *Nano Energy*, 2023, **107**, 108147.
110 H. Shi, P. Zhang, Z. Liu, S. Park, M. R. Lohe, Y. Wu, A. Shaygan Nia, S. Yang and X. Feng, *Angew. Chem., Int. Ed.*, 2021, **60**, 8689–8693.
111 J. Wang, H. Kang, H. Ma, Y. Liu, Z. Xie, Y. Wang and Z. Fan, *Eng. Sci.*, 2021, **15**, 57–66.
112 H. Feng, Q. Tian, J. Huang, X. Cui, J. Jiang, Y. Tian, L. Ye and Q. Xu, *Green Chem.*, 2023, **25**, 3966–3973.
113 D. Wang, C. Zhou, A. S. Filatov, W. Cho, F. Lagunas, M. Wang, S. Vaikuntanathan, C. Liu, R. F. Klie and D. V. Talapin, *Science*, 2023, **379**, 1242–1247.
114 J. Come, M. Naguib, P. Rozier, M. W. Barsoum, Y. Gogotsi, P.-L. Taberna, M. Morcrette and P. Simon, *J. Electrochem. Soc.*, 2012, **159**, A1368.
115 M. Naguib, J. Come, B. Dyatkin, V. Presser, P.-L. Taberna, P. Simon, M. W. Barsoum and Y. Gogotsi, *Electrochem. Commun.*, 2012, **16**, 61–64.
116 Q. Tang, Z. Zhou and P. Shen, *J. Am. Chem. Soc.*, 2012, **134**, 16909–16916.
117 M. Naguib, J. Halim, J. Lu, K. M. Cook, L. Hultman, Y. Gogotsi and M. W. Barsoum, *J. Am. Chem. Soc.*, 2013, **135**, 15966–15969.
118 F. Wang, C. Yang, C. Duan, D. Xiao, Y. Tang and J. Zhu, *J. Electrochem. Soc.*, 2015, **162**, B16.
119 Y. Gao, L. Wang, Z. Li, A. Zhou, Q. Hu and X. Cao, *Solid State Sci.*, 2014, **35**, 62–65.
120 R. B. Rakhi, B. Ahmed, M. N. Hedhili, D. H. Anjum and H. N. Alshareef, *Chem. Mater.*, 2015, **27**, 5314–5323.
121 J. Yang, M. Naguib, M. Ghidiu, L.-M. Pan, J. Gu, J. Nanda, J. Halim, Y. Gogotsi and M. W. Barsoum, *J. Am. Ceram. Soc.*, 2016, **99**, 660–666.
122 M. Hu, Z. Li, H. Zhang, T. Hu, C. Zhang, Z. Wu and X. Wang, *Chem. Commun.*, 2015, **51**, 13531–13533.
123 R. Meshkian, L.-Å. Näslund, J. Halim, J. Lu, M. W. Barsoum and J. Rosen, *Scr. Mater.*, 2015, **108**, 147–150.
124 J. Halim, S. Kota, M. R. Lukatskaya, M. Naguib, M. Q. Zhao, E. J. Moon, J. Pitock, J. Nanda, S. J. May and Y. Gogotsi, *Adv. Funct. Mater.*, 2016, **26**, 3118–3127.
125 K. Rasool, M. Helal, A. Ali, C. E. Ren, Y. Gogotsi and K. A. Mahmoud, *ACS Nano*, 2016, **10**, 3674–3684.
126 J. Zhou, X. Zha, F. Y. Chen, Q. Ye, P. Eklund, S. Du and Q. Huang, *Angew. Chem., Int. Ed.*, 2016, **55**, 5008–5013.
127 B. Soundiraraju and B. K. George, *ACS Nano*, 2017, **11**, 8892–8900.
128 J. Zhou, X. Zha, X. Zhou, F. Chen, G. Gao, S. Wang, C. Shen, T. Chen, C. Zhi, P. Eklund, S. Du, J. Xue, W. Shi, Z. Chai and Q. Huang, *ACS Nano*, 2017, **11**, 3841–3850.
129 H. Lin, Y. Wang, S. Gao, Y. Chen and J. Shi, *Adv. Mater.*, 2018, **30**, 1703284.
130 M. Wu, B. Wang, Q. Hu, L. Wang and A. Zhou, *Materials*, 2018, **11**, 2112.
131 R. Meshkian, M. Dahlqvist, J. Lu, B. Wickman, J. Halim, J. Thörnberg, Q. Tao, S. Li, S. Intikhab, J. Snyder, M. W. Barsoum, M. Yildizhan, J. Palisaitis, L. Hultman, P. O. Å. Persson and J. Rosen, *Adv. Mater.*, 2018, **30**, 1706409.
132 X. Chen, Y. Zhu, M. Zhang, J. Sui, W. Peng, Y. Li, G. Zhang, F. Zhang and X. Fan, *ACS Nano*, 2019, **13**, 9449–9456.
133 Q. Chen, D. Zhang, J. Pan and W. Fan, *Optik*, 2020, **219**, 165046.
134 B. Soundiraraju, R. Raghavan and B. K. George, *ACS Appl. Nano Mater.*, 2020, **3**, 11007–11016.
135 K. Maeda, H. Wakayama, Y. Washio, A. Ishikawa, M. Okazaki, H. Nakata and S. Matsuishi, *J. Phys. Chem. C*, 2020, **124**, 14640–14645.
136 S. Liu, R. Lv, J. Wang, Y. Wang, H. Wang, H. Zhang and Y. Wang, *J. Mater. Chem. C*, 2021, **9**, 16985–16990.
137 H. Shin, W. Eom, K. H. Lee, W. Jeong, D. J. Kang and T. H. Han, *ACS Nano*, 2021, **15**, 3320–3329.
138 M. Y. Hazman, M. E. El-Sayed, F. F. Kabil, N. A. Helmy, L. Almas, M. McFarland, A. Shams El Din and S. Burian, *Agronomy*, 2022, **12**, 1596.
139 P. Zhang, J. Li, D. Yang, R. A. Soomro and B. Xu, *Adv. Funct. Mater.*, 2023, **33**, 2209918.
140 M. Shi, R. Wang, L. Li, N. Chen, P. Xiao, C. Yan and X. Yan, *Adv. Funct. Mater.*, 2023, **33**, 2209777.
141 X. Sun, X. He, Y. Zhu, E. Obeng, B. Zeng, H. Deng, J. Shen and R. Hu, *Chem. Eng. J.*, 2023, **451**, 138985.
142 M. Wang, X. Liu, B. Qin, Z. Li, Y. Zhang, W. Yang and H. Fan, *Chem. Eng. J.*, 2023, **451**, 138508.
143 S. Li, X. Tang, X. Zhao, S. Lu, J. Luo, Z. Chai, T. Ma, Q. Lan, P. Ma and W. Dong, *J. Mater. Sci. Technol.*, 2023, **133**, 238–248.
144 Z. Abid, K. Rafiq, A. Rauf, R. Hamed Althomali and E. Hussain, *Mater. Adv.*, 2024, DOI: **10.1039/D3MA00710C**.
145 H. Ahmadi, N. Shokrollah, S. Aghaei, S. Gharishvandi, M. M. Goodarzi, A. Mohebifar and N. Tightiz, *J. Mater. Sci.: Mater. Electron.*, 2016, **27**, 4689–4693.

146 Z. Bao, C. Lu, X. Cao, P. Zhang, L. Yang, H. Zhang, D. Sha, W. He, W. Zhang and L. Pan, *Chin. Chem. Lett.*, 2021, **32**, 2648–2658.
147 F. H. Fagerli, Z. Wang, T. Grande, H. Kaland, S. M. Selbach, N. P. Wagner and K. Wiik, *ACS Omega*, 2022, **7**, 23790–23799.
148 L. Li, R. Li, S. Gai, P. Gao, F. He, M. Zhang, Y. Chen and P. Yang, *J. Mater. Chem. A*, 2015, **3**, 15642–15649.
149 C. Lu, L. Yang, B. Yan, L. Sun, P. Zhang, W. Zhang and Z. Sun, *Adv. Funct. Mater.*, 2020, **30**, 2000852.
150 H. Peçenek, S. Yetiman, F. K. Dokan, M. S. Onses, E. Yılmaz and E. Sahmetlioglu, *Ceram. Int.*, 2022, **48**, 7253–7260.
151 M. Shen, W. Jiang, K. Liang, S. Zhao, R. Tang, L. Zhang and J.-Q. Wang, *Angew. Chem., Int. Ed.*, 2021, **60**, 27013–27018.
152 T. Schultz, N. C. Frey, K. Hantanasirisakul, S. Park, S. J. May, V. B. Shenoy, Y. Gogotsi and N. Koch, *Chem. Mater.*, 2019, **31**, 6590–6597.
153 A. Khosla, Sonu, H. T. A. Awan, K. Singh, Gaurav, R. Walvekar, Z. Zhao, A. Kaushik, M. Khalid and V. Chaudhary, *Adv. Sci.*, 2022, **9**, 2203527.
154 Z. Xie, Y. Duo, Z. Lin, T. Fan, C. Xing, L. Yu, R. Wang, M. Qiu, Y. Zhang and Y. Zhao, *Adv. Sci.*, 2020, **7**, 1902236.
155 X. Wang, Y. Wang, Y. Jiang, X. Li, Y. Liu, H. Xiao, Y. Ma, Y. y. Huang and G. Yuan, *Adv. Funct. Mater.*, 2021, **31**, 2103210.
156 M. Li, X. Li, G. Qin, K. Luo, J. Lu, Y. Li, G. Liang, Z. Huang, J. Zhou and L. Hultman, *ACS Nano*, 2021, **15**, 1077–1085.
157 H. Zhu, B. Li, C. Y. Chan, B. L. Q. Ling, J. Tor, X. Y. Oh, W. Jiang, E. Ye, Z. Li and X. J. Loh, *Adv. Drug Delivery Rev.*, 2022, 114644.
158 J. L. Hart, K. Hantanasirisakul, A. C. Lang, Y. Li, F. Mehmood, R. Pachter, A. I. Frenkel, Y. Gogotsi and M. L. Taheri, *Adv. Mater. Interfaces*, 2021, **8**, 2001789.
159 N. Li, X. Chen, W.-J. Ong, D. R. MacFarlane, X. Zhao, A. K. Cheetham and C. Sun, *ACS Nano*, 2017, **11**, 10825–10833.
160 A. Al Mayyahi, S. Sarker, B. M. Everhart, X. He and P. B. Amama, *Mater. Today Commun.*, 2022, **32**, 103835.
161 X. Hu, Y. Wang, Z. Ling, H. Song, Y. Cai, Z. Li, D. Zu and C. Li, *Appl. Surf. Sci.*, 2021, **556**, 149817.
162 T. Hu, Z. Li, M. Hu, J. Wang, Q. Hu, Q. Li and X. Wang, *J. Phys. Chem. C*, 2017, **121**, 19254–19261.
163 M. M. Baig, I. H. Gul, S. M. Baig and F. Shahzad, *J. Electroanal. Chem.*, 2022, **904**, 115920.
164 X. Xu, Y. Zhang, H. Sun, J. Zhou, F. Yang, H. Li, H. Chen, Y. Chen, Z. Liu and Z. Qiu, *Adv. Electron. Mater.*, 2021, **7**, 2000967.
165 K. Nasrin, V. Sudharshan, K. Subramani and M. Sathish, *Adv. Funct. Mater.*, 2022, **32**, 2110267.
166 Y. Xie, M. Naguib, V. N. Mochalin, M. W. Barsoum, Y. Gogotsi, X. Yu, K.-W. Nam, X.-Q. Yang, A. I. Kolesnikov and P. R. Kent, *J. Am. Chem. Soc.*, 2014, **136**, 6385–6394.
167 L. Cheng, X. Li, H. Zhang and Q. Xiang, *J. Phys. Chem. Lett.*, 2019, **10**, 3488–3494.
168 H. Wang, Y. Wu, T. Xiao, X. Yuan, G. Zeng, W. Tu, S. Wu, H. Y. Lee, Y. Z. Tan and J. W. Chew, *Appl. Catal., B*, 2018, **233**, 213–225.
169 Y. Liu, Y.-H. Li, X. Li, Q. Zhang, H. Yu, X. Peng and F. Peng, *ACS Nano*, 2020, **14**, 14181–14189.
170 S. Vigneshwaran, C. M. Park and S. Meenakshi, *Sep. Purif. Technol.*, 2021, **258**, 118003.
171 Y. Li and S. Guo, *Matter*, 2021, **4**, 1142–1188.
172 V. Mehta, H. S. Saini, S. Srivastava, M. K. Kashyap and K. Tankeshwar, *J. Phys. Chem. C*, 2019, **123**, 25052–25060.
173 Q. Meng, J. Ma, Y. Zhang, Z. Li, C. Zhi, A. Hu and J. Fan, *Nanoscale*, 2018, **10**, 3385–3392.
174 V. Natu and M. W. Barsoum, *J. Phys. Chem. C*, 2023, **127**, 20197–20206.
175 H. Ding, Y. Li, M. Li, K. Chen, K. Liang, G. Chen, J. Lu, J. Palisaitis, P. O. Å. Persson, P. Eklund, L. Hultman, S. Du, Z. Chai, Y. Gogotsi and Q. Huang, *Science*, 2023, **379**, 1130–1135.
176 M. A. Hope, A. C. Forse, K. J. Griffith, M. R. Lukatskaya, M. Ghidiu, Y. Gogotsi and C. P. Grey, *Phys. Chem. Chem. Phys.*, 2016, **18**, 5099–5102.
177 D. Li, X. Chen, P. Xiang, H. Du and B. Xiao, *Appl. Surf. Sci.*, 2020, **501**, 144221.
178 Y. Xin and Y.-X. Yu, *Mater. Des.*, 2017, **130**, 512–520.
179 J. Björk and J. Rosen, *Chem. Mater.*, 2021, **33**, 9108–9118.
180 R. Wang, M. Li, K. Sun, Y. Zhang, J. Li and W. Bao, *Small*, 2022, **18**, 2201740.
181 M. Khazaei, M. Arai, T. Sasaki, C.-Y. Chung, N. S. Venkataramanan, M. Estili, Y. Sakka and Y. Kawazoe, *Adv. Funct. Mater.*, 2013, **23**, 2185–2192.
182 Y.-W. Cheng, J.-H. Dai, Y.-M. Zhang and Y. Song, *J. Mater. Chem. A*, 2018, **6**, 20956–20965.
183 E. Balcı, Ü. Ö. Akkuş and S. Berber, *J. Mater. Chem. C*, 2017, **5**, 5956–5961.
184 F. Yang, D. Hegh, D. Song, J. Zhang, K. A. S. Usman, C. Liu, Z. Wang, W. Ma, W. Yang and S. Qin, *Mater. Rep.: Energy*, 2022, **2**, 100079.
185 F. Cao, Y. Zhang, H. Wang, K. Khan, A. K. Tareen, W. Qian, H. Zhang and H. Ågren, *Adv. Mater.*, 2022, **34**, 2107554.
186 Y. Gogotsi, *Chem. Mater.*, 2023, **35**, 8767–8770.
187 Z. Xiao, Z. Li, X. Meng and R. Wang, *J. Mater. Chem. A*, 2019, **7**, 22730–22743.
188 X. Liang, A. Garsuch and L. F. Nazar, *Angew. Chem.*, 2015, **127**, 3979–3983.
189 Y. Wen, T. E. Rufford, X. Chen, N. Li, M. Lyu, L. Dai and L. Wang, *Nano Energy*, 2017, **38**, 368–376.
190 W. Xu, S. Li, W. Zhang, B. Ouyang, W. Yu and Y. Zhou, *ACS Appl. Mater. Interfaces*, 2021, **13**, 49242–49253.
191 F. Yang, D. Hegh, D. Song, J. Zhang, K. A. S. Usman, Z. Wang, P. Zhang, W. Ma, W. Yang and S. Qin, *J. Mater. Chem. A*, 2021, **9**, 6393–6401.
192 B. Yang, Y. She, C. Zhang, S. Kang, J. Zhou and W. Hu, *Nanomaterials*, 2020, **10**, 345.
193 M. Naguib, M. Kurtoglu, V. Presser, J. Lu, J. Niu, M. Heon, L. Hultman, Y. Gogotsi and M. W. Barsoum, *Adv. Mater.*, 2011, **23**, 4207.
194 X. Zhang, Z. Zhang and Z. Zhou, *J. Energy Chem.*, 2018, **27**, 73–85.
195 Z. Zeng, Y. Yan, J. Chen, P. Zan, Q. Tian and P. Chen, *Adv. Funct. Mater.*, 2019, **29**, 1806500.

196 M. Han, X. Yin, H. Wu, Z. Hou, C. Song, X. Li, L. Zhang and L. Cheng, *ACS Appl. Mater. Interfaces*, 2016, **8**, 21011–21019.
197 L. Cheng, Q. Chen, J. Li and H. Liu, *Appl. Catal., B*, 2020, **267**, 118379.
198 C. Peng, H. Wang, H. Yu and F. Peng, *Mater. Res. Bull.*, 2017, **89**, 16–25.
199 M. Khazaei, M. Arai, T. Sasaki, A. Ranjbar, Y. Liang and S. Yunoki, *Phys. Rev. B: Condens. Matter Mater. Phys.*, 2015, **92**, 075411.
200 M. Lu, H. Li, W. Han, J. Chen, W. Shi, J. Wang, X.-M. Meng, J. Qi, H. Li and B. Zhang, *J. Energy Chem.*, 2019, **31**, 148–153.
201 L. Zhang, J. Yang, T. Xie, S. Feng and L. Xu, *Mater. Des.*, 2020, **192**, 108772.
202 Q. Tang, Z. Sun, S. Deng, H. Wang and Z. Wu, *J. Colloid Interface Sci.*, 2020, **564**, 406–417.
203 G. Zhao, J. Zou, X. Chen, J. Yu and F. Jiao, *Chem. Eng. J.*, 2020, **397**, 125407.
204 A. Akhoondi, M. Mirzaei, M. Y. Nassar, Z. Sabaghian, F. Hatami and M. Yusuf, *Synth. Sintering*, 2022, **2**, 151–169.
205 Y. Li, L. Ding, Y. Guo, Z. Liang, H. Cui and J. Tian, *ACS Appl. Mater. Interfaces*, 2019, **11**, 41440–41447.
206 Y. Qin, Y. Sun, Y. Li, C. Li, L. Wang and S. Guo, *Chin. Chem. Lett.*, 2020, **31**, 774–778.
207 T. Cai, L. Wang, Y. Liu, S. Zhang, W. Dong, H. Chen, X. Yi, J. Yuan, X. Xia and C. Liu, *Appl. Catal., B*, 2018, **239**, 545–554.
208 Y. Zhang, L. Wang, N. Zhang and Z. Zhou, *RSC Adv.*, 2018, **8**, 19895–19905.
209 L. Tie, S. Yang, C. Yu, H. Chen, Y. Liu, S. Dong, J. Sun and J. Sun, *J. Colloid Interface Sci.*, 2019, **545**, 63–70.
210 H. Guan, H. He, T. Zeng and C. Zhang, *J. Energy Chem.*, 2021, **63**, 633–641.
211 M. Tang, H. Sun, L. Su, Y. Gao, F. Chen, Z. Wang and C. Wang, *Batteries Supercaps*, 2023, **6**, e202200402.
212 M. Boota, T. Hussain, L. Yang, M. Becuwe, W. Porzio, L. Barba and R. Ahuja, *Adv. Electron. Mater.*, 2021, **7**, 2001202.
213 X. Hui, P. Zhang, J. Li, D. Zhao, Z. Li, Z. Zhang, C. Wang, R. Wang and L. Yin, *Adv. Energy Mater.*, 2022, **12**, 2201393.
214 J. Li, H. Wang and X. Xiao, *Energy Environ. Mater.*, 2020, **3**, 306–322.
215 M. Tahir, A. Ali Khan, S. Tasleem, R. Mansoor and W. K. Fan, *Energy Fuels*, 2021, **35**, 10374–10404.
216 C. Yang, Q. Tan, Q. Li, J. Zhou, J. Fan, B. Li, J. Sun and K. Lv, *Appl. Catal., B*, 2020, **268**, 118738.
217 S. Kajiyama, L. Szabova, H. Iinuma, A. Sugahara, K. Gotoh, K. Sodeyama, Y. Tateyama, M. Okubo and A. Yamada, *Adv. Energy Mater.*, 2017, **7**, 1601873.
218 X. Xie, Y. Xue, L. Li, S. Chen, Y. Nie, W. Ding and Z. Wei, *Nanoscale*, 2014, **6**, 11035–11040.
219 L. Liu, M. Orbay, S. Luo, S. Duluard, H. Shao, J. Harmel, P. Rozier, P.-L. Taberna and P. Simon, *ACS Nano*, 2021, **16**, 111–118.
220 K. Arole, J. W. Blivin, S. Saha, D. E. Holta, X. Zhao, A. Sarmah, H. Cao, M. Radovic, J. L. Lutkenhaus and M. J. Green, *iScience*, 2021, **24**, 103403.
221 Y. Chen, T. Shi, P. Liu, X. Ma, L. Shui, C. Shang, Z. Chen, X. Wang, K. Kempa and G. Zhou, *J. Mater. Chem. A*, 2018, **6**, 19167–19175.
222 J. Xiao, J. Wen, J. Zhao, X. Ma, H. Gao and X. Zhang, *Electrochim. Acta*, 2020, **337**, 135803.
223 N. J. Prakash and B. Kandasubramanian, *J. Alloys Compd.*, 2021, **862**, 158547.
224 S. M. George and B. Kandasubramanian, *Ceram. Int.*, 2020, **46**, 8522–8535.
225 F. Damiri, M. H. Rahman, M. Zehravi, A. A. Awaji, M. Z. Nasrullah, H. A. Gad, M. Z. Bani-Fwaz, R. S. Varma, M. O. Germoush and H. S. Al-Malky, *Materials*, 2022, **15**, 1666.
226 B. Lu, Z. Zhu, B. Ma, W. Wang, R. Zhu and J. Zhang, *Small*, 2021, **17**, 2100946.
227 X. Lin, Z. Li, J. Qiu, Q. Wang, J. Wang, H. Zhang and T. Chen, *Biomater. Sci.*, 2021, **9**, 5437–5471.
228 M. Soleymaniha, M. A. Shahbazi, A. R. Rafieerad, A. Maleki and A. Amiri, *Adv. Healthcare Mater.*, 2019, **8**, 1801137.
229 C. Huang, X. Peng, D.-J. Pang, J. Li, B. S. Paulsen, F. Rise, Y.-L. Chen, Z.-L. Chen, R.-Y. Jia, L.-X. Li, X. Song, B. Feng, Z.-Q. Yin and Y.-F. Zou, *Food Funct.*, 2021, **12**, 10828–10841.
230 N. Garg and F. J. Ahmad, in *MXene-Filled Polymer Nanocomposites*, CRC Press, 2023, pp. 247–258.
231 X. Han, J. Huang, H. Lin, Z. Wang, P. Li and Y. Chen, *Adv. Healthcare Mater.*, 2018, **7**, 1701394.
232 H. Lin, X. Wang, L. Yu, Y. Chen and J. Shi, *Nano Lett.*, 2017, **17**, 384–391.
233 Y. Zi, K. Yang, J. He, Z. Wu, J. Liu and W. Zhang, *Adv. Drug Delivery Rev.*, 2022, 114449.
234 G. Liu, J. Zou, Q. Tang, X. Yang, Y. Zhang, Q. Zhang, W. Huang, P. Chen, J. Shao and X. Dong, *ACS Appl. Mater. Interfaces*, 2017, **9**, 40077–40086.
235 Z. Yu, L. Jiang, R. Liu, W. Zhao, Z. Yang, J. Zhang and S. Jin, *Chem. Eng. J.*, 2021, **426**, 131914.
236 Y. Xu, Y. Wang, J. An, A. C. Sedgwick, M. Li, J. Xie, W. Hu, J. Kang, S. Sen, A. Steinbrueck, B. Zhang, L. Qiao, S. Wageh, J. F. Arambula, L. Liu, H. Zhang, J. L. Sessler and J. S. Kim, *Bioact. Mater.*, 2022, **14**, 76–85.
237 L. Ou, B. Song, H. Liang, J. Liu, X. Feng, B. Deng, T. Sun and L. Shao, *Part. Fibre Toxicol.*, 2016, **13**, 1–24.
238 Y. Guan, J. Yan, Y. Shan, Y. Zhou, Y. Hang, R. Li, Y. Liu, B. Liu, Q. Nie and B. Bruckner, *Nat. Energy*, 2023, **8**, 304–316.
239 M. Amin, H. H. Shah, A. G. Fareed, W. U. Khan, E. Chung, A. Zia, Z. U. R. Farooqi and C. Lee, *Int. J. Hydrogen Energy*, 2022, **47**, 33112–33134.
240 M. Thirunavukkarasu, Y. Sawle and H. Lala, *Renewable Sustainable Energy Rev.*, 2023, **176**, 113192.
241 T. Najam, M. K. Aslam, K. Rafiq, M. Altaf Nazir, A. u. Rehman, M. Imran, M. S. Javed, X. Cai and S. S. A. Shah, *Mater. Sci. Eng. B*, 2021, **273**, 115417.
242 Q. Jiang, N. Kurra, K. Maleski, Y. Lei, H. Liang, Y. Zhang, Y. Gogotsi and H. N. Alshareef, *Adv. Energy Mater.*, 2019, **9**, 1901061.
243 S. Xu, G. Wei, J. Li, W. Han and Y. Gogotsi, *J. Mater. Chem. A*, 2017, **5**, 17442–17451.

244 R. Rajeev, D. A. Thadathil and A. Varghese, *Crit. Rev. Solid State Mater. Sci.*, 2022, 1–43.
245 X. Wang, T. S. Mathis, K. Li, Z. Lin, L. Vlcek, T. Torita, N. C. Osti, C. Hatter, P. Urbankowski and A. Sarycheva, *Nat. Energy*, 2019, **4**, 241–248.
246 S. Buczek, M. L. Barsoum, S. Uzun, N. Kurra, R. Andris, E. Pomerantseva, K. A. Mahmoud and Y. Gogotsi, *Energy Environ. Mater.*, 2020, **3**, 398–404.
247 N. Kurra, M. Alhabeb, K. Maleski, C.-H. Wang, H. N. Alshareef and Y. Gogotsi, *ACS Energy Lett.*, 2018, **3**, 2094–2100.
248 C.-F. Liu, Y.-C. Liu, T.-Y. Yi and C.-C. Hu, *Carbon*, 2019, **145**, 529–548.
249 A. S. Levitt, M. Alhabeb, C. B. Hatter, A. Sarycheva, G. Dion and Y. Gogotsi, *J. Mater. Chem. A*, 2019, **7**, 269–277.
250 R. Imsong and D. D. Purkayastha, *Sep. Purif. Technol.*, 2023, **306**, 122636.
251 L. Wang, X. Feng, L. Ren, Q. Piao, J. Zhong, Y. Wang, H. Li, Y. Chen and B. Wang, *J. Am. Chem. Soc.*, 2015, **137**, 4920–4923.
252 Q. X. Xia, N. M. Shinde, J. M. Yun, T. Zhang, R. S. Mane, S. Mathur and K. H. Kim, *Electrochim. Acta*, 2018, **271**, 351–360.
253 M. Mahmood, A. Rasheed, I. Ayman, T. Rasheed, S. Munir, S. Ajmal, P. O. Agboola, M. F. Warsi and M. Shahid, *Energy Fuels*, 2021, **35**, 3469–3478.
254 A. Sikdar, P. Dutta, S. K. Deb, A. Majumdar, N. Padma, S. Ghosh and U. N. Maiti, *Electrochim. Acta*, 2021, **391**, 138959.
255 Y. Li, Z. Wang, J. Hu, S. Li, Y. Du, X. Han and P. Xu, *Adv. Funct. Mater.*, 2020, **30**, 1910498.
256 A. Sharma, P. Mane, B. Chakraborty and C. S. Rout, *ACS Appl. Energy Mater.*, 2021, **4**, 14198–14209.
257 W. Hou, Y. Sun, Y. Zhang, T. Wang, L. Wu, Y. Du and W. Zhong, *J. Alloys Compd.*, 2021, **859**, 157797.
258 A. M. Omer, G. S. Elgarhy, G. M. El-Subruiti, R. E. Khalifa and A. S. Eltaweil, *Int. J. Biol. Macromol.*, 2020, **148**, 1072–1083.
259 H. Liu, R. Hu, J. Qi, Y. Sui, Y. He, Q. Meng, F. Wei, Y. Ren, Y. Zhao and W. Wei, *Adv. Mater. Interfaces*, 2020, **7**, 1901659.
260 A. Szuplewska, D. Kulpińska, A. Dybko, M. Chudy, A. M. Jastrzębska, A. Olszyna and Z. Brzózka, *Trends Biotechnol.*, 2020, **38**, 264–279.
261 K. Rafiq, H. D. Mai, J. K. Kim, J. M. Woo, B. M. Moon, C. H. Park and H. Yoo, *Sens. Actuators, B*, 2017, **251**, 472–480.
262 R. A. Soomro, S. Jawaid, Q. Zhu, Z. Abbas and B. Xu, *Chin. Chem. Lett.*, 2020, **31**, 922–930.
263 J. Liu, X. Jiang, R. Zhang, Y. Zhang, L. Wu, W. Lu, J. Li, Y. Li and H. Zhang, *Adv. Funct. Mater.*, 2019, **29**, 1807326.
264 T. Shay, M. D. Dickey and O. D. Velev, *Lab Chip*, 2017, **17**, 710–716.
265 X. Li, X. Li, T. Liu, Y. Lu, C. Shang, X. Ding, J. Zhang, Y. Feng and F.-J. Xu, *ACS Appl. Mater. Interfaces*, 2021, **13**, 46848–46857.
266 Y. Yue, N. Liu, W. Liu, M. Li, Y. Ma, C. Luo, S. Wang, J. Rao, X. Hu, J. Su, Z. Zhang, Q. Huang and Y. Gao, *Nano Energy*, 2018, **50**, 79–87.
267 F. Wang, C. Yang, M. Duan, Y. Tang and J. Zhu, *Biosens. Bioelectron.*, 2015, **74**, 1022–1028.
268 P. Kalluru and R. Vankayala, *2D Functional Nanomaterials: Synthesis, Characterization and Applications*, 2021, pp. 31–46.
269 E. Lee, A. VahidMohammadi, B. C. Prorok, Y. S. Yoon, M. Beidaghi and D.-J. Kim, *ACS Appl. Mater. Interfaces*, 2017, **9**, 37184–37190.
270 S. Ullah, F. Shahzad, B. Qiu, X. Fang, A. Ammar, Z. Luo and S. A. Zaidi, *Prog. Mater. Sci.*, 2022, **129**, 100967.
271 A. Rhouati, M. Berkani, Y. Vasseghian and N. Golzadeh, *Chemosphere*, 2022, **291**, 132921.
272 B. Xu, C. Zhi and P. Shi, *J. Phys.: Mater.*, 2020, **3**, 031001.
273 R. Rakhi, P. Nayak, C. Xia and H. N. Alshareef, *Sci. Rep.*, 2016, **6**, 1–10.
274 H. Liu, C. Duan, C. Yang, W. Shen, F. Wang and Z. Zhu, *Sens. Actuators, B*, 2015, **218**, 60–66.
275 L. Lorencova, T. Bertok, J. Filip, M. Jerigova, D. Velic, P. Kasak, K. A. Mahmoud and J. Tkac, *Sens. Actuators, B*, 2018, **263**, 360–368.
276 P. A. Rasheed, R. P. Pandey, K. Rasool and K. A. Mahmoud, *Sens. Actuators, B*, 2018, **265**, 652–659.
277 B. Xu, M. Zhu, W. Zhang, X. Zhen, Z. Pei, Q. Xue, C. Zhi and P. Shi, *Adv. Mater.*, 2016, **28**, 3333–3339.
278 X. Liu, L. He, P. Li, X. Li and P. Zhang, *ChemElectroChem*, 2021, **8**, 3658–3665.
279 R. Gao, X. Yang, Q. Yang, Y. Wu, F. Wang, Q. Xia and S.-J. Bao, *Microchim. Acta*, 2021, **188**, 1–9.
280 T. Xia, G. Liu, J. Wang, S. Hou and S. Hou, *Biosens. Bioelectron.*, 2021, **183**, 113243.
281 S. Sun, M. Wang, X. Chang, Y. Jiang, D. Zhang, D. Wang, Y. Zhang and Y. Lei, *Sens. Actuators, B*, 2020, **304**, 127274.
282 Y. Sun, L. Chen, Y. Wang, Z. Zhao, P. Li, W. Zhang, Y. Leprince-Wang and J. Hu, *J. Mater. Sci.*, 2017, **52**, 1561–1572.
283 K. Matthews, T. Zhang, C. E. Shuck, A. VahidMohammadi and Y. Gogotsi, *Chem. Mater.*, 2021, **34**, 499–509.
284 M. Wu, Y. An, R. Yang, Z. Tao, Q. Xia, Q. Hu, M. Li, K. Chen, Z. Zhang and Q. Huang, *ACS Appl. Nano Mater.*, 2021, **4**, 6257–6268.
285 T. Thomas, J. A. R. Ramon, V. Agarwal, A. Álvarez-Méndez, J. A. Martinez, Y. Kumar and K. Sanal, *Microporous Mesoporous Mater.*, 2022, **336**, 111872.
286 H. Lu, J. Tournet, K. Dastafkan, Y. Liu, Y. H. Ng, S. K. Karuturi, C. Zhao and Z. Yin, *Chem. Rev.*, 2021, **121**, 10271–10366.
287 F. Ahmad, K. Rafiq, T. Najam, E. Hussain, M. Sohail, M. Z. Abid, A. Mahmood, M. S. Javed and S. S. A. Shah, *Int. J. Hydrogen Energy*, 2023, **48**, 35075–35111.
288 K. U. Sahar, K. Rafiq, Z. Abid, U. ur Rehman, A. Rauf and E. Hussain, *React. Chem. Eng.*, 2023, **8**, 2522–2536.
289 M. Jalil, K. Rafiq, M. Z. Abid, A. Rauf, S. Wang, S. Iqbal and E. Hussain, *Nanoscale Adv.*, 2023, **5**, 3233–3246.

290 M. Sabir, K. Rafiq, M. Z. Abid, U. Quyyum, S. S. A. Shah, M. Faizan, A. Rauf, S. Iqbal and E. Hussain, *Fuel*, 2023, **353**, 129196.
291 C. V. Pham, D. Escalera-López, K. Mayrhofer, S. Cherevko and S. Thiele, *Adv. Energy Mater.*, 2021, **11**, 2101998.
292 H. Wang, Y. Wu, X. Yuan, G. Zeng, J. Zhou, X. Wang and J. W. Chew, *Adv. Mater.*, 2018, **30**, 1704561.
293 L. Yang, C. Dall'Agnese, Y. Dall'Agnese, G. Chen, Y. Gao, Y. Sanehira, A. K. Jena, X.-F. Wang, Y. Gogotsi and T. Miyasaka, *Adv. Funct. Mater.*, 2019, **29**, 1905694.
294 M. Bilal, Z. U. Rehman, M. Zaqa, J. Hou, F. K. Butt and A. Hussain, in *Energy Applications of 2D Nanomaterials*, CRC Press, 2022, pp. 185–201.
295 J. Zhang, Y. Zhao, X. Guo, C. Chen, C.-L. Dong, R.-S. Liu, C.-P. Han, Y. Li, Y. Gogotsi and G. Wang, *Nat. Catal.*, 2018, **1**, 985–992.
296 R. Chen, C. Yang, W. Cai, H.-Y. Wang, J. Miao, L. Zhang, S. Chen and B. Liu, *ACS Energy Lett.*, 2017, **2**, 1070–1075.
297 L. Yang, Z. Chen, X. Wang and M. Jin, *Nanomaterials*, 2022, **12**, 542.
298 L. Ding, S. Zeng, W. Zhang, C. Guo, X. Chen, B. Peng, Z. Lv, H. Zhou and Q. Xu, *ACS Appl. Energy Mater.*, 2022, **5**, 11540–11552.
299 K. R. G. Lim, A. D. Handoko, S. K. Nemani, B. Wyatt, H.-Y. Jiang, J. Tang, B. Anasori and Z. W. Seh, *ACS Nano*, 2020, **14**, 10834–10864.
300 X. Zhang, Z. Geng, J. Jian, Y. He, Z. Lv, X. Liu and H. Yuan, *Catalysts*, 2020, **10**, 293.
301 X. Li, Y. Bai, X. Shi, N. Su, G. Nie, R. Zhang, H. Nie and L. Ye, *Mater. Adv.*, 2021, **2**, 1570–1594.
302 C. Xia, H. Ye, A. Kim, A. Sabahi Namini, S. Li, S. A. Delbari, J. Y. Park, D. Kim, Q. V. Le, R. S. Varma, R. Luque, A. T-Raissi, H. W. Jang and M. Shokouhimehr, *Chemosphere*, 2023, **325**, 138323.
303 S. Chen, T. Takata and K. Domen, *Nat. Rev. Mater.*, 2017, **2**, 1–17.
304 K. Takanabe, *ACS Catal.*, 2017, **7**, 8006–8022.
305 X. Wu, Z. Wang, M. Yu, L. Xiu and J. Qiu, *Adv. Mater.*, 2017, **29**, 1607017.
306 Y. Jiang, T. Sun, X. Xie, W. Jiang, J. Li, B. Tian and C. Su, *ChemSusChem*, 2019, **12**, 1368–1373.
307 J. Ren, H. Zong, Y. Sun, S. Gong, Y. Feng, Z. Wang, L. Hu, K. Yu and Z. Zhu, *CrystEngComm*, 2020, **22**, 1395–1403.
308 Y. Jiang, X. Wu, Y. Yan, S. Luo, X. Li, J. Huang, H. Zhang and D. Yang, *Small*, 2019, **15**, 1805474.
309 Y. Yuan, H. Li, L. Wang, L. Zhang, D. Shi, Y. Hong and J. Sun, *ACS Sustain. Chem. Eng.*, 2019, **7**, 4266–4273.
310 D. A. Kuznetsov, Z. Chen, P. V. Kumar, A. Tsoukalou, A. Kierzkowska, P. M. Abdala, O. V. Safonova, A. Fedorov and C. R. Müller, *J. Am. Chem. Soc.*, 2019, **141**, 17809–17816.
311 P. Kuang, M. He, B. Zhu, J. Yu, K. Fan and M. Jaroniec, *J. Catal.*, 2019, **375**, 8–20.
312 Y. Geng, G. Cao, L. Wang and S. Wang, *PLoS One*, 2019, **14**, e0219512.
313 J. Liu, Y. Liu, D. Xu, Y. Zhu, W. Peng, Y. Li, F. Zhang and X. Fan, *Appl. Catal., B*, 2019, **241**, 89–94.
314 T. Su, Z. D. Hood, M. Naguib, L. Bai, S. Luo, C. M. Rouleau, I. N. Ivanov, H. Ji, Z. Qin and Z. Wu, *Nanoscale*, 2019, **11**, 8138–8149.
315 M. Zhang, J. Qin, S. Rajendran, X. Zhang and R. Liu, *ChemSusChem*, 2018, **11**, 4226–4236.
316 P. Lin, J. Shen, X. Yu, Q. Liu, D. Li and H. Tang, *Ceram. Int.*, 2019, **45**, 24656–24663.
317 M. Tahir and B. Tahir, *Ind. Eng. Chem. Res.*, 2020, **59**, 9841–9857.
318 J. Low, L. Zhang, T. Tong, B. Shen and J. Yu, *J. Catal.*, 2018, **361**, 255–266.
319 Q. Liu, X. Tan, S. Wang, F. Ma, H. Znad, Z. Shen, L. Liu and S. Liu, *Environ. Sci.: Nano*, 2019, **6**, 3158–3169.
320 Y. Yang, D. Zhang and Q. Xiang, *Nanoscale*, 2019, **11**, 18797–18805.
321 Y. Li, X. Chen, Y. Sun, X. Meng, Y. Dall'Agnese, G. Chen, C. Dall'Agnese, H. Ren, S. i. Sasaki and H. Tamiaki, *Adv. Mater. Interfaces*, 2020, **7**, 1902080.
322 S. Vigneshwaran, P. Karthikeyan, C. M. Park and S. Meenakshi, *J. Environ. Manage.*, 2020, **273**, 111125.
323 Y. Li, X. Deng, J. Tian, Z. Liang and H. Cui, *Appl. Mater. Today*, 2018, **13**, 217–227.
324 A. Iqbal, J. Kwon, M.-K. Kim and C. Koo, *Mater. Today Adv.*, 2021, **9**, 100124.
325 Y. Zhang, L. Wang, J. Zhang, P. Song, Z. Xiao, C. Liang, H. Qiu, J. Kong and J. Gu, *Compos. Sci. Technol.*, 2019, **183**, 107833.
326 Z. Zhou, Q. Song, B. Huang, S. Feng and C. Lu, *ACS Nano*, 2021, **15**, 12405–12417.
327 M. Han, C. E. Shuck, R. Rakhmanov, D. Parchment, B. Anasori, C. M. Koo, G. Friedman and Y. Gogotsi, *ACS Nano*, 2020, **14**, 5008–5016.
328 K. Raagulan, R. Braveenth, H. J. Jang, Y. Seon Lee, C.-M. Yang, B. Mi Kim, J. J. Moon and K. Y. Chai, *Materials*, 2018, **11**, 1803.
329 A. Tanvir, P. Sobolčiak, A. Popelka, M. Mrlik, Z. Spitalsky, M. Micusik, J. Prokes and I. Krupa, *Polymers*, 2019, **11**, 1272.
330 M. C. Vu, D. Mani, J.-B. Kim, T.-H. Jeong, S. Park, G. Murali, I. In, J.-C. Won, D. Losic and C.-S. Lim, *Composites, Part A*, 2021, **149**, 106574.
331 B. Zhou, Y. Li, Z. Li, J. Ma, K. Zhou, C. Liu, C. Shen and Y. Feng, *J. Mater. Chem. C*, 2021, **9**, 10425–10434.
332 B. Aïssa, A. Sinopoli, A. Ali, Y. Zakaria, A. Zekri, M. Helal, M. Nedil, F. Rosei, S. Mansour and K. Mahmoud, *Carbon*, 2021, **173**, 528–539.
333 K. Khan, A. K. Tareen, M. Aslam, R. Wang, Y. Zhang, A. Mahmood, Z. Ouyang, H. Zhang and Z. Guo, *J. Mater. Chem. C*, 2020, **8**, 387–440.
334 X. Hu, B. Quan, C. Zhu, H. Wen, M. Sheng, S. Liu, X. Li, H. Wu, X. Lu and J. Qu, *Adv. Sci.*, 2023, **10**, 2206835.
335 M. Liu, W. Jiang, P. Song, J. Ji and Q. Wang, *Inorg. Chem. Commun.*, 2022, **140**, 109455.
336 Q. Feng, F. Deng, K. Li, M. Dou, S. Zou and F. Huang, *Colloids Surf., A*, 2021, **625**, 126903.
337 G. Wen, X. Wen, H. Cao, P. Bai, Y. Meng, L. Ma and Y. Tian, *Appl. Nanosci.*, 2023, **186**, 108590.

338 P. Tian, G. Yu, K. Wei, Z. Zhang and N. Wang, *Ceram. Int.*, 2021, **47**, 30722–30728.
339 Z.-K. Li, Y. Wei, X. Gao, L. Ding, Z. Lu, J. Deng, X. Yang, J. Caro and H. Wang, *Angew. Chem., Int. Ed.*, 2020, **59**, 9751–9756.
340 E. Marquis, M. Cutini, B. Anasori, A. Rosenkranz and M. C. Righi, *ACS Appl. Nano Mater.*, 2022, **5**, 10516–10527.
341 Y. Guo, X. Zhou, D. Wang, X. Xu and Q. Xu, *Langmuir*, 2019, **35**, 14481–14485.
342 Y. Guan, M. Zhang, J. Qin, X. Ma, C. Li and J. Tang, *J. Phys. Chem. C*, 2020, **124**, 13664–13671.
343 Y. Yang, J. Zhu, K. Hou, L. Ma, Z. Li, W. Jia, H. Wang, J. Wang and S. Yang, *Chem. Eng. J.*, 2022, **442**, 136238.
344 W. Lian, X. Jie, Y. Lv and W. Yu, *Appl. Nanosci.*, 2021, **11**, 1471–1479.
345 M. E. Valdés, L. H. Santos, M. C. R. Castro, A. Giorgi, D. Barceló, S. Rodríguez-Mozaz and M. V. Amé, *Environ. Pollut.*, 2021, **269**, 116133.
346 M. Z. Abid, K. Rafiq, A. Rauf, S. S. A. Shah, R. Jin and E. Hussain, *Nanoscale Adv.*, 2023, **5**, 3247–3259.
347 A. Ilyas, K. Rafiq, M. Z. Abid, A. Rauf and E. Hussain, *RSC Adv.*, 2023, **13**, 2379–2391.
348 A. Aslam, M. Z. Abid, K. Rafiq, A. Rauf and E. Hussain, *Sci. Rep.*, 2023, **13**, 6306.
349 X. Yang, Y. Liu, S. Hu, F. Yu, Z. He, G. Zeng, Z. Feng and A. Sengupta, *Polym. Adv. Technol.*, 2021, **32**, 1000–1010.
350 A. Abbas, A. M. Al-Amer, T. Laoui, M. J. Al-Marri, M. S. Nasser, M. Khraisheh and M. A. Atieh, *Sep. Purif. Technol.*, 2016, **157**, 141–161.
351 R. Castro-Muñoz, E. Gontarek and A. Figoli, in *Current Trends and Future Developments on (Bio-) Membranes*, Elsevier, 2020, pp. 125–149.
352 R. Castro-Muñoz, B. E. Barragán-Huerta, V. Fíla, P. C. Denis and R. Ruby-Figueroa, *Waste Biomass Valorization*, 2018, **9**, 513–529.
353 Z. Abid, A. Ilyas, K. Rafiq, M. A. Nadeem, A. Rauf, A. Wasim and E. Hussain, *Environ. Sci.: Water Res. Technol.*, 2023, **9**, 2238–2252.
354 U. Quyyum, K. Rafiq, M. Z. Abid, F. Ahmad, A. Rauf and E. Hussain, *Environ. Sci.: Water Res. Technol.*, 2023, **9**, 1147–1160.
355 P. Karthikeyan, K. Ramkumar, K. Pandi, A. Fayyaz, S. Meenakshi and C. M. Park, *Ceram. Int.*, 2021, **47**, 3692–3698.
356 S. Wang, Y. Liu, Q.-F. Lü and H. Zhuang, *J. Mol. Liq.*, 2020, **297**, 111810.
357 A. Shahzad, J. Jang, S.-R. Lim and D. S. Lee, *Environ. Res.*, 2020, **182**, 109005.
358 B.-M. Jun, M. Jang, C. M. Park, J. Han and Y. Yoon, *Nucl. Eng. Technol.*, 2020, **52**, 1201–1207.
359 L. Wang, H. Song, L. Yuan, Z. Li, Y. Zhang, J. K. Gibson, L. Zheng, Z. Chai and W. Shi, *Environ. Sci. Technol.*, 2018, **52**, 10748–10756.
360 S. Kim, F. Gholamirad, M. Yu, C. M. Park, A. Jang, M. Jang, N. Taheri-Qazvini and Y. Yoon, *Chem. Eng. J.*, 2021, **406**, 126789.
361 L. Wang, W. Tao, L. Yuan, Z. Liu, Q. Huang, Z. Chai, J. K. Gibson and W. Shi, *Chem. Commun.*, 2017, **53**, 12084–12087.
362 B.-M. Jun, C. M. Park, J. Heo and Y. Yoon, *J. Environ. Manage.*, 2020, **256**, 109940.
363 Y. Yan, H. Han, Y. Dai, H. Zhu, W. Liu, X. Tang, W. Gan and H. Li, *ACS Appl. Nano Mater.*, 2021, **4**, 11763–11769.
364 V. T. Quyen, L. T. T. Ha, D. M. Thanh, Q. V. Le, N. M. Viet, N. T. Nham and P. Q. Thang, *Environ. Technol. Innovation*, 2021, **21**, 101286.
365 N. My Tran, Q. Thanh Hoai Ta and J.-S. Noh, *Appl. Surf. Sci.*, 2021, **538**, 148023.
366 L. Ding, Y. Wei, Y. Wang, H. Chen, J. Caro and H. Wang, *Angew. Chem., Int. Ed.*, 2017, **56**, 1825–1829.
367 Y. Fan, J. Li, S. Wang, X. Meng, W. Zhang, Y. Jin, N. Yang, X. Tan, J. Li and S. Liu, *Chem. Eng. J.*, 2020, **401**, 126073.
368 J. Zhao, Y. Yang, C. Yang, Y. Tian, Y. Han, J. Liu, X. Yin and W. Que, *J. Mater. Chem. A*, 2018, **6**, 16196–16204.
369 X. Chen, X. Tong, J. Gao, L. Yang, J. Ren, W. Yang, S. Liu, M. Qi, J. Crittenden and R. Hao, *Environ. Sci. Technol.*, 2022, **56**, 4542–4552.
370 L. Zhang, Y. Huang, H. Dong, R. Xu and S. Jiang, *Composites, Part B*, 2021, **223**, 109149.
371 C. Lan, H. Jia, M. Qiu and S. Fu, *ACS Appl. Mater. Interfaces*, 2021, **13**, 38761–38772.
372 L. Liu, Z. Ma, M. Zhu, L. Liu, J. Dai, Y. Shi, J. Gao, T. Dinh, T. Nguyen and L.-C. Tang, *J. Mater. Sci. Technol.*, 2023, **132**, 59–68.
373 Y. Shi, Z. Wang, C. Liu, H. Wang, J. Guo, L. Fu, Y. Feng, L. Wang, F. Yang and M. Liu, *Composites, Part B*, 2022, **236**, 109792.
374 M. Mao, K.-X. Yu, C.-F. Cao, L.-X. Gong, G.-D. Zhang, L. Zhao, P. Song, J.-F. Gao and L.-C. Tang, *Chem. Eng. J.*, 2022, **427**, 131615.
375 Z.-H. Zhang, J.-W. Zhang, C.-F. Cao, K.-Y. Guo, L. Zhao, G.-D. Zhang, J.-F. Gao and L.-C. Tang, *Chem. Eng. J.*, 2020, **386**, 123894.
376 E. Jiao, K. Wu, Y. Liu, M. Lu, Z. Hu, B. Chen, J. Shi and M. Lu, *Composites, Part A*, 2021, **146**, 106417.
377 Y. Zhu, X. Zhao, Q. Peng, H. Zheng, F. Xue, P. Li, Z. Xu and X. He, *Nanoscale Adv.*, 2021, **3**, 5683–5693.
378 Y. Liu, K. Wu, M. Lu, E. Jiao, H. Zhang, J. Shi and M. Lu, *Composites, Part A*, 2021, **141**, 106227.
379 N.-N. Wang, H. Wang, Y.-Y. Wang, Y.-H. Wei, J.-Y. Si, A. C. Y. Yuen, J.-S. Xie, B. Yu, S.-E. Zhu and H.-D. Lu, *ACS Appl. Mater. Interfaces*, 2019, **11**, 40512–40523.
380 Y. Jiang, X. Ru, W. Che, Z. Jiang, H. Chen, J. Hou and Y. Yu, *Composites, Part B*, 2022, **229**, 109460.
381 Y. I. Jhon, J. Koo, B. Anasori, M. Seo, J. H. Lee, Y. Gogotsi and Y. M. Jhon, *Adv. Mater.*, 2017, **29**, 1702496.
382 K. Chaudhuri, *Plasmonic Metasurfaces Utilizing Emerging Material Platforms*, Purdue University Graduate School, 2019.
383 C. Ma, W. Huang, Y. Wang, J. Adams, Z. Wang, J. Liu, Y. Song, Y. Ge, Z. Guo and L. Hu, *Nanophotonics*, 2020, **9**, 2451–2458.

384 L. Zhang, Q. Sheng, L. Chen, J. Zhang, S. Fu, Q. Fang, Y. Wang, W. Shi and J. Yao, *Opt. Lett.*, 2022, **47**, 3964–3967.
385 K. Y. Lau, X. Liu and J. Qiu, *Laser Photonics Rev.*, 2022, **16**, 2100709.
386 Q. Wu, X. Jin, S. Chen, X. Jiang, Y. Hu, Q. Jiang, L. Wu, J. Li, Z. Zheng and M. Zhang, *Opt. Express*, 2019, **27**, 10159–10170.
387 F. Yang, Y. Ge, T. Yin, J. Guo, F. Zhang, X. Tang, M. Qiu, W. Liang, N. Xu and C. Wang, *ACS Appl. Nano Mater.*, 2020, **3**, 11850–11860.
388 Y. I. Jhon, J. Lee, Y. M. Jhon and J. H. Lee, *Nanophotonics*, 2021, **10**, 1741–1751.
389 G. Sun, M. Feng, K. Zhang, T. Wang, Y. Li, D. Han, Y. Li and F. Song, *Results Phys.*, 2021, **26**, 104451.